Oscillation and Extinction in Flames

Heyang Wang

A DISSERTATION

PRESENTED TO THE FACULTY

OF PRINCETON UNIVERSITY

IN CANDIDACY FOR THE DEGREE

OF DOCTOR OF PHILOSOPHY

RECOMMENDED FOR ACCEPTANCE

BY THE DEPARTMENT OF

MECHANICAL AND AEROSPACE ENGINEERING

November 2007

Abstract

Oscillation phenomena in flames were theoretically investigated for both diffusion and premixed flames. For diffusion flames, oscillations develop intrinsically as a result of thermal-diffusive instability when the Lewis numbers are larger than unity. A nonlinear stability analysis for the intrinsic oscillation in a planar flame was first conducted by deriving an evolution equation for the amplitude of perturbation, through which three possible flame responses were predicted: the flame may be stable, unstable or oscillate persistently. This study was then extended to investigate forced flame oscillations by incorporating imposed flow oscillations. Resonance between the intrinsic and forced oscillations was identified when the flame is close to the marginally stable state and the imposed frequency approaches the intrinsic flame oscillation frequency.

The analysis was then extended to radiation-affected diffusion flames. A model accounting for effects of radiative heat loss and nonunity Lewis numbers was first developed to study the structure and extinction characteristics of counterflow diffusion flames. Dual extinction limits in the presence of radiative loss, namely the kinetic and radiative limits at small and large Damköhler numbers, respectively, were identified. Based on this result, the model was then employed to study intrinsic flame oscillations with emphasis on those developed near the radiative extinction limit. It was shown that radiative loss assumes a similar role as increasing the thermal diffusivity of the reactants. Thus, flame oscillation near the radiative limit is still a thermal-diffusive instability phenomenon in nature, although it may develop under unity Lewis number.

For premixed flames, the study was focused on the linear response of stretch-affected premixed flames to flow oscillations. In particular, the effects of flame stretch on the response of heat release rate in a wedge-shaped flame were studied. It was found that the effects of flame stretch become important through the modulation of the flame surface area when the normalized oscillation frequency is of the order of $O(\hat{\sigma}_C^{-1/2})$, where $\hat{\sigma}_C$ is the Markstein number characterizing the curvature effect of flame surface. For frequency below this order, the flame responds as an unstretched flame.

Acknowledgements

My academic journey at Princeton would have never been possible without the generosity and kind support from many individuals, to whom I own a tremendous debt of gratitude.

The first person I wish to express my gratitude is my advisor, Professor Chung K. Law. His high standard of scholarship and generous dispensing of encouragement are constant inspiration and strength that have nourished my intellectual growth and sharpened my personality. I count it as my great fortune that, in having Professor Law as my academic advisor, I have also acquired a personal counselor whose wisdom has been essential in my growth as a scholar.

I would like to express my gratitude to Professor John K. Bechtold of New Jersey Institute of Technology. He led me into the beautiful world of theoretical combustion. His proficient guidance and trenchant yet gentle comments have sharpened my skills and mind.

I would also like to thank Professor M. Matalon and Professor Y. Ju for spending their time reviewing this dissertation and offering many helpful comments which have greatly improved this dissertation.

My life as a graduate student was immensely enriched through the daily interactions with the senior researchers and the fellow graduate students of our research group: Delin Zhu, Hongyan Sun, Matei Radulescu, Erik Christiansen, John Blouch, Tianfeng Lu, Kuo-Long (Peter) Pan, Sean Yoo, Jiao Yuan, Xiaolin Zheng, Grunde Jomaas, Tsung-Ping (Albert) Hsieh, Peng (Paul) Zhang, Ben Stiegemeier, Andrew Kelley and Wei

Liu. All of them have made the time in the lab so enjoyable. I want to specially thank Delin Zhu and his wife Ying (Lucy) Lu for all their perpetual hospitality, support and friendship in these years. Dr. Tianfeng Lu has been a superb colleague and genuine friend. I benefited greatly from his expertise on numerical simulation and computers. I would also like to thank Grunde Jomaas for his countless help.

I want to specially thank my parents and sister for their love and support of my study. The debt of gratitude I owe them can never be paid off.

Finally, I want to express my most heartfelt gratitude to my wife, Ying Zhou, for her love, understanding and support. Her companionship has made the most difficult time joyful.

This research has been supported by the Air Force Office of Scientific Research under the technical monitoring of Dr. Julian M. Tishkoff.

This dissertation carries the number of 3177-T in the records of the Department of Mechanical of Aerospace Engineering.

Table of Contents

Chapter 1: Introduction

1.1. Overview

The present study is concerned with the oscillation phenomena in flames, in particular those driven by the intrinsic thermal-diffusive instability in diffusion flames and the thermo-acoustic instability in premixed flames. As such, this dissertation will be presented within the context of flame instabilities in both diffusion and premixed flames. In addition, since oscillations in diffusion flames have been primarily observed near the extinction state while radiative heat loss has been known to play an important role in both the flame oscillation and extinction behavior [1-5], the present study is therefore also concerned with the extinction characteristics of radiation-affected diffusion flames.

Combustion processes are governed by the equations of fluid mechanics that describe the conservation of mass, momentum and energy, supplemented by the species conservation equations expressing the mass balance of the species involved in the chemical reaction. These equations are, in general, highly nonlinear, multidimensional and strongly coupled. Thus, investigations often resort to simplified theories in order to gain fundamental understanding of various combustion processes.

In a certain sense, modern combustion theory started from the paper by Zeldovich & Frank-Kamenetski [6], in which the analytical formulas for the velocity and structure of a planar stationary flame supported by an Arrhenius reaction were derived by recognizing that the overall activation energy of the reaction is large in comparison to the available thermal energy. This work pioneered the concept of exploiting the physical

knowledge of the flame structure in order to make mathematical simplifications and, as a result, has led to the development of activation energy asymptotics extensively used in theoretical studies to this day [7].

The flame, though an entirely deterministic system, is capable of spontaneously developing irregular spatio-temporal behavior that can also be chaotic under certain physico-chemical conditions [8-13]. These unstable flame phenomena, often manifested in the forms of cells, ridges or pulsations over the flame surface, lead to various multidimensional patterns on the otherwise smooth or stationary flame front. The next important step in the development of combustion theory is the Darrieus-Landau (DL) solution for flame instability, in which an infinitely thin planar flame front is shown to be absolutely unstable against any perturbation as a consequence of density jump across the flame [14, 15]. Thus, a flame cannot propagate as a planar stationary front, but instead it becomes cellular, sometimes nonstationary and even turbulent. The DL theory, also known as that of hydrodynamic instability, however, ignores the structure of the flame such that it is not valid for perturbations of short wavelength that is comparable to the flame thickness [8, 13]. This has led to a great deal of work since the 1940s to improve the DL theory by incorporating the effects of finite flame thickness and the transport processes within the flame zone [16-22].

In addition to the DL hydrodynamic mechanism, Sivashinsky [23] developed a thermal-diffusive theory by assuming constant density, and showed that cellular flame fronts can also develop in mixtures with $Le < 1$ in the absence of hydrodynamic effect, where the Lewis number, Le, is defined as the ratio of the thermal diffusivity of the mixture to the mass diffusivity of the deficient species. Furthermore, Sivashinsky [23]

found that a planar flame may propagate in the form of pulsating fronts for mixtures with sufficiently large Lewis numbers. These flame instabilities, either cellular or pulsating, result from the imbalance between the thermal and mass diffusion, and hence are referred to as the thermal-diffusive instability. In the present state, various flame instabilities in premixed flames have been extensively studied and the underlying mechanisms are relatively well understood.

Unlike premixed flames, diffusion flames do not propagate, but rather are fixed within the neighborhood of the stoichiometric surface at which the fuel and oxidizer meet. Thus, diffusion flames are relatively stable and the instabilities observed in premixed flames are generally believed to be absent in diffusion flames. However, recent experiments have also identified some fascinating unstable behaviors in diffusion flames, especially near the extinction state [1-4, 24-29]. For example, flame strips and oscillations have been reported in both hydrogen and hydrocarbon/air diffusion flames in experiments involving a variety of configurations, such as candle and jet flames. These observed striped and oscillating flames are primarily driven by the thermal-diffusive instability, and thermal expansion does not play a crucial role [13]. Consequently, most theoretical studies on instabilities in diffusion flames adopted the constant density approximation to simplify the analysis and capture the major physics [30-38]. However, even within this framework, the problem is still rather complicated because of the large number of parameters involved, including those associated with both the reactant properties and flow conditions [13]. Thus, compared to the well understood premixed flame instabilities, there have been relatively few theoretical studies of diffusion flame dynamics. Therefore one of the primary objectives of this dissertation is to remedy this

deficiency and study, in particular, flame oscillations in diffusion flames driven by the thermal-diffusive instability.

Since, as indicated above, combustion theory was mainly developed from the study of premixed flame dynamics that are richly endowed with instability phenomena, in the following we shall first present an overview of flame instabilities in premixed, which will then be followed by a discussion on the instability of diffusion flames. Flame oscillations resulting from the imposed unsteady flow variations will also be discussed within the context of flame instabilities because in some cases they act as the key elementary process in the development of flame instabilities. Then, the objectives and outline of this dissertation will be presented.

1.2. Premixed Flame Instabilities

Flame instabilities arise in combustion processes in many different forms. They can be classified as intrinsic instabilities, such as hydrodynamic instability and thermal-diffusive instability, which are developed from the combustion processes irrespective of the combustion chamber, or chamber instabilities, such as thermo-acoustic instability, which are developed from the interaction of the combustion processes with the chamber [7]. In the following, theses instabilities will be discussed separately.

1.2.1. Hydrodynamic Instability

Hydrodynamic instability is caused by the density difference between the burned and unburned gases due to thermal expansion [7]. Its physical explanation is shown in Fig. 1.1. The flame front is assumed to be infinitely thin and propagates normal to itself with a

constant speed. When the flame is perturbed as shown, the streamlines leading to the convex section of the flame with respect to the unburned gas diverge, while those leading to the concave section converge. As a result, the velocity of the flow between the diverging streamline decreases, while the velocity between the converging streamlines increases. Therefore, the flame cannot balance the incoming flow, and as such is unstable to the perturbations that wrinkle the flame. Within this framework, Darrieus [14] and Landau [15] made the first analysis on flame instability and derived a dispersion relation relating the perturbation growth rate σ to its wavenumber k as

$$\sigma = \Omega_0 s_b k$$
$$\Omega_0 = (\sqrt{\epsilon + \epsilon^2 - \epsilon^3} - \epsilon)/(1+\epsilon)$$

where $\epsilon = \rho_b/\rho_u$ is the ratio of the densities of the burned and unburned gas and s_b the flame velocity relative to the burned gas. It is seen that for all $\epsilon < 1$ the growth rate σ is always positive for any wavenumber k, indicating that flames are unconditionally unstable and hence cannot sustain a smooth front. However, this is in conflict with the fact that smooth fronts have been observed in small scale experiments, implying that they are stable to perturbations of short wavelength [16, 39-41]. For this reason, subsequent work on hydrodynamic instability was aimed at correcting the DL theory for short-wave perturbations by taking the flame structure into consideration. Specifically, Markstein [16] incorporated the effects of finite flame thickness by relating the flame speed to the local curvature of the flame front through a phenomenological constant, ℓ, called the Markstein length. Linear stability analysis shows that the Markstein theory yields stabilization of short-wave perturbations, which explains the existence of small scale planar flame fronts. However, the Markstein length cannot be determined by such a phenomenological

approach. Istratrov & Librovich [17] then realized that this problem is characterized by two disparate length scales, the diffusion length ($\ell_D = D_{th}/s_u$) and the hydrodynamic length ($\Lambda = 2\pi/k$), which respectively characterize the length scales of the flame thickness and flame geometry, where D_{th} is the thermal diffusivity of the mixture and s_u the laminar flame speed with respect to the unburned gas. Utilizing this multiscale feature, Matalon & Matkowsky [18] performed a rigorous asymptotic analysis of the flame structure and solved the Markstein length, ℓ, in terms of the physico-chemical properties of the mixture.

Then reconsideration of the linear stability analysis yields a dispersion relation in the form

$$\sigma = \Omega_0 s_b k - \Omega_1 D_{th} k^2 \tag{1.1}$$

where Ω_1 is determined by the Lewis number, Le, the density ratio, ϵ, and the Zeldovich number $\beta = E(T_b - T_u)/RT_b^2$, E is the activation energy, R the universal gas constant and T_b and T_u are the temperatures of the burned and unburned gases, respectively. Thus, the second term in the RHS of Eq. (1.1) represents a correction to the DL result. For $\Omega_1 > 0$ this correction term has a stabilizing effect for short-wave perturbations with wavenumber $k > k_c = \Omega_0 s_b/\Omega_1 D_{th}$, which agrees with the Markstein's phenomenological theory. Similar results were also obtained by Pelcé & Clavin [20] and Frankel & Sivashinsky [21], respectively.

1.2.2. Thermal-Diffusive Instability

Thermal-diffusive instability arises in flames as a result of the imbalance between the thermal and mass diffusion, i.e. for Lewis number differing from unity, $Le \neq 1$. There are

two modes of thermal-diffusive instability, cellular and pulsating, which respectively occur for $Le < 1$ and $Le > 1$.

Zeldovich [42] proposed a theory, as shown in Fig. 1.2a, to qualitatively explain the cellular instability. It should be noted that the length scale of the wrinkles is of the order of the flame thickness ℓ_D, since it is at this scale that the diffusion processes become important. This is in contrast to the hydrodynamic theory in which the transverse scale of the wrinkles, Λ, is much larger than the flame thickness. It is seen from Fig. 1.2a that in the convex section of the flame with respect to the unburned gas, mass diffusion of the reactants into the reaction zone is focused and as such tends to strengthen the flame. However, the convex front has the opposite effect on heat conduction, which consequently weakens the flame. The net effect of these two phenomena depends on the relative rates of heat and mass diffusion, i.e. the Lewis number, *Le*. For $Le < 1$, the effect of mass diffusion is stronger than that of heat conduction such that the convex section of the flame front becomes stronger and propagates faster, while, by the same reasoning, the concave section weakens and propagates slower, leading to a cellular flame front. For $Le > 1$, the effect is opposite and hence the flame is cellularly stable. However, for flames with $Le > 1$, pulsating flame front may develop as a consequence of the unequal rate of mass diffusion and heat conduction. Figure 1.2b shows the simplified structure of a planar flame with the profiles of temperature and deficient species for $Le < 1$ and $Le > 1$, respectively. For $Le < 1$, if the reaction zone is positively perturbed with respect to the flame front, upstream heat conduction is increased by a larger extent than mass diffusion into the reaction zone, as evidenced by the steeper slope of the temperature profile. Consequently, the flame is weakened and the reaction zone relaxes back to its original

position. Similarly, a negative perturbation strengthens the flame and leads it back to the original position again. However, for $Le > 1$, by the same argument, a positive perturbation will strengthen the flame such that the reaction zone tends to outrun the flame front, recognizing nevertheless that it is bounded by the finite thickness of the preheat zone. As a consequence, the flame will propagate in a pulsating manner.

Although the motion of a flame front is always accompanied by the motion of the local flow field, the above qualitative theory implies that the hydrodynamic effect plays a secondary role for the thermal-diffusive instability. As such, theoretical studies have often adopted a constant density approximation, also referred to as the thermal-diffusive model, to simplify the analysis and capture the controlling physics [23, 43-44]. In this way, the flame is a passive front in a prescribed flow field and the system is governed only by energy and species conservation equations. Using this model, Barenblatt *et al.* [43] performed a linear analysis for the cellular mode of the thermal-diffusive instability in a planar flame subject to long-wave perturbations, and derived the following dispersion relation

$$\sigma = D_{\text{th}}\left[\tfrac{1}{2}\beta(1-Le)-1\right]k^2$$

It is seen that for $Le < Le_c = 1 - 2/\beta$, the flame is unstable to any perturbation and becomes stable as $Le > Le_c$. The stability boundary Le_c is slightly less than unity because in additional to nonequidiffusion, pure curvature effects tends to smoothen the flame front by decreasing the flame speed at the convex section and increasing at the concave section [45]. This shifts the stability boundary for Le from unity to a slightly smaller value. Subsequently, Sivashinsky [23] incorporated the relaxation effects of short-wave

perturbations and derived a dispersion relation for $Le \approx Le_c$ using large activation energy asymptotics as

$$\sigma = D_{\text{th}}\left[\tfrac{1}{2}\beta(1-Le)-1\right]k^2 - 4D_{\text{th}}\ell_D^2 k^4$$

Thus, when the flame is unstable, i.e. $Le < Le_c$, there exists a critical wavenumber k_c that corresponds to the fastest growing mode of the perturbation and hence determines the critical size of cells as they begin to develop over the flame front. Sivashinsky [23] also determined a criterion for the occurrence of the planar pulsating mode of thermal-diffusive instability:

$$\beta(Le-1) > 4(1+\sqrt{3}) \approx 10.9 \tag{1.2}$$

When the flame is corrugated the expression in Eq. (1.2) is slightly below 10.9. Since typical values of β and Le of gaseous systems cannot satisfy Eq. (1.2), it is concluded that pulsating instability cannot be observed in gaseous combustion. Joulin & Clavin [44] extended Sivashinsky's theory by considering the effect of heat loss. They found that with increasing heat loss the parameter range for the pulsating instability to occur increases and becomes accessible for gaseous combustion. This theoretical prediction was then experimentally verified by Gololobov *et al.* [46] in spinning acetylene decomposition flames. In addition, Joulin & Clavin [44] found that the cellular flame boundary Le_c increases with increasing heat loss and approaches unity at the flame extinction limit. Sivashinsky [8, 47] further studied the nonlinear development of the disturbed flame front and derived an evolution equation for the amplitude of the perturbation for $Le \approx Le_c$, which is known as the Kuramoto-Sivashinsky equation. The nonlinear effect in the evolution of the disturbed flame is shown to be of a purely kinematic nature. Numerical integration of this equation shows that a disturbed planar

flame ultimately evolves into a cellular flame with cells being in a state of continual chaotic self-motion [48].

1.2.3. Thermo-Acoustic Instability

The combustion-driven thermo-acoustic instability results from the resonant coupling between the unsteady combustion process and the natural acoustic modes of the combustor [7]. Unsteady heat release generates acoustic waves which will then be reflected from the chamber walls and interact with the combustion process. Since the combustion process is sensitive to flow variations, a feedback loop is created and combustion instability may occur if the phase between the acoustic waves and the unsteady combustion satisfies certain conditions. A criterion for the emergence of thermo-acoustic instability was proposed by Rayleigh in 1878 [49]. It states that when heat is released locally and periodically in a gaseous fluid, an acoustic oscillation is amplified if the heat release and pressure oscillations are in phase with each other. Thermo-acoustic instability usually manifests in the form of sustained oscillations in pressure, heat release rate and flow rate. It caused serious problems during the early stage in the development of solid and liquid propellant rocket engines [50], and nowadays is still practically important due to the requirement for developing lean premixed combustors with low NO_x emission, which are susceptible to instabilities [51]. Thus, it is one of the major concerns of the present study.

While thermo-acoustic instability occurs as a consequence of the two-way coupling between the combustion heat release and acoustic waves, its theoretical description is usually approached by emphasizing one of the two-way processes in the

coupling mechanism, i.e. considering acoustics or combustion as the central process [52]. The former employs a wave equation for the reacting flows and derived a unified framework for the analysis of combustion oscillations. Thus, the difficulty in describing the response of the flame to acoustic wave modulation is avoided. The latter emphasizes the flame motion in an unsteady flow field and its response to flow perturbations. In its simplest form, the flame can be considered as a moving surface anchored at a specific location in a duct with a constant cross-section area, and hence can be described by the level-set equation, known as the G-equation [53]. Of particular interest is how the rate of heat release responds to an acoustic perturbation. This problem has been addressed by a number of studies [54-66]. Specifically, Fleifel *et al.* [54] studied the linear response of laminar premixed flames to flow oscillations under the assumption of constant flame speed. The results showed flame wrinkling in the form of convective wave is induced by flow oscillations. The response of the flame is evaluated by the flame transfer function defined as the ratio of the relative heat release oscillation to the relative flow oscillation. Its magnitude and phase depend primarily on the flame Strouhal number, which is defined as the oscillation frequency normalized by the ratio of the laminar flame speed to the duct radius. In terms of this number, high frequency perturbation passes through the flame while low frequencies induce stronger responses. Ducruix *et al.* [55] then conducted a measurement for the flame transfer function in an axisymmetric conical flame and compared the results with the theory. Good agreement was obtained for low perturbation frequencies. However, the phase difference showed increased discrepancy at larger frequencies. Schuller *et al.* [56] extended the theory of Fleifel *et al.* [54] to include the convective effects of the flow modulations propagating upstream of the flame and the

results showed improved agreement with the experiments. Dowling [57] studied the nonlinear response of a premixed ducted flame to velocity perturbations of large amplitude and examined, in particular, the nonlinear process that controls the finite amplitude of the heat release oscillations. It was found that once the amplitude of the velocity fluctuation exceeds its mean, i.e. when the flow velocity reverses, the oscillation in heat release rate saturates, leading to finite-amplitude limit cycles. This mechanism constitutes the major nonlinearity of the system. Lieuwen [58] further studied the nonlinear response to harmonic velocity perturbations, and showed that due to nonlinearities, the amplitude of the transfer function relative to its linear value decreases with increasing amplitude of the velocity perturbation. The nonlinearity is more evident for high frequency perturbations and for flames with more surface area close to the anchoring position.

These analyses, however, assumed that the flame speed is constant, independent of flame stretch. This then implies that the heat release responds to flow oscillations only through modulations of the flame surface area. Since the local flame propagation speed and hence the local burning rate are actually affected by perturbations, it is reasonable to expect that oscillations of the heat release rate are correspondingly affected. In particular, since the wavelength of the flame wrinkling induced by the flow oscillation scales inversely with the perturbation frequency [54-56], variations in stretch-induced flame speeds are expected to become significant at high frequencies and responsible for some of the experimentally observed phenomena. For example, Baillot and co-workers [59-61] performed a systematic study of the response of Bunsen flames of methane–air mixtures to velocity oscillations of varying amplitudes and frequencies. It was found that, at low

disturbance frequencies and small amplitudes, the flame front wrinkles symmetrically about the burner axis. At higher frequencies but similar low amplitudes, a phenomenon referred to as "filtering" was observed, wherein the flame wrinkling was evident only at the flame base and decayed with streamwise location downstream. Lieuwen [67] suggested that this behavior could result from the growing significance of flame speed variation along the flame due to the small radii and hence strong curvature of the flame wrinkles at high disturbance frequencies. It is noted that Baillot *et al.* [59-61] neither provided photographic images nor suggested the possible mechanisms responsible for this behavior. Thus, this dissertation will address this problem and study particularly the role of flame stretch through the curvature of the flame wrinkles on the premixed flame response to flow oscillations.

1.3. Diffusion Flame Instabilities

Unlike the instabilities in premixed flames, which may result from different mechanisms, instabilities in diffusion flames are mainly driven by thermal-diffusive effects [13]. Thus the discussion on diffusion flame instabilities will be limited in the scope of thermal-diffusive instability. Furthermore, since these instabilities have been mostly observed near the extinction state, in the following we shall first discuss the extinction characteristics of diffusion flames, especially in the presence of radiative heat loss. Then, the experimental observations and theoretical analyses for the thermal-diffusive instability in diffusion flames will be presented. Finally, we will discuss forced flame oscillations in diffusion flames by the imposed unsteady flow variations and their coupling with the intrinsic flame oscillations driven by the thermal-diffusive instability.

1.3.1. Extinction Characteristics

The structure and extinction characteristics of diffusion flames in the absence of volumetric heat loss were first rigorously analyzed using large activation energy asymptotics in a seminal paper by Liñán [68]. It is shown that the flame structure and response are primarily controlled by the system Damköhler number, *Da*, defined as the ratio of the diffusion time to the reaction time, and that there exists a minimum *Da*, and consequently a maximum flow rate, beyond which steady burning is not possible due to insufficient time for adequate reaction to occur in order to maintain the flame structure. This feature can be demonstrated by a plot of reactant leakage (or flame temperature) versus *Da*, as shown in Fig. 1.3. It is seen (from the lower branch) that as $Da \to \infty$ the reactant leakage diminishes as a result of complete reaction. In this limit the chemical reaction with large activation energy occurs within an infinitely thin reaction zone. But with decreasing *Da*, the reaction zone thickens and the reaction becomes incomplete leading to an increase in the leakage of one or both reactants until the Damköhler number *Da* reaches the minimum value, Da_{ext}, which corresponds to the extinction state.

Extinction can be further promoted in the presence of radiative heat loss [69-71]. In particular, because the extent of radiative loss increases with increasing flame volume and thereby flame thickness, and because flame thickness increases with decreasing flow rate and hence increasing *Da*, extinction is expected to be facilitated with increasing *Da*. Consequently, in addition to the extinction limit at the minimum *Da*, there should exist another extinction limit at a maximum *Da*, above which steady burning is also not possible. The possible existence of the dual extinction limits at lower and higher

Damköhler numbers, hereafter respectively referred to as the kinetic and radiative extinction limits, was first suggested and numerically demonstrated by T'ien *et al.* [72]. It was later theoretically confirmed by Chao *et al.* [73] using large activation energy asymptotics, and experimentally verified by Maruta *et al.* [5]. Their results are summarized in Fig. 1.4, in which the variation of the reactant leakage with *Da* in the presence of radiative loss is plotted. It is seen that with increasing *Da* from the kinetic extinction limit, $Da_{E,K}$, the reactant leakage first decreases as a result of increased reaction rate, and then increases as a result of increased radiative heat loss, and finally reaches the radiative extinction limit, $Da_{E,R}$. Thus, steady burning is only possible within a limited range of *Da*, namely $Da_{E,K} < Da < Da_{E,R}$. Although so far this feature has been analyzed in a couple of papers [5, 72-76], a rigorous theoretical description for the radiation-affected diffusion flames has not been attempted. Specifically, these analyses [72-75] missed considering the excess/deficiency of the total enthalpy in the reaction zone, hereafter referred to as the excess enthalpy [77]. Although inclusion of the excess enthalpy does not lead to qualitative differences in the extinction results, it has been shown that it is a crucial element in the study of thermal-diffusive instability in diffusion flames [13]. Furthermore, these analyses adopted either unity [73-74] or near-unity [75] reactant Lewis numbers, which apparently are not appropriate for the study of thermal-diffusive instability that is usually driven by the non-unity reactant Lewis numbers. Thus, in this dissertation a rigorous analysis of the extinction characteristics of radiation-affected diffusion flames will be first presented prior to the study of thermal-diffusive instability.

1.3.2. Thermal-Diffusive Instability

1.3.2.1. Experimental Observations

The earliest observation of diffusion flame instability is probably by Gardisde & Jackson [24]. They observed that the surface of a hydrogen-air jet flame was formed of triangular cells in the shape of a polyhedron at relatively high flow rates when the hydrogen was sufficiently diluted with nitrogen or carbon dioxide. The cells at the base of the flame were approximately 0.7 cm in width. Later, Dongworth & Melvin [25] carried out experiments using a splitter-plate burner and observed a cellular appearance at the base of a hydrogen–oxygen diffusion flame at sufficiently high flow velocities and when the hydrogen is diluted with nitrogen or argon, but not with helium. The cells were about 1 cm in length. Ishizuka & Tsuji [26] reported a similar behavior in a counterflow hydrogen–oxygen diffusion flame. They observed that when hydrogen, injected through the wall of a porous cylinder in a vertically approaching uniform air stream, is diluted with a heavier gas, such as nitrogen or argon, the diffusion flame surface that is normally wrapped around the cylinder breaks up into stripes and leaves regularly spaced extinguished regions along the cylinder axis. These observations were rather accidental discovery than intended realization from systematically designed experiments. Chen *et al.* [27] were the first to systematically study the occurrence of cellular diffusion flames in a variety of fuels and diluents and for various initial mixture strengths, defined as the fuel-to-oxidizer mass fraction ratio in their respective supplying streams normalized by the mass-weighted stoichiometric coefficient ratio. They found that far from extinction, no flames develop cellular or striped structures. Cellular flames were formed at near-extinction conditions when the Lewis number of the more completely consumed reactant

was sufficiently less than unity. Depending on the conditions, the observed cells have the dimension of about 0.7-1.5 cm. Lo Jacono *et al.* [28] then studied hydrogen–oxygen jet flames diluted with carbon dioxide and examined, in particular, the influence of the initial mixture strength on the formation of the cellular flames. It was found that the parameter space for the cellular instability increases with decreasing initial mixture strength. Furthermore, for a given initial mixture strength, several cellular states were found to co-exist near the extinction limit, and the preferred number of cells decreased with decreasing Damköhler number. Recently, Lo Jacono *et al.* [29] introduced a porous plug counter-diffusion (PPCD) burner, which is able to produce a one-dimensional unstrained planar flame and hence facilitates the direct comparison of experiments with theory and simulation. Utilizing this burner, similar results as those in Lo Jacono *et al.* [28] were obtained.

In addition to the cellular patterns in diffusion flames, flame oscillations have also been reported in experiments involving a variety of configurations. Chan & T'ien [1] conducted experiments for a range of condensed-phase (liquid and solid) fuels, such as kerosene, heptane, ethanol, methanol and polyethylene, in different flame geometries. In most cases, spontaneous flame oscillations that last a couple of cycles with increasing amplitude were observed before flame extinction. Similarly, Ross *et al.* [2] observed oscillations in candle flames near the extinction limit in microgravity condition.. Nayagam & Williams [3] conducted experiments for microgravity droplet flame in the Space Shuttle. Relatively persistent flame oscillations of eight cycles were observed before extinction in the weak transport limit. Thus, this flame oscillation appears to be triggered near the radiative extinction limit induced by the excessive radiative loss at

large *Da*. Recently, Füri *et al.* [4] systematically studied the conditions for the onset of near-limit flame oscillations in gaseous jet diffusion flames. It was found that the reactant Lewis numbers and the initial mixture strength are the key parameters governing flame oscillations. The tendency for flame oscillations to occur increases with decreasing initial mixture strength and increasing reactant Lewis numbers, which are typically larger than unity.

1.3.2.2. Theoretical Analysis

The above experimental observations suggest that instability analysis in diffusion flames is more complex than its counterpart in premixed flames, although many of the traits observed are quite similar. First, unlike premixed flames, which is characterized by a single Lewis number, for diffusion flames there are two effective Lewis numbers, Le_F and Le_O, associated with the fuel and oxidizer, respectively; the different individual role they play in the stability consideration has been confirmed by the experiments [27]. Second, all cellular and pulsating flames were observed near the extinction state, implying that the flow conditions, i.e. the Damköhler number, *Da*, is an important parameter that controls, among others, the onset of flame instability. Third, the initial mixture strength, ϕ, was shown to play an essential role in the development of instability, especially in the determination of the specific mode of thermal-diffusive instability. For example, cellular and pulsating instabilities have been shown to be more likely to form at larger and smaller ϕ, respectively. Finally, other parameters, such as the temperature differential between the supplying streams of the fuel and oxidizer, ΔT, and the radiative heat loss, may also have important effects on flame instability behaviors. Therefore, a

complete theory on the stability of diffusion flames needs to take all these parameters into consideration, and hence tends to be more complex than that of premixed flames. Consequently, compared to the well-understood premixed flame instabilities, there have been relatively few theoretical investigations of diffusion flame instabilities. Kirkby & Schmitz [30] examined numerically the response of a planar diffusion flame to one-dimensional perturbations, and were the first to show that flame oscillations resulting from the thermal-diffusive instability may develop when the Lewis numbers are greater than unity and/or there is appreciable heat loss. Cheatham & Matalon [31-32] studied the dynamics of a spherical diffusion flame in a reduced oxidant environment. They identified that spontaneous flame oscillations can be triggered either by sufficiently large Lewis numbers (even without heat loss) or by excessive heat loss (even for unity Lewis numbers). The predicted oscillation frequency is typically of the order of 1 Hz, which is consistent with the experiments. The first theoretical study of the cellular mode of thermal-diffusive instability in diffusion flames is by Kim *et al.* [33]. They performed a linear stability analysis for a one-dimensional convective-diffusive diffusion flame using large activation energy asymptotics. The Lewis numbers of the fuel and oxidizer were assumed to be identical and sufficiently smaller than unity. The initial mixture strength was fixed at unity and convection was towards the oxidizer. However, the derived dispersion relation shows that the characteristic size of the cells at the onset of instability is comparable to the thickness of the reaction zone, which is much smaller than the expected diffusion length scale. Thus, in follow-up studies, Kim [34-35] adopted near-unity Lewis numbers, namely $1 - Le \sim O(\beta^{-1})$, and claimed that the development of cells with the critical size of diffusion length scale is only possible under this limit and near

extinction condition, namely $Da_{Cr} - Da_{ext} \sim O(\beta^{-1})$, where Da_{Cr} is the critical Damköhler number corresponding to the marginally stable state and Da_{ext} is the extinction Damköhler number.

The most comprehensive theory of the diffusion flame dynamics was proposed by Cheatham & Matalon [36], in which all the above mentioned parameters, Le_F, Le_O, ϕ, ΔT, and Da, are taken into consideration in the limit of large activation energy for a one-step overall reaction. By resolving the internal structure of the reaction zone, Cheatham & Matalon [36] derived the required conditions for the determination of the temperature and mass fractions of the fuel and oxidizer, as well as the instantaneous shape of the reaction sheet, in the form of jump and leakage conditions. The stability analysis of a planar flame using this model shows that flames with infinitely fast reaction ($Da \rightarrow \infty$) or unity reactant Lewis numbers ($Le_F = Le_O = 1$) are unconditionally stable. The cellular instability with critical cell size comparable to the diffusion length scale tends to occur in "fuel-lean" systems for $Da_{ext} < Da < Da_{Cr}$, where the critical Damköhler number satisfies $Da_{Cr} - Da_{ext} \sim O(1)$, which is different from the results of Kim [33-35]. However, smaller cells that scale on the thickness of the reaction zone are also possible near extinction conditions, i.e. $Da_{Cr} \approx Da_{ext}$. This model was then utilized by Kukuck & Matalon [37] to study the onset of flame oscillations in a planar diffusion flame. The results show that oscillations develop when the Damköhler number is sufficiently small, namely at near-extinction conditions, and when the reactant diffusing against the stream is more completely consumed and the corresponding Lewis number is sufficiently large, typically larger than one. The effect of radiative heat loss was also studied and it was shown that increased heat loss enhances the onset of instability. The predicted oscillation frequency

is typically 1 – 6 Hz. However, high frequency oscillations are also possible just prior to extinction.

The above investigations confirmed the experimental observations [1-4, 24-29]. Matalon [13, 38] unified the above theoretical results in a fuel-oxidizer Lewis number parameter plane, as shown in Fig. 1.5. The occurrence of the specific mode of thermal-diffusive instability is related to two parameters, h_f and γ. The parameter h_f, also referred to as the excess enthalpy, represents the available enthalpy in the reaction zone. As shown in Fig. 1.5, the curve $h_f = 0$ separates regions of excess (below the curve) and deficiency (above the curve) in available enthalpy and always includes the point, $Le_F = Le_O = 1$. It is seen that h_f is always negative when both Lewis numbers are smaller than unity, and positive when they are larger than unity or either of them is sufficiently large. The parameter γ represents the effective mixture strength in the reaction zone and varies from negative values for lean conditions, to positive values for rich conditions. Thus, the line $\gamma = 0$ separates regions of relatively lean (to the left) or rich (to the right) mixtures. The entire parameter plane is divided into several regions by $h_f = 0$ and $\gamma = 0$, and different types of instability are expected in different regimes. Stationary cells are primarily observed in fuel lean systems ($\gamma < 0$) when there is excess in available enthalpy ($h_f > 0$). The characteristic cell size is comparable to the diffusion length scale. However, as $\gamma \sim 0$, i.e. for near stoichiometric conditions, the cells are much smaller and scale on the reaction zone thickness $\ell_R = \beta^{-1}\ell_D$. Kim's analysis [33] falls into this regime as a result of the limited parameters used (γ slight larger than 0). In this case, perturbation intrudes into the reaction zone and a separate analysis that incorporates small wavelength

perturbations evolving on the fast time scale, $t_R = \beta^{-2} t_D$, is required [78]. These high-frequency modes, also referred to as 'fast-time' instabilities, are limited to conditions very near the extinction limit, namely $Da_{Cr} \approx Da_{ext}$, whereas ordinary cells with characteristic size comparable to the diffusion length are predicted to occur over a wider range of Damköhler number, namely $Da_{Cr} - Da_{ext} \sim O(1)$. In contrast to the stationary cells, flame oscillations tend to develop in fuel rich systems ($\gamma > 0$) with deficiency in enthalpy ($h_f < 0$). When the Lewis numbers of the two reactants are larger than one, or one of them is near or even below one and the other sufficiently larger than one, the fastest growing mode corresponds to the zero wavenumber resulting in planar oscillations. For small Le_F, the fastest growing mode corresponds to a finite wavenumber. Thus, the oscillating cell is also a possible mode of thermal-diffusive instability in diffusion flames, although it will not be discussed in this dissertation. Finally, the competing modes of instability are also possible in the domain separating these regimes, as shown in Fig. 1.5.

The above linear analyses provide a rather detailed map for the occurrence of thermal-diffusive instability in diffusion flames. However, they are only concerned with the initial growth of flame instabilities under infinitesimal perturbations. As the perturbations grow to finite amplitude, nonlinear effects become important and may limit the further growth of perturbations. As such, the flame behavior subsequent to the onset of flame instabilities must be determined by a nonlinear analysis. In addition, these studies are primarily focused on flame instabilities near the kinetic extinction limit in adiabatic or weakly radiative diffusion flames. As we have shown, in the presence of substantial radiative heat loss, there exist dual extinction limits, namely kinetic and radiative limits, at small and large Damköhler numbers, respectively. Being near-limit

phenomena, flame instabilities in diffusion flames are expected to develop near both extinction limits and the instabilities near these limits are also expected to possess different behavior, as evident by the experiment of Nayagam & Williams [3]. Therefore, this dissertation will address these two aspects of flame instabilities, and study, in particular, the nonlinear behavior of flame oscillations in adiabatic diffusion flames and the occurrence of flame oscillations near the radiative extinction limit in radiation-affected diffusion flames.

1.3.3. Flame Response to Flow Oscillations

The flame oscillations studied in the above investigations arise intrinsically as a result of thermal-diffusive instability in diffusion flames. However, flames are often subjected to unsteady flow oscillations imposed either by the random motion of eddies in turbulence or by the system acoustics. Thus, the response of flames to flow oscillations has received considerable attention during the past few years. The studies primarily emphasized on the effects of strain rate oscillations [86-93]. In particular, results on diffusion flames show that the flame response becomes more sensitive to the imposed oscillations when the otherwise steady flame is near its extinction limit; whereas for flames far from extinction the flame response is attenuated monotonically as the frequency of the imposed oscillation increases. Consequently, unsteady flames can withstand higher strain rates at higher frequencies than at lower frequencies. However, among these investigations, theoretical ones are relatively few. Strahle [86] studied the convective droplet burning at a stagnation point under the influence of small amplitude sound wave from the free stream. Im *et al.* [92] analyzed the response of counterflow diffusion flames to

monochromatic oscillatory strain rates using large activation energy asymptotics. Attention was focused on near extinction conditions so that the time scale of the imposed unsteadiness is comparable to that of diffusive transport. The results of Im *et al.* [93] suggest that the unsteady characteristics of the near-extinction diffusion flame can be significantly different from those in the reaction-sheet limit.

These earlier studies, however, have not addressed the important issue of resonance. That is, combustion systems may exhibit intrinsic oscillations and these oscillations may then interact with the imposed flow oscillations so that the flame responses could be significantly different. Furthermore, if considering the intrinsic oscillations, those thermal-diffusively unstable flames could extinguish at a larger Damköhler number corresponding to the marginally stable state, Da_{Cr}, also denoted as the dynamic extinction Damköhler number, instead of at the static extinction Damköhler number, Da_{ext}, considered in previous studies. Thus, in this dissertation we shall address this specific problem and study, in particular, the possible resonance between the intrinsic and forced flame oscillations for flames with Damköhler number close to the dynamic extinction (stability) limit, Da_{Cr}.

1.4. Objectives and Outline

As reviewed in the previous section, this dissertation addresses the following flame oscillation and extinction problems.

First, in Chapter 2 we carry out a systematic nonlinear analysis for flame oscillations in chambered planar diffusion flames without volumetric heat loss. This analysis is based on the linear analysis of Kukuck & Matalon [37]. A bifurcation analysis

near the neutral stability limit is conducted and a nonlinear evolution equation of the Landau type for the amplitude of perturbation is derived. The various possible burning regimes are then mapped in parameter space

In Chapter 3, this analysis is extended to incorporate imposed flow oscillations and studies, in particular, their coupling with intrinsic oscillations. The linear response of flames to the imposed oscillations is first examined and the resonant coupling between the forced and intrinsic flame oscillations is identified. Then the nonlinear response is examined by deriving an evolution equation for the amplitude of flame response.

The analysis for flame oscillations in diffusion flames is extend to radiation-affected flames. Due to the absence of a rigorous theory for the dynamics of radiation-affected diffusion flames with the proper consideration of the excess enthalpy, in Chapter 4 we shall first develop a model for planar diffusion flames with distinct reactant Lewis numbers and radiative heat loss. This model is then utilized to systematically study the dual extinction characteristics of a counterflow diffusion flame.

In Chapter 5, using the above model the linear analysis for the flame oscillations in diffusion flames is extended to the radiation-affected flames. A dispersion relation relating the perturbation growth rate to the system parameters and radiative loss is derived. Using this dispersion relation, flame oscillations near both the kinetic and radiative extinction limits are studied and the role of radiative loss in the development of flame oscillations is identified.

In Chapter 6, the study on flame oscillations is extended to premixed flames. Motivated by understanding the driving mechanism of the thermo-acoustic instability, we study the linear response of a wedge-shaped flame to harmonic flow oscillations, and in

particular, examine the effects of flame stretch on the flame transfer function. An approximate but sufficiently accurate analytical solution for the perturbed flame location and the flame transfer function are first derived. Two nondimensional parameters characterizing the effects of flame stretch are then isolated by expanding the solutions in the limit of weak stretch.

Finally, in Chapter 7 we summarize the work and present recommendation for future research.

1.5. List of Publications

A good part of the dissertation research has been either published or accepted for publication. The materials contained in them are distributed in the dissertation, as follows.

Chapter 2: Wang, H. Y., Bechtold, J. K. and Law, C. K., "Nonlinear Oscillations in Diffusion Flames", *Combust. Flame* **145**: 376-389 (2006).

Chapter 3: Wang, H. Y., Bechtold, J. K. and Law, C. K., "Forced Oscillation in Diffusion Flames near Diffusive-Thermal Resonance", *Int. J. Heat Mass Transfer* (2007) (In press).

Chapter 4: Wang, H. Y., Chen, W. H. and Law, C. K., "Extinction of Counterflow Diffusion Flames with Radiative Heat Loss and Nonunity Lewis Numbers", *Combust. Flame* **148**: 100-116 (2007).

Chapter 5: Wang, H. Y. and Law, C. K., "On Intrinsic Oscillation in Radiation-Affected Diffusion Flames", *Proc. Combust. Inst.* **31**: 979-987 (2007).

Chapter 6: Wang, H. Y., Preetham, Kumar, T. S., Lieuwen, T. and Law, C. K., "Linear Response of Stretch-Affected Premixed Flames to Flow Oscillations", submitted for publication.

References

1. Chan, W. and T'ien, J., *Combust. Sci. Technol.* **18**: 139-143 (1978).
2. Ross, H. D., Sotos, R. G. and T'ien, J. S., *Combust. Sci. Technol.* **75**: 155-160 (1991).
3. Nayagam, V. and Williams, F. A., *7th Int. Conf. on Numerical Combustion*, New York (1998).
4. Furi, M., Papas, P. and Monkewitz, P. A., *Proc. Combust. Inst.* **28**: 831-838 (2000).
5. Maruta, K., Yoshida, M., Guo, H., Ju, Y. and Niioka, T., *Combust. Flame* **112**: 181-187 (1998).
6. Zeldovich, Y. B. and Frank-Kamenetski, D. A., *Acta Physicochimica URSS* **9**: 341-350 (1938).
7. Williams, F. A., Combustion Theory, 2nd edition, Addison-Wesley, Redwood City, CA (1985).
8. Sivashinsky, G. I., *Ann. Rev. Fluid Mech.* **15**: 179-199 (1983).
9. Clavin, P., *Prog. Energy Combust. Sci.* **11**: 1-59 (1985).
10. Buckmaster, J., *Ann. Rev. Fluid Mech.* **25**: 21-53 (1993).
11. Clavin, P., *Ann. Rev. Fluid Mech.* **26**: 321-352 (1994).
12. Liberman, M. A. and Bychkov, V. V., *Physics Reports* **325**: 115-237 (2000).
13. Matalon, M., *Ann. Rev. Fluid Mech.* **39**: 163-191 (2007).
14. Darrieus, G., Propagation d'uu Front de Flamme, communication presented at La Technique Moderne (1938).
15. Landau, L., *Acta Physicochimica URSS* **19**: 77-85 (1944).

16. Markstein, G. H., *Nonsteady Flame Propagation*, Pergamon Press, New York (1964).

17. Istratov A. G. and Librovich V. B., *Acta Astronau.* **14**: 453-467 (1969).

18. Matalon, M. and Matkowsky, B. J., *J. Fluid Mech.* **124**: 239-259 (1982).

19. Clavin, P. and Williams, F. A., *J. Fluid Mech.* **116**: 251-282 (1982).

20. Pelcé, P. and Clavin, P., *J. Fluid Mech.* **124**: 219-237 (1982).

21. Frankel, M. L. and Sivashinsky, G. I., *Combust. Sci. Technol.* **29**: 207-224 (1982).

22. Matalon, M., Cui, C., Bechtold, J. K., *J. Fluid Mech.* **487**: 179-210 (2003).

23. Sivashinsky, G. I., *Combust. Sci. Technol.* **15**: 137-146 (1977).

24. Gardside, J. E. and Jackson, B., *Nature* **168**: 1085 (1951).

25. Dongworth, M. R. and Melvin, A., *Combust. Sci. Technol.* **14**: 177-182 (1976).

26. Ishizuka, S. and Tsuji, H., *Proc. Combust. Inst.* **18**: 695-703 (1981).

27. Chen, R. H., Mitchell, G. B. and Ronney, P. D., *Proc. Combust. Inst.* **24**: 213-221 (1992).

28. Lo Jacono, D., Papas, P. and Monkewitz, P. A., *Combust. Theory Modelling* **7**: 635-644 (2003).

29. Lo Jacono, D., Papas, P., Matalon, M. and Monkewitz, P. A., *Proc. Combust. Inst.* **30**: 501-509 (2005).

30. Kirkby, L. L. and Schmitz, R. A., *Combust. Flame* **10**: 205-220 (1966).

31. Cheatham, S. and Matalon, M., *Proc. Combust. Inst.* **26**: 1063-1070 (1996).

32. Cheatham, S. and Matalon, M., *AIAA J.* **34**: 1403-1409 (1996).

33. Kim, J. S., Williams, F. A. & Ronney, P. D., *J. Fluid Mech* **327**: 273-301 (1996).

34. Kim, J. S., *Combust. Theory Modelling* **1**: 13-40 (1997).

35. Kim, J. S. and Lee, S. R., *Combust. Theory Modelling* **3**: 123-146 (1999).

36. Cheatham, S. and Matalon, M., *J. Fluid Mech.* **414**: 105-144 (2000).

37. Kukuck, S. and Matalon, M., *Combust. Theory Modelling* **5**: 217-240 (2001).

38. Metzener, P. and Matalon, M., *Combust. Theory Modelling* **10**: 701-725 (2006).

39. Tse, S. D., Zhu, D. L. and Law, C. K., *Proc. Combust. Inst.* **28**: 1793-1800 (2000).

40. Kwon, O. C., Rozenchan, G. and Law, C. K., *Proc. Combust. Inst.* **29**: 1775-1783 (2002).

41. Law, C. K., *Combust. Sci. Technol.* **178**: 335-360 (2006).

42. Zeldovich, Y. B., Theory of Combustion and Detonation of Gases, Academy Science, USSR, 1944 (in Russian).

43. Barenblatt, G. I., Zeldovich, Y. B. and Istratov, A. G., *Zh. Prikl. Mekh. Tekh. Fiz.* **4**: 21-26 (1962).

44. Joulin, G. and Clavin, P., *Combust. Flame* **35**: 139-153 (1979).

45. Bechtold, J. K. and Matalon, M., *Combust. Flame* **67**: 77-90 (1987).

46. Gololobov, I. M., Granovsky, E. A. and Gostinsev, Y. A., *Fiz. Goreniya Vzryva* **17**: 28-33 (1981).

47. Sivashinsky, G. I., *Acta Astronaut* **4**: 1177-1206 (1977).

48. Michelson, D. M. and Sivashinsky, G. I., *Acta Astronaut* **4**: 1207-1221 (1977).

49. Rayleigh, L., *The Theory of Sound*, Dover Publications, New York (1945).

50. Williams, F. A., Barrere, M. and Huang, N. C., Fundamental *Aspects of Solid Propellant Rockets*, AGARDograph No. 115, Slough, England: Technivision Services (1969).

51. Correa, S. M., *Proc. Combust. Inst.* **27**: 1793-1807 (1998).

52. Candel, S., *Proc. Combust. Inst.* **29**: 1-28 (2002).

53. Law, C. K., *Combustion Physics*, Cambridge University Press, New York (2006).

54. Fleifel, M., Annaswamy, A. M., Ghoniem, Z. A. and Ghoniem, A. F., *Combust. Flame* **106**: 487-510 (1996).

55. Ducruix, S., Durox, D. and Candel, S., *Proc. Combust. Inst.* **28**: 765-773 (2000).

56. Schuller, T., Durox, D. and Candel, S., *Combust. Flame* **134**: 21-34 (2003).

57. Dowling, A. P., *J. Fluid Mech.* **346**: 271-290 (1997).

58. Lieuwen, T., *Proc. Combust. Inst.* **30**: 1725-1732 (2005).

59. Bourehla, A. and Baillot, F., *Combust. Flame* **114**: 303-318 (1998).

60. Baillot, F., Bourehla, A. and Durox, D., *Combust. Sci. Technol.* **112**: 327-350 (1996).

61. Baillot, F., Durox, D. and Prud'homme, R. *Combust. Flame* **88**: 149-168 (1992).

62. Boyer, L. and Quinard, J., *Combust. Flame* **82**: 51-65 (1990).

63. Dowling, A. P., *J. Fluid Mech.* **394**: 51-72 (1999).

64. Durox, D., Baillot, F., Searby, G. and Boyer, L., *J. Fluid Mech.* **350**: 295-310 (1997).

65. Preetham and Lieuwen, T. *AIAA Paper* # 2006-0960 (2006).

66. Cho, J. H. and Lieuwen, T., *Combust. Flame* **140**: 116-129 (2005).

67. Lieuwen, T. and Yang, V., *Combustion Instabilities in Gas Turbine Engine*, AIAA, Reston, VA, pp. 345 (2006).

68. Liñán, A., *Acta Astronautica* **1**: 1007-1039 (1974).

69. Bonne, U., *Combust. Flame* **16**: 147-159 (1971).

70. Sibulkin, M., Kulkarni, A. K. and Annamalai, K., *Proc. Combust. Inst.* **18**: 611–617 (1981).

71. Sohrab, S. H., Liñán, A. and Williams, F. A., *Combust. Sci. Technol.* **27**: 143-154 (1982).

72. T'ien, J. S., *Combust. Flame* **65**: 31-34 (1986).

73. Chao, B. H., Law, C. K., T'ien, J. S., *Proc. Combust. Inst.* **23**: 523–531 (1990).

74. Oh, T. K., Lee, J. S. and Chung, S. H., *Int. J. Heat Mass Transfer* **37**: 2893-2900 (1994).

75. Liu, F., Smallwood, G. J., Gulder, O. L. and Ju, Y., *Combust. Flame* **121**: 275-287 (2000).

76. Mills, K. and Matalon, M., *Proc. Combust. Inst.* **27**: 2535–2541 (1998).

77. Kim, J. S. and Williams, F. A., *J. Eng. Math.* **31**: 101-118 (1997).

78. Buckmaster, J., Nachman, A. and Taliaferro, S., *Physcia D* 9: 408-424 (1983).

79. Cheatham, S., Ph.D. thesis, Northwestern University, USA (1997).

80. Lee, S. R. and Kim, J. S., *Combust. Theory Modelling* **4**: 29-46 (2000).

81. Lee, S. R. and Kim, J. S., *Combust. Theory Modelling* **6**: 263-278 (2002).

82. Sohn, C. H., Chung, S. H. and Kim, J. S., *Combust. Flame* **117**: 404-412 (1999).

83. Sohn, C. H., Kim, J. S., Chung, S. H. and Maruta, K., *Combust. Flame* **123**: 95-106 (2000).

84. Christiansen, E. W., Tse, S. D. and Law, C. K., *Combust. Flame* **134**: 263-278 (2003).

85. Miklavčič, M., Moore, A. B. and Wichman, I. S., *Combust. Theory Model.* **9**: 403-416 (2005).

86. Strahle, W. C., *Proc. Combust. Inst.* **10**: 1783-1792 (1965).

87. Saitoh, T. and Otsuka, Y., *Combust. Sci. Technol.* **12**: 135-146 (1976).

88. Im, H. G., Chen, J. H. and Chen, J. Y., *Combust. Flame* **118**: 204-212 (1999).

89. Egolfopoulos, F. N. and Campbell, C. S., *J. Fluid Mech.* **318**: 1-29 (1996).

90. Welle, E. J., Roberts, W. L., Carter, C. D. and Donbar, J. M., *Combust. Flame* **135**: 285-297 (2003).

91. Cuenot, B., Egolfopoulos, F. N. and Poinsot, T., *Combust. Theory Modelling* 4: 77-97 (2000).

92. Im, H. G., Law, C. K., Kim, J. S. and Williams, F. A., *Combust. Flame* **100**: 21-30 (1995).

93. Im, H. G., Bechtold, J. K. and Law, C. K., *Combust. Sci. Technol.* **106**: 345-361 (1995).

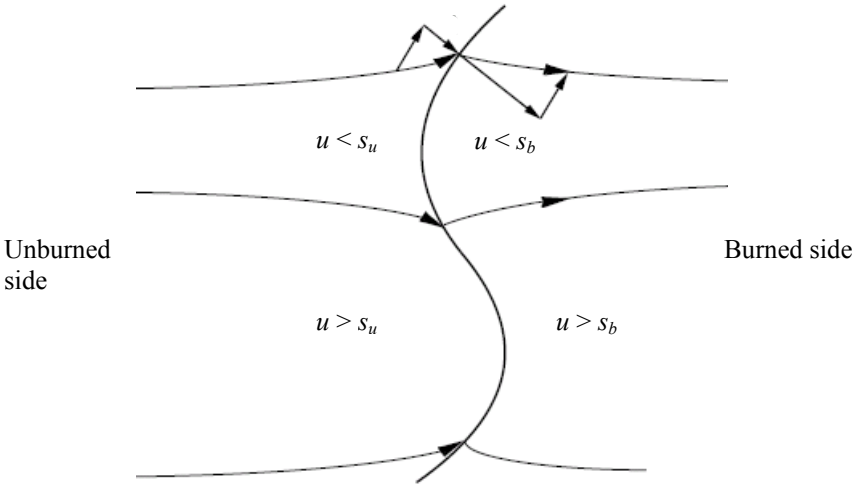

Figure 1.1. Shemataic showing the mechanism of hydrodynamic instabilitiy.

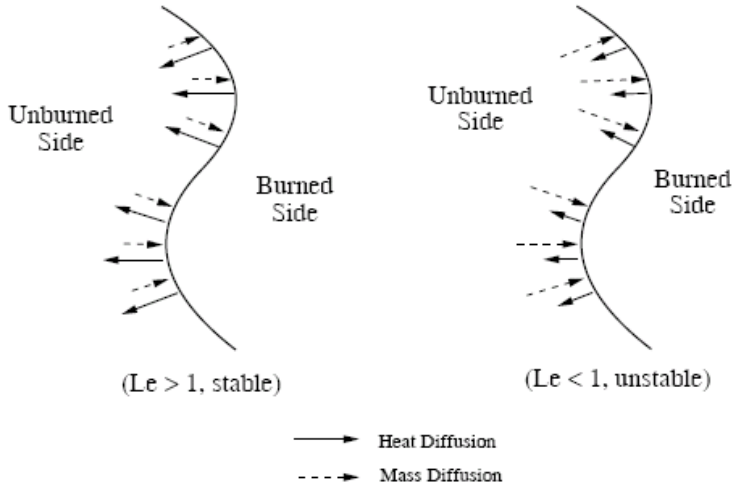

(a) Cellular instability

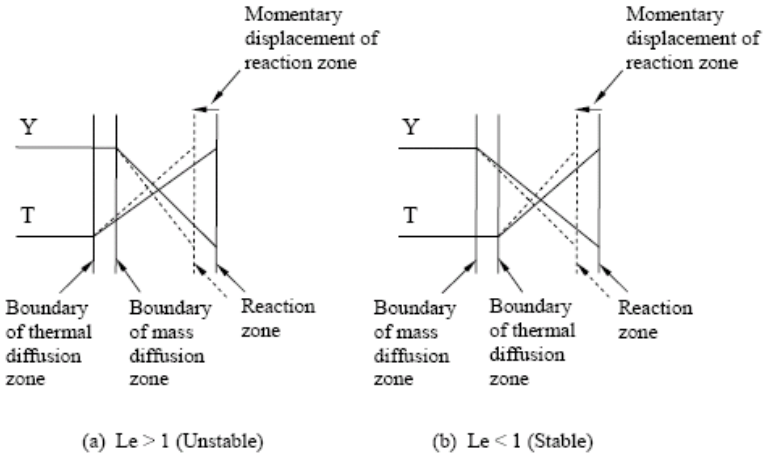

(b) Pulsating instability

Figure 1.2. Shemataic showing the mechanism of thermal-diffusive instabilities. Figures are adapted from Ref. 53.

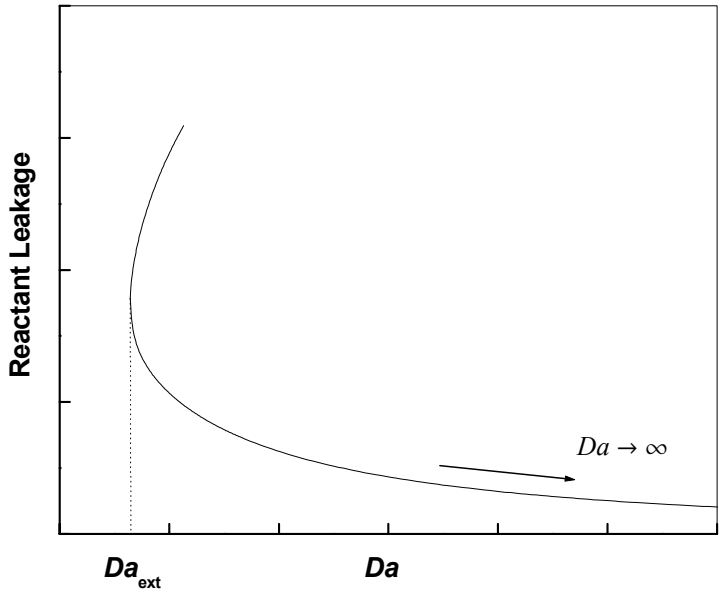

Figure 1.3. Variation of the reactant leakage with the Damköhler number, *Da*.

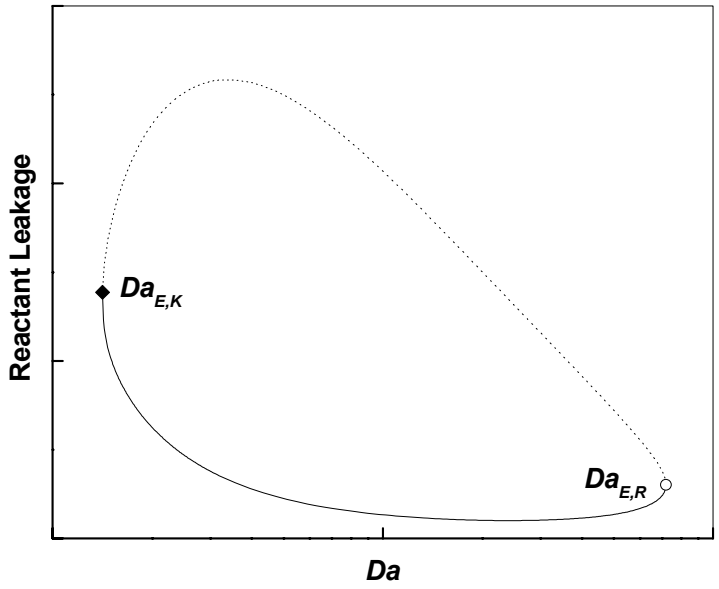

Figure 1.4. Variation of the reactant leakage with the Damköhler number, *Da*, in the presence of radiative heat loss.

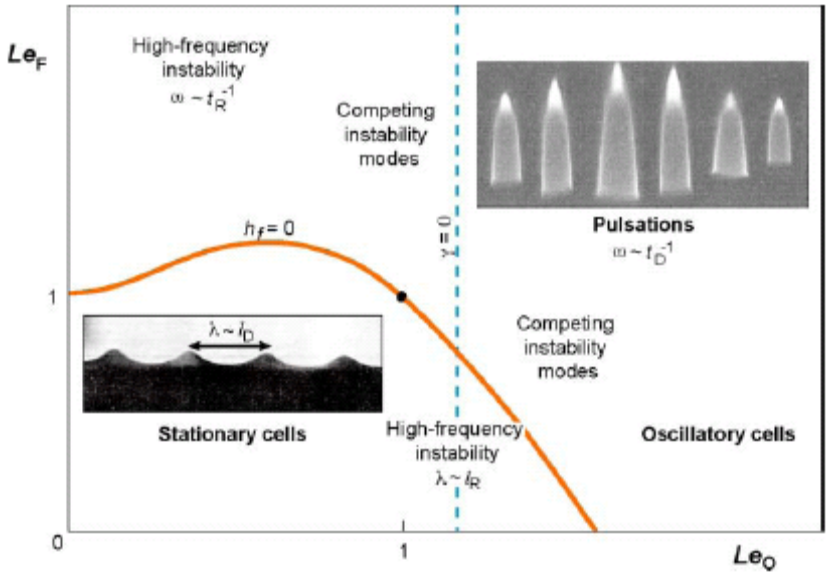

Figure 1.5. Diagram illustrating typical instability modes in the fuel-oxidizer Lewis number parameter plane. This figure is adapted from Ref. 13.

Chapter 2: Nonlinear Oscillations in Diffusion Flames

2.1. Background

In this chapter, we carry out a systematic nonlinear stability analysis for flame oscillations in chambered planar diffusion flames. As reviewed in the previous section, the theoretical description of diffusion flame dynamics is more complicated than that of premixed flames due to the large number of parameters involved. This is even more severe when considering the nonlinear behavior of flame instabilities due to the mathematical difficulties in analyzing the reaction zone structure. Therefore, up to now, only one theoretical work [1] and a few numerical investigations [2-7] have addressed the nonlinear behavior of diffusion flame instabilities. Specifically, Cheatham [1] derived an evolution equation for the perturbation amplitude in a droplet flame by employing a weakly nonlinear theory, and provided a diagram mapping various possible long time behaviors. Three possible modes of flame oscillations were identified: the perturbation may damp; it may become unbounded in finite time; or it may approach a constant amplitude. Lee & Kim [2-3] numerically investigated the nonlinear dynamics of striped diffusion flames formed in the counterflow field, with Lewis numbers sufficiently smaller than unity. Their results show that the 2D stripe flame structure is able to survive Damköhler numbers significantly below the static extinction Damköhler number of 1-D flame structure, due to the enhanced reaction intensity in the reaction segments by the excessive diffusion of reactants from the quenched segments. Hysteresis was also predicted. Sohn *et al.* numerically studied the nonlinear evolution of oscillations triggered

by non-unity Lewis numbers [4] and radiative heat loss [5] in a diffusion flame established in a stagnant mixing layer. The Lewis numbers were assumed sufficiently greater than unity, and their work showed that the flame oscillation was amplified if the initial Damköhler number Da was smaller than the critical Damköhler number, Da_{Cr} On the other hand, when $Da > Da_{Cr}$, the oscillation was damped unless the perturbation of the initial Damköhler number was sufficiently large, in which case a subcritical bifurcation to growing oscillations took place. No limit cycle behavior was predicted in the absence of radiative heat loss. Christiansen *et. al.* [6] simulated the transient behavior of burner-supported spherical diffusion flames using detailed chemistry and transport. Their results show that, when $Da < Da_{Cr}$, the amplitude of oscillations always increased, and eventually led to extinction when the amplitude became too large. No limit cycle behavior was observed.

While the numerical studies discussed above have revealed some interesting phenomena about the nonlinear evolution of flame instabilities, the parameters employed in these studies were very limited. Thus, a nonlinear stability analysis near the bifurcation point (stability limit) will be conducted in this chapter to understand more details of the nonlinear characteristics of flame oscillations over a wider parameter range.

2.2. Formulation

We consider a simple configuration of a planar flame in a chamber [7-8]. As shown in Fig. 2.1, the fuel stream is fed from the bottom of a long channel at a constant velocity, normalized to unity. The oxidizer diffuses against the fuel stream from a fast cross-stream at the top of the chamber. The fast oxidizer stream maintains constant conditions at the

top of the chamber by carrying away the combustion products reaching there. We employ the asymptotic theory of Cheatham & Matalon [7] in which the convective-diffusive equations for temperature and fuel and oxidizer mass fractions are solved on either side of the flame surface, x_f. These quantities are then related across the flame using the matching conditions obtained by asymptotic analysis of the reaction zone. Assuming constant physical and chemical properties of reactants, constant density, and one-step irreversible chemical reaction, the appropriate nondimensional governing equations can be written as [7]

$$\frac{\partial T}{\partial t} + \frac{\partial T}{\partial x} - \frac{\partial^2 T}{\partial x^2} = 0, \tag{2.1}$$

$$\frac{\partial Y_F}{\partial t} + \frac{\partial Y_F}{\partial x} - Le_F^{-1}\frac{\partial^2 Y_F}{\partial x^2} = 0, \tag{2.2}$$

$$\frac{\partial Y_O}{\partial t} + \frac{\partial Y_O}{\partial x} - Le_O^{-1}\frac{\partial^2 Y_O}{\partial x^2} = 0, \tag{2.3}$$

where T is the temperature and Y_F and Y_O are the mass fractions of the fuel and oxidizer, respectively. The Lewis numbers of the fuel and oxidizer, Le_F and Le_O, are assumed larger than unity in order to focus on the pulsating instability.

The boundary conditions are

$$T = T_{-\infty} \qquad Y_F = 1 \qquad Y_O = 0 \qquad \text{as } x \to -\infty \tag{2.4}$$

$$T = T_{-\infty} + \Delta T \qquad Y_F = 0 \qquad Y_O = \phi^{-1} \qquad \text{at } x = 0 \tag{2.5}$$

where $\Delta T = T_\infty - T_{-\infty}$ is the difference between the temperatures at the oxidizer and fuel boundaries, and ϕ is the initial mixture strength, defined as the ratio of the fuel mass fraction at the fuel boundary to the oxidizer mass fraction at the oxidizer boundary normalized by the mass-weighted stoichiometric coefficient ratio, i.e.

$$\phi = \frac{\widetilde{Y}_{F,-\infty} / \nu_F W_F}{\widetilde{Y}_{O,\infty} / \nu_O W_O}$$

where ν_i and W_i respectively denote the stoichiometric coefficient and molecular weight of species i ($i = F, O$), and the over-tilde "~" designates the unscaled Y_i for differentiation with their nondimensional counterparts.

The derived jump relations at the reaction sheet location x_f are [7]

$$[T] = [Y_F] = [Y_O] = 0 \tag{2.6}$$

$$\left[\frac{\partial T}{\partial x}\right] = -\frac{1}{Le_F}\left[\frac{\partial Y_F}{\partial x}\right] = -\frac{1}{Le_O}\left[\frac{\partial Y_O}{\partial x}\right] \tag{2.7}$$

where we have adopted the notation $[T] = T(x_f^+) - T(x_f^-)$. Expressions for the amount of leakage of the reactants through the reaction sheet have been given as [7]

$$Y_F\big|_{x=x_f^+} = \beta^{-1} Le_F S_F \tag{2.8}$$

$$Y_O\big|_{x=x_f^-} = \beta^{-1} Le_O S_O \tag{2.9}$$

where β is the Zeldovich number and approximate formulas for the quantities S_F and S_O have been determined through curve fitting [7]. The specific form of these formulas relevant to the present investigation will be presented shortly. These quantities depend only on two parameters γ and Δ. Here,

$$\gamma = -\frac{\left.\dfrac{\partial T}{\partial x}\right|_{x_f^-} + \left.\dfrac{\partial T}{\partial x}\right|_{x_f^+}}{\left.\dfrac{\partial T}{\partial x}\right|_{x_f^-} - \left.\dfrac{\partial T}{\partial x}\right|_{x_f^+}} \tag{2.10}$$

represents the excess of heat conducted away to one side of the reaction sheet from the total heat generated by the chemical reaction, and

$$\Delta = 4Le_F Le_O Da\left[\frac{\partial T}{\partial x}\right]^{-2} \exp\left(\frac{1+\gamma}{2}h_O + \frac{1-\gamma}{2}h_O\right) \tag{2.11}$$

is the reduced Damköhler number which measures the intensity of chemical reaction, where

$$h_F = T_1^+ + \frac{1}{Le_F}(Y_F)_1^+$$

$$h_O = T_1^- + \frac{1}{Le_O}(Y_O)_1^-$$

are the excess/deficiency in the fuel and oxidizer enthalpies, respectively, evaluated at the reaction sheet. Furthermore, the subscript "1" denotes the $O(\beta^{-1})$ expression in a power series expansion in terms of β^{-1}, and the superscript +/- denotes quantities on the oxidizer/fuel side of the reaction sheet. The term $(1+\gamma)h_O/2+(1-\gamma)h_F/2$ in Eq. (2.11) represents the excess/deficiency in the total enthalpy in the reaction region, as mentioned in Chapter 1. It comes from the imbalance of diffusion for chemical and thermal energies as the reactants leak through the reaction zone. We note that, if the Lewis numbers are unity, the enthalpy variables are conserved scalars and hence h_F and h_O are both zero. The heat transfer parameter, γ, measures the degree of asymmetry of thermal diffusion across the reaction zone. If γ = 0, the temperature profile is symmetric and hence heat is conducted to the fuel and oxidant sides equally. As $\gamma > 0$, more heat is conducted to the oxidant side and consequently the oxidant is more completely consumed, so that the reaction is relatively "fuel-rich". Similarly, it is "fuel-lean" as $\gamma < 0$.

Figure 2.2 shows S_F and S_O as a function of Δ. Solutions are seen to exist only when $\Delta \geq \Delta_c$ and for each $\Delta > \Delta_c$ there exist two distinct solutions characterized by

different extent of reactant leakage (and flame temperature). The critical value Δ_c depends only on $|\gamma|$ and was first determined by Liñán [9] as

$$\Delta_c = e^{\left\{(1-|\gamma|)-(1-|\gamma|)^2+0.26(1-|\gamma|)^3+0.055(1-|\gamma|)^4\right\}}$$

Approximate formulas for the leakage function S_1 and S_2 in Fig. 2.2 were given in [7]. These formulas differ depending on whether we are discussing the top or bottom branch, and are given by

$$S_1 = \begin{cases} a_0\Delta^{-4/3}\exp\left\{-a_1(\Delta-\Delta_c)^{a_2}\right\} \\ \Delta^{-1/3}\left\{q_0+q_1(\Delta-\Delta_c)^{q_2}\right\} \end{cases}$$

$$S_2 = \begin{cases} b_0\Delta^{-4/3}\exp\left\{-b_1(\Delta-\Delta_c)^{b_2}\right\} \\ \Delta^{-1/3}\left\{r_0+r_1(\Delta-\Delta_c)^{r_2}\right\} \end{cases}$$

where the top line in the bracketed expressions corresponds to the solution of the lower branch in Fig. 2.2 and the bottom line to the upper branch. The coefficients a_i, b_i, q_i and r_i depend only on γ and are given in the appendix of [8]. For $\gamma > 0$, S_1 and S_2 correspond to S_F and S_O and for $\gamma < 0$ to S_O and S_F, respectively. For definiteness, we shall restrict our discussion to the case $\gamma > 0$ and thus only the expressions corresponding to the lower branch of Fig. 2.2 are needed. The appropriate coefficients are

$$\begin{aligned} a_0 &= 0.61923 + 3.2523|\gamma| + 0.52069\gamma^2 \\ a_1 &= 1.9077 - 1.901|\gamma| + 1.055\gamma^2 \\ a_2 &= 0.46137 - 0.15374|\gamma| - 0.06769\gamma^4 - 0.23288\gamma^6 \end{aligned}$$

and

$$\begin{aligned} b_0 &= 0.61923(1-|\gamma|)^{15}\exp\{10.469|\gamma|\} \\ b_1 &= 1.9077 + 11.588\gamma^2 - 17.014\gamma^4 + 55.865\gamma^6 \\ b_2 &= 0.46137 + 0.27706|\gamma| - 0.2029\gamma^2 \end{aligned}$$

2.3. The Basic State and Linear Stability Analysis

The above system possesses the following steady-state solutions:

$$T=\begin{cases} T_{-\infty}+(e^{-\xi_f}+\Delta T-1)e^{x}+\dfrac{1}{\beta}\left\{\dfrac{Le_F}{Le_O}\dfrac{(1-e^{Le_O\xi_f})-Le_O(1-e^{\xi_f})}{1-e^{Le_F\xi_f}}-\dfrac{S_O}{S_F}\right\}S_F e^{x-\xi_f}, & x<x_f \\ T_{-\infty}+1+(\Delta T-1)e^{x}-\dfrac{1}{\beta}\left\{\dfrac{1-e^{x}}{1-e^{Le_F\xi_f}}\right\}Le_F S_F, & x>x_f \end{cases}$$

$$Y_F=\begin{cases} 1-e^{Le_F(x-\xi_f)}+\dfrac{1}{\beta}\left\{1-\dfrac{Le_F}{Le_O}\dfrac{1-e^{Le_O\xi_f}}{1-e^{Le_F\xi_f}}+\dfrac{S_O}{S_F}\right\}Le_F S_F e^{Le_F(x-\xi_f)}, & x<x_f \\ \dfrac{1}{\beta}\left\{\dfrac{1-e^{Le_F x}}{1-e^{Le_F\xi_f}}\right\}Le_F S_F, & x>x_f \end{cases} \tag{2.12}$$

$$Y_O=\begin{cases} \dfrac{1}{\beta}Le_O S_O e^{Le_O(x-\xi_f)}, & x<x_f \\ (1+\phi^{-1})e^{Le_O x}-1+\dfrac{1}{\beta}\left\{\dfrac{1-e^{Le_O x}}{1-e^{Le_F\xi_f}}\right\}Le_F S_F, & x>x_f \end{cases}$$

where the reaction-sheet location x_f is given by

$$x_f=\xi_f+\frac{1}{\beta}\left(S_O-\frac{Le_F}{Le_O}\frac{1-e^{Le_O\xi_f}}{1-e^{Le_F\xi_f}}S_F\right)$$

and the location of the stoichiometric flame surface ξ_f corresponding to the reaction-sheet limit is given by

$$\xi_f=-Le_O^{-1}\ln(1+\phi^{-1}) \tag{2.13}$$

Note that, in constructing these solutions, it is necessary to include the terms of $O(\beta^{-1})$ since the complete determination of the overall flame response requires that the excess/deficient enthalpies to be known. The steady-state solutions (2.12) give the flame temperature

$$T_f = T_{\text{ad}} - \frac{1}{\beta}\left\{\frac{1-e^{\xi_f}}{1-e^{Le_F\xi_f}}Le_F S_F - \left(S_O - \frac{Le_F}{Le_O}\frac{1-e^{Le_O\xi_f}}{1-e^{Le_F\xi_f}}S_F\right)(\Delta T - 1)e^{\xi_f}\right\}$$

where the adiabatic flame temperature is

$$T_{\text{ad}} = 1 + T_{-\infty} + (\Delta T - 1)e^{\xi_f}$$

The quantities γ, h_F and h_O can now be determined from the above solutions as

$$\gamma = -1 + 2(1-\Delta T)\left(\frac{\phi}{1+\phi}\right)^{1/Le_O} \tag{2.14}$$

$$h_F = -\left\{\frac{Le_F\left(1-e^{\xi_f}\right)-\left(1-e^{Le_F\xi_f}\right)}{1-e^{Le_F\xi_f}}\right\}S_F(\gamma,\Delta)$$

$$h_O = -\frac{Le_F}{Le_O}\left\{\frac{Le_O\left(1-e^{\xi_f}\right)-\left(1-e^{Le_O\xi_f}\right)}{1-e^{Le_F\xi_f}}\right\}S_F(\gamma,\Delta)$$

Finally, the relationship between Δ and Da is found to be

$$\Delta = 4Le_F Le_O Da \exp\left[\left(\frac{1-\gamma}{2} - Le_F\frac{1-e^{\xi_f}}{1-e^{Le_F\xi_f}} + \frac{1+\gamma}{2}\frac{Le_F}{Le_O}\frac{1-e^{Le_O\xi_f}}{1-e^{Le_F\xi_f}}\right)S_F(\gamma,\Delta)\right] \tag{2.15}$$

It is clear that, when $Le_F = Le_O = 1$, the excess/deficiency enthalpies are zero, and Eq. (2.15) reduces to $\Delta = 4Da$. For general Lewis numbers, however, the excess/deficiency enthalpy results in an implicit relation between Δ and Da. As a consequence, the turning point for Δ in Fig. 2.2 does not correspond to the turning point for Da, indicating that Δ_c does not correspond to the physical extinction point. This feature was discussed in detail by Kim & Williams [10].

The linear stability of the above solutions has been investigated by Kukuck & Matalon [8], who identified critical conditions for the onset of pulsating instability. The instability was found to arise at a value of Damköhler number exceeding its quasi-steady

extinction value. This is illustrated in Fig. 2.3 where we show a typical response curve in the $T_f \sim Da$ plane. The subscripts 'ext' and 'Cr' denote the points corresponding to the quasi-steady extinction and the onset of instability, respectively. The point denoted by Da_c in Fig. 2.3 represents the point at which the parameter Δ has a turning point, i.e. $\Delta = \Delta_c$ in Fig. 2.4. As remarked earlier, the physical turning point of Da may differ significantly from Da_c for non-unity Lewis numbers. Figure 2.3 also shows that the onset of instability occurs at the Damköhler number Da_{Cr} prior to but near extinction, and in general $Da_{\mathrm{Cr}} - Da_{\mathrm{ext}} \sim O(1)$ [8]. The planar flame with Damköhler number Da greater than Da_{Cr} on the upper branch of the $T_f \sim Da$ response curve is stable. Thus, between the two possible solutions for a given $Da > Da_{\mathrm{Cr}}$, the stable solution is the one corresponding to the larger flame temperature and smaller reactant leakage. The imaginary part of the growth rate is non-zero at the threshold, and therefore pulsating instability develops when $Da_{\mathrm{ext}} < Da < Da_{\mathrm{Cr}}$.

We shall now summarize several other results from the linear analysis [8] that will help guide our choice of parameters to exploit in the nonlinear analysis. The range of instability $(Da_{\mathrm{Cr}} - Da_{\mathrm{ext}})/Da_{\mathrm{ext}}$ depends on the four prescribed parameters: Le_F, Le_O, ϕ and ΔT. Among them the initial mixture strength ϕ has the most pronounced effect. The range of instability $(Da_{\mathrm{Cr}} - Da_{\mathrm{ext}})/Da_{\mathrm{ext}}$ increases dramatically with ϕ indicating that "fuel-rich" flames are more susceptible to pulsating instability. The effect of the Lewis number of oxidizer Le_O on $(Da_{\mathrm{Cr}} - Da_{\mathrm{ext}})/Da_{\mathrm{ext}}$ is moderate compared to ϕ but the general trend is that $(Da_{\mathrm{Cr}} - Da_{\mathrm{ext}})/Da_{\mathrm{ext}}$ increases with Le_O. For a given Le_O, the instability is only possible for a range of the fuel Lewis number Le_F. The results [8] also

show that instability occurs when the oxidizer, acting as the reactant diffusing against the convection, is the more completely consumed reactant, such that the reaction zone burns "fuel-rich". Thus, for example, the instability can be triggered by heating the fuel, i.e. decreasing ΔT.

2.4. Derivation of Evolution Equation

A weakly nonlinear analysis is now carried out to derive an evolution equation for the amplitude of a perturbation. The Damköhler number Da is chosen to be very close to the critical Damköhler number Da_{Cr} corresponding to the marginally stable state. Thus we introduce the small bifurcation parameter, ε, as

$$s'\varepsilon^2 = \frac{Da - Da_{\mathrm{Cr}}}{Da_{\mathrm{Cr}}}$$

where $s' = 1$ for $Da > Da_{\mathrm{Cr}}$ and $s' = -1$ for $Da < Da_{\mathrm{Cr}}$. We also retain the "fast time" t, associated with the oscillation of flames, and introduce a "slow time" τ, associated with the long time transient behavior. Furthermore, since planar perturbation corresponds to the fastest growing mode of instability, we introduce small 1D perturbations, with amplitude $\varepsilon << 1$, superimposed onto the steady state solutions identified below by the subscript "b":

$$T = T_b(x) + \beta^{-1}\varepsilon u(x,t,\tau) \tag{2.16}$$

$$Y_F = Y_{F,b}(x) + \beta^{-1}\varepsilon v(x,t,\tau) \tag{2.17}$$

$$Y_O = Y_{O,b}(x) + \beta^{-1}\varepsilon w(x,t,\tau) \tag{2.18}$$

$$x_f = x_{f,b} + \beta^{-1}\varepsilon l(x,t,\tau) \tag{2.19}$$

where u, v, w and l are the perturbation functions of temperature, fuel mass fraction, oxidizer mass fraction and flame sheet location, respectively. The slow time variable τ is defined as $\tau = \omega t$, where $\omega(\varepsilon)$ is a small frequency parameter.

Substituting Eqs. (2.16)-(2.19) into Eqs. (2.1)-(2.3) yields the governing equations for perturbations in the convective-diffusive zone

$$u_t + u_x - u_{xx} + \omega u_\tau = 0 \tag{2.20}$$

$$v_t + v_x - Le_F^{-1} v_{xx} + \omega v_\tau = 0 \tag{2.21}$$

$$w_t + w_x - Le_O^{-1} w_{xx} + \omega w_\tau = 0 \tag{2.22}$$

The above Eqs. (2.16)-(2.19) are also inserted into the boundary and jump conditions (2.4)-(2.7) which, when expanded for small ε, take the form

$$u = v = w = 0 \qquad \text{at } x = 0 \text{ and as } x \to -\infty \tag{2.23}$$

and

$$[u] = -Le_F^{-1}[v] = -Le_O^{-1}[w] \tag{2.24}$$

$$\left[u - \frac{\partial u}{\partial x}\right] = -\left[v - Le_F^{-1}\frac{\partial v}{\partial x}\right] = -\left[w - Le_O^{-1}\frac{\partial w}{\partial x}\right] \tag{2.25}$$

respectively. We note that the only nonlinearity in the model arises in the leakage conditions (2.8) and (2.9), which when expanded around the steady state, have the form:

$$\varepsilon Le_F^{-1} v^+ = \sum_{k=1}^{\infty} \frac{1}{k!} \frac{\partial^k S_F(\gamma, \Delta_b)}{\partial \Delta_b^k} (\Delta - \Delta_b)^k \tag{2.26}$$

$$\varepsilon Le_O^{-1} w^- = \sum_{k=1}^{\infty} \frac{1}{k!} \frac{\partial^k S_O(\gamma, \Delta_b)}{\partial \Delta_b^k} (\Delta - \Delta_b)^k \tag{2.27}$$

where Δ_b is the reduced Damköhler number evaluated at the steady state condition.

We expand the variables u, v, w and ω in a power series in ε, $(u,v,w)=\sum_{m=0}^{\infty}(u_m,v_m,w_m)\varepsilon^m$ and $\omega=\sum_{m=1}^{\infty}\omega_m\varepsilon^m$, respectively, and expand the governing equations, boundary, jump and leakage conditions for perturbations (2.20)-(2.27) in terms of ε. We obtain a system of equations to be solved at each order:

$$L\begin{pmatrix}u_m\\v_m\\w_m\end{pmatrix}=\begin{pmatrix}\dfrac{\partial^2 u_m}{\partial x^2}-\dfrac{\partial u_m}{\partial x}-\dfrac{\partial u_m}{\partial t}\\ \dfrac{\partial^2 v_m}{\partial x^2}-Le_F\dfrac{\partial v_m}{\partial x}-Le_F\dfrac{\partial v_m}{\partial t}\\ \dfrac{\partial^2 w_m}{\partial x^2}-Le_O\dfrac{\partial w_m}{\partial x}-Le_O\dfrac{\partial w_m}{\partial t}\end{pmatrix}=\begin{pmatrix}p_m\\q_m\\r_m\end{pmatrix} \tag{2.28}$$

with boundary conditions

$$u_m=v_m=w_m=0 \qquad \text{at } x=0 \text{ and as } x\to-\infty \tag{2.29}$$

jump conditions

$$[u_m]=-Le_F^{-1}[v_m]=-Le_O^{-1}[w_m] \tag{2.30}$$

$$\left[u_m-\frac{\partial u_m}{\partial x}\right]=-\left[v_m-Le_F^{-1}\frac{\partial v_m}{\partial x}\right]=-\left[w_m-Le_O^{-1}\frac{\partial w_m}{\partial x}\right] \tag{2.31}$$

and leakage conditions

$$\left(\frac{1-\gamma}{2}Le_Fb_F\right)u_m^+ +\left(\frac{1+\gamma}{2}Le_Fb_F\right)u_m^- +\left(\frac{1-\gamma}{2}b_F-1\right)v_m^+ +\left(\frac{1+\gamma}{2}\frac{Le_Fb_F}{Le_O}\right)w_m^-=\alpha_{Fm} \tag{2.32}$$

$$\left(\frac{1-\gamma}{2}Le_Ob_O\right)u_m^+ +\left(\frac{1+\gamma}{2}Le_Ob_O\right)u_m^- +\left(\frac{1-\gamma}{2}\frac{Le_Ob_O}{Le_F}\right)v_m^+ +\left(\frac{1+\gamma}{2}b_O-1\right)w_m^-=\alpha_{Om} \tag{2.33}$$

where $m = 0, 1, 2,\ldots$ and

$$b_j=\Delta_{b,\mathrm{Cr}}\frac{\partial S_j(\gamma,\Delta_{b,\mathrm{Cr}})}{\partial\Delta_b},\quad j=F,O$$

where $\Delta_{b,\mathrm{Cr}}$ corresponds to the value at the marginally stable state. The form of the inhomogeneous terms α_{Fm} and α_{Om} will be presented shortly. At leading order $m=0$, $p_0 = q_0 = r_0 = \alpha_{F0} = \alpha_{O0} = 0$, and we recover the homogeneous linear problem, such that the solutions are given as

$$(u_0, v_0, w_0) = \begin{cases} A(\tau)\Phi_J^-(x)\exp(ic_0 t) + c.c., & x < x_f \\ A(\tau)\Phi_J^+(x)\exp(ic_0 t) + c.c., & x > x_f \end{cases} \tag{2.34}$$

Here *c.c.* means the complex conjugate, c_0 is the frequency of oscillation at the onset of instability, and

$$\Phi_J^-(x) = C_J^- \exp\left[\left(Le_J/2 + \lambda_J\right)x\right]$$

$$\Phi_J^+(x) = C_J^+ \left\{\exp\left[\left(Le_J/2 + \lambda_J\right)x\right] - \exp\left[\left(Le_J/2 - \lambda_J\right)x\right]\right\}$$

where $J = T, F, O$ corresponds to the solutions of u_0, v_0 and w_0, respectively, and we have employed the notation

$$\lambda_J = \frac{1}{2}\sqrt{Le_J^2 + 4iLe_J c_0}$$

with $Le_T = 1$. The constants $C_J^{\pm}$ are determined by the linear system (2.A1) given in the appendix, established from the jump & leakage conditions for the leading order perturbations. The amplitude function $A(\tau)$, which is a function of slow time τ, is determined by going to higher orders in our perturbation scheme. At each order, solutions exist only if appropriate solvability conditions are satisfied, and thus we introduce the adjoint system:

$$L^*\begin{pmatrix} u^* \\ v^* \\ w^* \end{pmatrix} = \begin{pmatrix} \dfrac{\partial^2 u^*}{\partial x^2} + \dfrac{\partial u^*}{\partial x} + \dfrac{\partial u^*}{\partial t} \\ \dfrac{\partial^2 v^*}{\partial x^2} + Le_F \dfrac{\partial v^*}{\partial x} + Le_F \dfrac{\partial v^*}{\partial t} \\ \dfrac{\partial^2 w^*}{\partial x^2} + Le_O \dfrac{\partial w^*}{\partial x} + Le_O \dfrac{\partial w^*}{\partial t} \end{pmatrix} = 0 \tag{2.35}$$

with boundary conditions

$$u^* = v^* = w^* = 0 \quad \text{at } x = 0$$

$$u^*, v^*, w^* \text{ bounded} \quad \text{as } x \to -\infty$$

and jump and leakage conditions

$$[u^*] = [v^*] = [w^*] = 0$$

$$(u^*)^- - Le_F (v^*)^- - Le_O (w^*)^- = 0$$

$$\left[\frac{\partial u^*}{\partial x}\right] + \frac{1}{\chi}\frac{Le_F b_F}{Le_O b_O}\left[\frac{\partial v^*}{\partial x}\right] + \frac{1}{\chi}\left[\frac{\partial w^*}{\partial x}\right] = 0$$

$$\left(\frac{\partial u^*}{\partial x}\right)^+ + \frac{1-\gamma}{1+\gamma}\left(\frac{\partial u^*}{\partial x}\right)^- - \frac{2Le_F}{1+\gamma}\left(\frac{\partial v^*}{\partial x}\right)^- - \frac{2Le_O}{1+\gamma}\left(\frac{\partial w^*}{\partial x}\right)^+ = 0$$

where

$$\chi = -\left\{\left(\frac{1-\gamma}{2} b_F - 1\right)\frac{1}{Le_O b_O} + \frac{1+\gamma}{2}\frac{1}{Le_O}\right\}$$

The solutions to the adjoint problem (2.35) are

$$(u^*, v^*, w^*) = \begin{cases} \Psi_J^-(x)\exp(ic_0 t) + c.c., & x < x_f \\ \Psi_J^+(x)\exp(ic_0 t) + c.c., & x > x_f \end{cases} \tag{2.36}$$

where $J = T, F, O$

$$\Psi_J^-(x) = E_J^- \exp\left[\left(-Le_J/2 + \bar{\lambda}_J\right)x\right]$$

$$\Psi_J^+(x) = E_J^+ \left\{ \exp\left[\left(-Le_J/2 + \bar{\lambda}_J \right) x \right] - \exp\left[\left(-Le_J/2 - \bar{\lambda}_J \right) x \right] \right\}$$

Here $\bar{\lambda}_J$ is the complex conjugate of λ_J and the constants $E_J^{\pm}$ are determined by the linear system (2.A2) given in the appendix.

At $O(\varepsilon)$,

$$\alpha_{j1} = \frac{1}{2} b_{j1} \left[F^2(\Phi) A^2 \exp(2ic_0 t) + c.c. + 2\left|F(\Phi)\right|^2 \left|A\right|^2 \right]$$

where $j = F, O$,

$$b_{j1} = -Le_j \left\{ \Delta_{b,\mathrm{Cr}} \frac{\partial S_j(\gamma, \Delta_{b,\mathrm{Cr}})}{\partial \Delta_b} + \Delta_{b,\mathrm{Cr}}^2 \frac{\partial^2 S_j(\gamma, \Delta_{b,\mathrm{Cr}})}{\partial \Delta_b^2} \right\},$$

and the function $F(\Phi)$ is defined as

$$F(\Phi) = \frac{1+\gamma}{2} \left\{ \Phi_T^-(\xi_f) + Le_O^{-1} \Phi_O^-(\xi_f) \right\} + \frac{1-\gamma}{2} \left\{ \Phi_T^+(\xi_f) + Le_F^{-1} \Phi_F^+(\xi_f) \right\}$$

The solutions to the $O(\varepsilon)$ perturbations are given as

$$(u_1, v_1, w_1) = \begin{cases} A^2 \Theta_J^-(x) \exp(2ic_0 t) + c.c. + \left|A\right|^2 \Omega_J^-(x), & x < x_f \\ A^2 \Theta_J^+(x) \exp(2ic_0 t) + c.c. + \left|A\right|^2 \Omega_J^+(x), & x > x_f \end{cases} \tag{2.37}$$

where $J = T, F, O$,

$$\Theta_J^-(x) = D_J^- \exp\left[\left(Le_J/2 + \mu_J \right) x \right]$$

$$\Theta_J^+(x) = D_J^+ \left\{ \exp\left[\left(Le_J/2 + \mu_J \right) x \right] - \exp\left[\left(Le_J/2 - \mu_J \right) x \right] \right\}$$

$$\Omega_J^-(x) = B_J^- e^{Le_J x}$$

$$\Omega_J^+(x) = B_J^+ \left(1 - e^{Le_J x} \right)$$

$$\mu_J = \frac{1}{2} \sqrt{Le_J^2 + 8iLe_J c_0},$$

and the constants $B_J^{\pm}$ and $D_J^{\pm}$ are determined by the linear system (2.A3) and (2.A4), respectively, given in the appendix. The solvability condition at $O(\varepsilon)$ produces $\omega_1 = 0$.

At $O(\varepsilon^2)$,

$$\alpha_{j2} = \alpha_{j2,3} A^3 \exp(3ic_0 t) + \left(\alpha_{j2,2} A|A|^2 + \alpha_{j2,1} A\right)\exp(ic_0 t) + c.c.$$

where $j = F, O$,

$$\alpha_{j2,1} = s b_{j1} F(\Phi)$$

$$\alpha_{j2,2} = b_{j1}\left(F(\Phi)F(\Omega) + \overline{F}(\Phi)F(\Theta)\right) + b_{j2}F(\Phi)|F(\Phi)|^2$$

$$\alpha_{j2,3} = b_{j1}F(\Phi)F(\Theta) + \frac{1}{3}b_{j2}F^3(\Phi)$$

$$b_{j2} = -Le_j\left\{\frac{\Delta_{b,\mathrm{Cr}}}{2}\frac{\partial S_j(\gamma,\Delta_{b,\mathrm{Cr}})}{\partial\Delta_b} + \frac{3\Delta_{b,\mathrm{Cr}}^2}{2}\frac{\partial^2 S_j(\gamma,\Delta_{b,\mathrm{Cr}})}{\partial\Delta_b^2} + \frac{\Delta_{b,\mathrm{Cr}}^3}{2}\frac{\partial^3 S_j(\gamma,\Delta_{b,\mathrm{Cr}})}{\partial\Delta_b^3}\right\}$$

$$s = \frac{s'}{1 - \left(\frac{1-\gamma}{2} - Le_F\frac{1-e^{\xi_f}}{1-e^{Le_F\xi_f}} + \frac{1+\gamma}{2}\frac{Le_F}{Le_O}\frac{1-e^{Le_O\xi_f}}{1-e^{Le_F\xi_f}}\right)b_F}$$

Applying the solvability condition at this order provides the following evolution equation for the amplitude of the perturbation

$$\frac{dA}{d\tau_2} + \alpha_1 A + \alpha_2 A|A|^2 = 0, \tag{2.38}$$

where the new slow time $\tau_2 = \varepsilon^2 t$ and the coefficients are given by

$$\alpha_1 = \frac{\alpha_{10}}{\alpha_0}, \qquad \alpha_2 = \frac{\alpha_{20}}{\alpha_0}$$

$$\alpha_0 = \int_{-\infty}^{\xi_f^-}\left[\overline{\Psi}_T^-\Phi_T^- + Le_F\overline{\Psi}_F^-\Phi_F^- + Le_O\overline{\Psi}_O^-\Phi_O^-\right]dx + \int_{\xi_f^+}^{0}\left[\overline{\Psi}_T^+\Phi_T^+ + Le_F\overline{\Psi}_F^+\Phi_F^+ + Le_O\overline{\Psi}_O^+\Phi_O^+\right]dx$$

$$\alpha_{10} = \left\{\left(\frac{1-\gamma}{2\chi}\frac{b_F}{Le_O b_O}+1\right)\left[\frac{d\overline{\Psi}_F}{dx}\right]+\left(\frac{1-\gamma}{2\chi}\frac{1}{Le_F}\right)\left[\frac{d\overline{\Psi}_O}{dx}\right]\right\}\alpha_{F2,1} +$$
$$\left\{\left(\frac{1+\gamma}{2\chi}\frac{Le_F b_F}{Le_O^2 b_O}\right)\left[\frac{d\overline{\Psi}_F}{dx}\right]-\frac{1}{\chi}\left(\frac{1-\gamma}{2}b_F-1\right)\frac{1}{Le_O b_O}\left[\frac{d\overline{\Psi}_O}{dx}\right]\right\}\alpha_{O2,1}$$

$$\alpha_{20} = \left\{\left(\frac{1-\gamma}{2\chi}\frac{b_F}{Le_O b_O}+1\right)\left[\frac{d\overline{\Psi}_F}{dx}\right]+\left(\frac{1-\gamma}{2\chi}\frac{1}{Le_F}\right)\left[\frac{d\overline{\Psi}_O}{dx}\right]\right\}\alpha_{F2,2} +$$
$$\left\{\left(\frac{1+\gamma}{2\chi}\frac{Le_F b_F}{Le_O^2 b_O}\right)\left[\frac{d\overline{\Psi}_F}{dx}\right]-\frac{1}{\chi}\left(\frac{1-\gamma}{2}b_F-1\right)\frac{1}{Le_O b_O}\left[\frac{d\overline{\Psi}_O}{dx}\right]\right\}\alpha_{O2,2}$$

Here we have adopted the notation $\left[\frac{d\overline{\Psi}_j}{dx}\right] = \frac{d\overline{\Psi}_j^{+}(\xi_f)}{dx} - \frac{d\overline{\Psi}_j^{-}(\xi_f)}{dx}$, $j = F, O$.

The above evolution equation is a classical equation of the Landau type. We construct solutions by first writing the perturbation amplitude A in polar form and separating α_1 and α_2 into their real and imaginary parts:

$$A = R(\tau_2)\exp[i\theta(\tau_2)]$$

$$\alpha_1 = \alpha_{1r} + i\alpha_{1i}, \qquad \alpha_2 = \alpha_{2r} + i\alpha_{2i}$$

The complex amplitude Eq. (2.38) can now be expressed as two real equations:

$$R' + \alpha_{1r}R + \alpha_{2r}R^3 = 0 \tag{2.39}$$

$$R\theta' + \alpha_{1i}R + \alpha_{2i}R^3 = 0 \tag{2.40}$$

where the prime denotes differentiation with respect to τ_2. The solutions to Eqs. (2.39) and (2.40) are

$$R(\tau_2) = \frac{R(0)}{\sqrt{[1+\alpha_{2r}R^2(0)/\alpha_{1r}]\exp(2\alpha_{1r}\tau_2) - \alpha_{2r}R^2(0)/\alpha_{1r}}} \tag{2.41}$$

$$\theta(\tau_2) = -\frac{\alpha_{2i}}{2\alpha_{2r}} \ln\left\{[1+\alpha_{2r}R^2(0)/\alpha_{1r}]\exp(2\alpha_{1r}\tau_2) - \alpha_{2r}R^2(0)/\alpha_{1r}\right\}$$
$$+\left(\frac{\alpha_{1r}\alpha_{2i}}{\alpha_{2r}} - \alpha_{1i}\right)\tau_2 + \theta(0)$$

respectively, where $R(0)$ and $\theta(0)$ are the initial magnitude and polar angle, respectively. Equation (2.41) indicates that the long time behavior of the amplitude $R(\tau_2)$ depends only on the coefficients α_{1r} and α_{2r} and the initial condition $R(0)$. When $\alpha_{1r}>0$ and $\alpha_{2r}>0$, Eq. (2.41) indicates $R(\tau_2)\to 0$ as $\tau_2 \to \infty$. Hence this case corresponds to a stable basic state solution. When $\alpha_{1r}>0$ and $\alpha_{2r}<0$, the long time behavior of the amplitude $R(\tau_2)$ depends on its initial condition $R(0)$. If $R^2(0) < \alpha_{1r}/|\alpha_{2r}|$, then $R(\tau_2)\to 0$ as $\tau_2 \to \infty$, whereas if $R^2(0) > \alpha_{1r}/|\alpha_{2r}|$, then $R(\tau_2)\to \infty$ at a finite time given by

$$\tau_{\text{ext}} = \frac{1}{2\alpha_{1r}} \ln\left[\frac{\alpha_{2r}R^2(0)}{\alpha_{1r}+\alpha_{2r}R^2(0)}\right] \tag{2.42}$$

When $\alpha_{1r}<0$ and $\alpha_{2r}<0$, again we find that $R(\tau_2)\to \infty$ at the time given by Eq. (2.42). Finally, when $\alpha_{1r}<0$ and $\alpha_{2r}>0$, the solution (2.41) approaches a constant $R(\tau_2)\to\sqrt{|\alpha_{1r}/\alpha_{2r}|}$ as $\tau_2\to\infty$, corresponding to a limit cycle. The three possible burning regimes are mapped out in the α_{1r}-α_{2r} parameter plane in Fig. 2.5. The long time behavior as a function of the four parameters Le_F, Le_O, ϕ and ΔT will be discussed next.

2.5. Results and Discussion

Our results demonstrate that the long time behavior of the chambered diffusion flame depends on the two coefficients α_{1r} and α_{2r} of Eq. (2.38) which in turn are determined by the four prescribed parameters Le_F, Le_O, ϕ and ΔT. The values of the coefficients α_{1r} and α_{2r} have been tested over a rather large range of parameters ($1 < Le_F < 4$, $1.2 < Le_O < 4$, $0.3 < \phi < 20$ and $-1 < \Delta T < 0.4$) for which α_{2r} is always found to be negative and α_{1r} always has the same sign as s, and hence s'. Therefore, when $Da < Da_{\mathrm{Cr}}$ the coefficients α_{1r} and α_{2r} lie in the third quadrant of the α_{1r}-α_{2r} diagram of Fig. 2.5, indicating an unstable flame. On the other hand, when $Da > Da_{\mathrm{Cr}}$, α_{1r} and α_{2r} lie in the fourth quadrant of the α_{1r} - α_{2r} diagram, and thus the flame is stable to small amplitude perturbations and unstable to perturbations of sufficiently large amplitude. Over this wide range of parameters, which describes most practical combustion systems, no limit cycle behavior is predicted, consistent with the experimental observations reported in [11-14]. However, we expect that limit cycles may exist when other effects such as heat loss are considered, as is the case in the numerical investigation of Sohn *et al.* [5]. Figures 2.6 ~ 2.8 show how the coefficients α_{1r} and α_{2r} vary with changes in each of the four parameters, Le_F, Le_O, ϕ and ΔT. The Damköhler number Da is chosen to be smaller than Da_{Cr} so that all the traces lie in the third quadrant of the α_{1r}-α_{2r} diagram. Because the value of α_{1r} is proportional to s', the traces for $Da > Da_{\mathrm{Cr}}$ with the same parameters are symmetric across the α_{2r} axis and hence lie in the fourth quadrant of the α_{1r}-α_{2r} diagram. Figures 2.6 and 2.7 show the variations of α_{1r} and α_{2r} with Le_O and Le_F for several values of ϕ with fixed $\Delta T = 0$. Figure 2.8 shows the variations of α_{1r} and

α_{2r} with ϕ for several values of ΔT and $Le_F = Le_O = 2$. The traces in Figs. 2.6 and 2.7 with the same values of ϕ start from the same points ($Le_F = 1$, $Le_O = 1.2$, $\Delta T = 0$ and ϕ=1, 2, 3, 4, respectively) and we see that the fuel Lewis number Le_F and oxidizer Lewis number Le_O have a very similar effect on α_{1r} and α_{2r}.

In Figs. 2.9 ~ 2.11 we show the evolution of the flame temperature perturbation u_f, given by

$$u_f = R(\tau_2)\cos\left(\theta(\tau_2) + c_0 t\right)$$

The values of parameters used in Fig. 2.9 are Le_F = 1, Le_O = 2, ϕ = 3, ΔT = 0 and $Da < Da_{\mathrm{Cr}}$ so that the solution lies in the third quadrant of the α_{1r} - α_{2r} diagram shown in Fig. 2.5. Figure 2.9 shows clearly the nonlinear oscillatory behavior leading to increased amplitude of perturbation, and eventually extinction at the time τ_{ext} given by Eq. (2.42). A similar response was predicted by Christiansen *et al.* [6] in their numerical simulation using detailed chemistry and transport. They found that once the maximum flame temperature drops below the critical value corresponding to the state of quasi-steady extinction during oscillation, the oscillation cannot recover and extinction occurs. The above expression for τ_{ext} provides an approximation for the computed extinction time.

Figures 2.10 and 2.11 were constructed using the same parameter values as Fig. 2.9, but with $s' > 0$ ($Da > Da_{\mathrm{Cr}}$) so that the values of α_{1r} and α_{2r} lie in the fourth quadrant of the α_{1r} - α_{2r} diagram. In Fig. 2.10 we have chosen $R^2(0) < \left|\alpha_{1r} / \alpha_{2r}\right|$, and the perturbation amplitude decays rapidly to zero. Figure 2.11 shows the nonlinear oscillation of the flame with the initial perturbation $R^2(0) > \left|\alpha_{1r} / \alpha_{2r}\right|$, and the amplitude of the perturbation is seen to grow with each oscillation, eventually blowing up in finite time.

Our prediction of a subcritical bifurcation to a nonlinear pulsating instability is consistent with the numerical results of Sohn *et al.* [5], and also with an early analysis by Joulin & Sivashinsky [15] on the nonlinear dynamics of premixed flames with Lewis numbers greater than unity. Sohn *et al.* [5] simulated a diffusion flame with the single set of parameters, $Le_F = Le_O = 2$, $\phi = 1$ and $\Delta T = 0$. They found that, when $Da > Da_{\mathrm{Cr}}$, the perturbation decays to zero and the flame is stable provided the initial amplitude is sufficiently small. However, for $Da < Da_{\mathrm{Cr}}$ the flame was predicted to evolve with unbounded oscillations, leading eventually to extinction. No limit cycle behavior was predicted for the chosen set of parameters in the absence of volumetric heat loss. Indeed, this set of parameters yields coefficients that lie in the third quadrant of the α_{1r} - α_{2r} diagram (when $Da < Da_{\mathrm{Cr}}$). In another study, Christiansen *et al*. [6] simulated a spherical methane-air diffusion flame with detailed chemistry and transport. The parameters used in their work were Le_F =2.3, Le_O =1.9, ϕ =13.73 and ΔT =0, which also lie in the third quadrant of the α_{1r} - α_{2r} plane, and they similarly found growing oscillations leading to extinction.

2.6. Conclusions

An evolution equation of the perturbation amplitude was derived in order to study the nonlinear dynamics of 1-D planar diffusion flames arising from pulsating instability. The Damköhler number Da of interest was chosen to be very close to the critical Damköhler number Da_{Cr} corresponding to the marginally stable state and the Lewis numbers were assumed greater than unity in order to focus on pulsating instabilities. Consequently, the transient flame oscillation behaviors exhibit weakly nonlinear characteristics. Our results

show that, when $Da < Da_{Cr}$, the flame extinguishes as the oscillation amplitude grows to large values. When $Da > Da_{Cr}$, the flame is stable unless a sufficiently large external perturbation is imposed, in which case a subcritical bifurcation to a pulsating flame, and ultimately extinction, takes place. Our predictions are consistent with available experimental and numerical results. Finally, our analysis also identifies a parameter space in which limit cycle behavior is possible. However, this regime falls outside the wide range of parameters typical of most practical combustion systems that are explored here. It is anticipated that additional effects not considered here, such as heat loss, may enable limit cycle behavior to be observed in practice.

Appendix

Following the same procedure as that in Cheatham & Matalon [7], the following homogeneous linear system can be derived from the jump and leakage conditions of leading order perturbations.

$$\begin{bmatrix} 1 & -1 & Le_F^{-1} & -Le_F^{-1} & 0 & 0 \\ 1 & -1 & 0 & 0 & Le_O^{-1} & -Le_O^{-1} \\ f_T & \frac{1}{2}-\lambda_T & f_F & \frac{1}{2}-Le_F^{-1}\lambda_F & 0 & 0 \\ f_T & \frac{1}{2}-\lambda_T & 0 & 0 & f_O & \frac{1}{2}-Le_O^{-1}\lambda_O \\ \frac{1-\gamma}{2}Le_F b_F & \frac{1+\gamma}{2}Le_F b_F & \frac{1-\gamma}{2}b_F-1 & 0 & 0 & \frac{1+\gamma}{2}\frac{Le_F}{Le_O}b_F \\ \frac{1-\gamma}{2}Le_O b_O & \frac{1+\gamma}{2}Le_O b_O & \frac{1-\gamma}{2}\frac{Le_O}{Le_F}b_O & 0 & 0 & \frac{1+\gamma}{2}b_O-1 \end{bmatrix} \begin{bmatrix} \Phi_T^+(\xi_f) \\ \Phi_T^-(\xi_f) \\ \Phi_F^+(\xi_f) \\ \Phi_F^-(\xi_f) \\ \Phi_O^+(\xi_f) \\ \Phi_O^-(\xi_f) \end{bmatrix} = \begin{bmatrix} 0 \\ 0 \\ 0 \\ 0 \\ 0 \\ 0 \end{bmatrix} \tag{2.A1}$$

where

$$f_J = -\frac{1}{2} + Le_J^{-1}\lambda_J \coth(\lambda_J \xi_f), \quad J = T, F, O$$

The values of $\Phi_J^{\pm}(\xi_f)$ can be calculated from the linear system (2.A1) and in turn the values of the constants $C_J^{\pm}$ can be obtained from them. Notice that the constants $C_J^{\pm}$ are proportional to each other. Without loss of generality, we can assume any of them, say C_T^+, unity.

Similarly, the jump and leakage conditions of the adjoint problem (2.35) produce the linear system

$$\begin{bmatrix} 1 & -1 & 0 & 0 & 0 & 0 \\ 0 & 0 & 1 & -1 & 0 & 0 \\ 0 & 0 & 0 & 0 & 1 & -1 \\ 0 & 1 & 0 & -Le_F & 0 & -Le_O \\ \bar{f}_T & \frac{1}{2}-\bar{\lambda}_T & \frac{1}{\chi}\frac{Le_F^2 b_F}{Le_O b_O}\bar{f}_F & \frac{1}{\chi}\frac{Le_F^2 b_F}{Le_O b_O}\left(\frac{1}{2}-Le_F^{-1}\bar{\lambda}_F\right) & \frac{Le_O}{\chi}\bar{f}_O & \frac{Le_O}{\chi}\left(\frac{1}{2}-Le_O^{-1}\bar{\lambda}_O\right) \\ \bar{f}_T & \frac{1-\gamma}{1+\gamma}\left(-\frac{1}{2}+\bar{\lambda}_T\right) & 0 & \frac{2Le_F^2}{1+\gamma}\left(\frac{1}{2}-Le_F^{-1}\bar{\lambda}_F\right) & -\frac{2Le_O^2}{1+\gamma}\bar{f}_O & 0 \end{bmatrix} \begin{bmatrix} \Psi_T^+(\xi_f) \\ \Psi_T^-(\xi_f) \\ \Psi_F^+(\xi_f) \\ \Psi_F^-(\xi_f) \\ \Psi_O^+(\xi_f) \\ \Psi_O^-(\xi_f) \end{bmatrix} = \begin{bmatrix} 0 \\ 0 \\ 0 \\ 0 \\ 0 \\ 0 \end{bmatrix}$$

(2.A2)

and the constants $E_J^{\pm}$ can be calculated in the same way.

At $O(\varepsilon)$, the jump & leakage conditions produce the following inhomogeneous linear systems

$$\begin{bmatrix} 1 & -1 & Le_F^{-1} & -Le_F^{-1} & 0 & 0 \\ 1 & -1 & 0 & 0 & Le_O^{-1} & -Le_O^{-1} \\ -\left(1-e^{\xi_f}\right)^{-1} & 0 & -\left(1-e^{Le_F\xi_f}\right)^{-1} & 0 & 0 & 0 \\ -\left(1-e^{\xi_f}\right)^{-1} & 0 & 0 & 0 & -\left(1-e^{Le_O\xi_f}\right)^{-1} & 0 \\ \frac{1-\gamma}{2}Le_F b_F & \frac{1+\gamma}{2}Le_F b_F & \frac{1-\gamma}{2}b_F-1 & 0 & 0 & \frac{1+\gamma}{2}\frac{Le_F}{Le_O}b_F \\ \frac{1-\gamma}{2}Le_O b_O & \frac{1+\gamma}{2}Le_O b_O & \frac{1-\gamma}{2}\frac{Le_O}{Le_F}b_O & 0 & 0 & \frac{1+\gamma}{2}b_O-1 \end{bmatrix} \begin{bmatrix} \Omega_T^+(\xi_f) \\ \Omega_T^-(\xi_f) \\ \Omega_F^+(\xi_f) \\ \Omega_F^-(\xi_f) \\ \Omega_O^+(\xi_f) \\ \Omega_O^-(\xi_f) \end{bmatrix} = \begin{bmatrix} 0 \\ 0 \\ 0 \\ 0 \\ q_5 \\ q_6 \end{bmatrix}$$

(2.A3)

and

$$\begin{bmatrix} 1 & -1 & Le_F^{-1} & -Le_F^{-1} & 0 & 0 \\ 1 & -1 & 0 & 0 & Le_O^{-1} & -Le_O^{-1} \\ g_T & \frac{1}{2}-\mu_T & g_F & \frac{1}{2}-Le_F^{-1}\mu_F & 0 & 0 \\ g_T & \frac{1}{2}-\mu_T & 0 & 0 & g_O & \frac{1}{2}-Le_O^{-1}\mu_O \\ \frac{1-\gamma}{2}Le_F b_F & \frac{1+\gamma}{2}Le_F b_F & \frac{1-\gamma}{2}b_F-1 & 0 & 0 & \frac{1+\gamma}{2}\frac{Le_F}{Le_O}b_F \\ \frac{1-\gamma}{2}Le_O b_O & \frac{1+\gamma}{2}Le_O b_O & \frac{1-\gamma}{2}\frac{Le_O}{Le_F}b_O & 0 & 0 & \frac{1+\gamma}{2}b_O-1 \end{bmatrix} \begin{bmatrix} \Theta_T^+(\xi_f) \\ \Theta_T^-(\xi_f) \\ \Theta_F^+(\xi_f) \\ \Theta_F^-(\xi_f) \\ \Theta_O^+(\xi_f) \\ \Theta_O^-(\xi_f) \end{bmatrix} = \begin{bmatrix} 0 \\ 0 \\ 0 \\ 0 \\ p_5 \\ p_6 \end{bmatrix}$$

(2.A4)

where

$$g_J = -\frac{1}{2}+Le_J^{-1}\mu_J \coth(\mu_J\xi_f), \quad J=T,F,O$$

$$q_5 = b_{F1}\left|F(\Phi)\right|^2, \quad q_6 = b_{O1}\left|F(\Phi)\right|^2$$

$$p_5 = \frac{1}{2}b_{F1}F^2(\Phi), \quad p_6 = \frac{1}{2}b_{O1}F^2(\Phi)$$

Thus, the constants $B_J^{\pm}$ and $D_J^{\pm}$ can be determined from the values of $\Omega_J^{\pm}\left(\xi_f\right)$ and $\Theta_J^{\pm}\left(\xi_f\right)$ computed from (2.A3) and (2.A4), respectively.

References

1. Cheatham, S., Ph.D. thesis, Northwestern University, USA (1997).
2. Lee, S. R. and Kim, J. S., *Combust. Theory Modelling* **4**: 29-46 (2000).
3. Lee, S. R. and Kim, J. S., *Combust. Theory Modelling* **6**: 263-278 (2002).
4. Sohn, C. H., Chung, S. H. and Kim, J. S., *Combust. Flame* **117**: 404-412 (1999).
5. Sohn, C. H., Kim, J. S., Chung, S. H. and Maruta, K., *Combust. Flame* **123**: 95-106 (2000).
6. Christiansen, E. W., Tse, S. D. and Law, C. K., *Combust. Flame* **134**: 263-278 (2003).
7. Cheatham, S. and Matalon, M., *J. Fluid Mech.* **414**: 105-144 (2000).
8. Kukuck, S. and Matalon, M., *Combust. Theory Modelling* **5**: 217-240 (2001).
9. Liñán, A., *Acta Astronautica* **1**: 1007-1039 (1974).
10. Kim, J. S. and Williams, F. A., *J. Eng. Math.* **31**: 101-118 (1997).
11. Chan, W. and T'ien, J., *Combust. Sci. Technol.* **18**: 139-143 (1978).
12. Ross, H. D., Sotos, R. G. and T'ien, J. S., *Combust. Sci. Technol.* **75**: 155-160 (1991).
13. Nayagam, V. and Williams, F. A., *7th Int. Conf. on Numerical Combustion*, New York (1998).
14. Furi, M., Papas, P. and Monkewitz, P. A., *Proc. Combust. Inst.* **28**: 831-838 (2000).
15. Joulin, G. and Sivashinsky, G. I., *Combust. Sci. Technol.* **55**: 83-88 (1987).

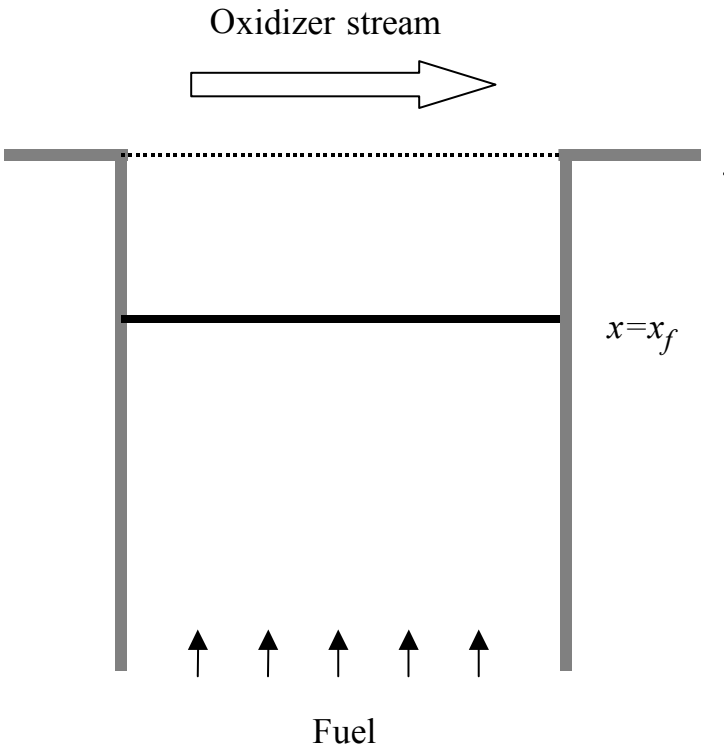

Figure 2.1. The one-dimensional flame configuration.

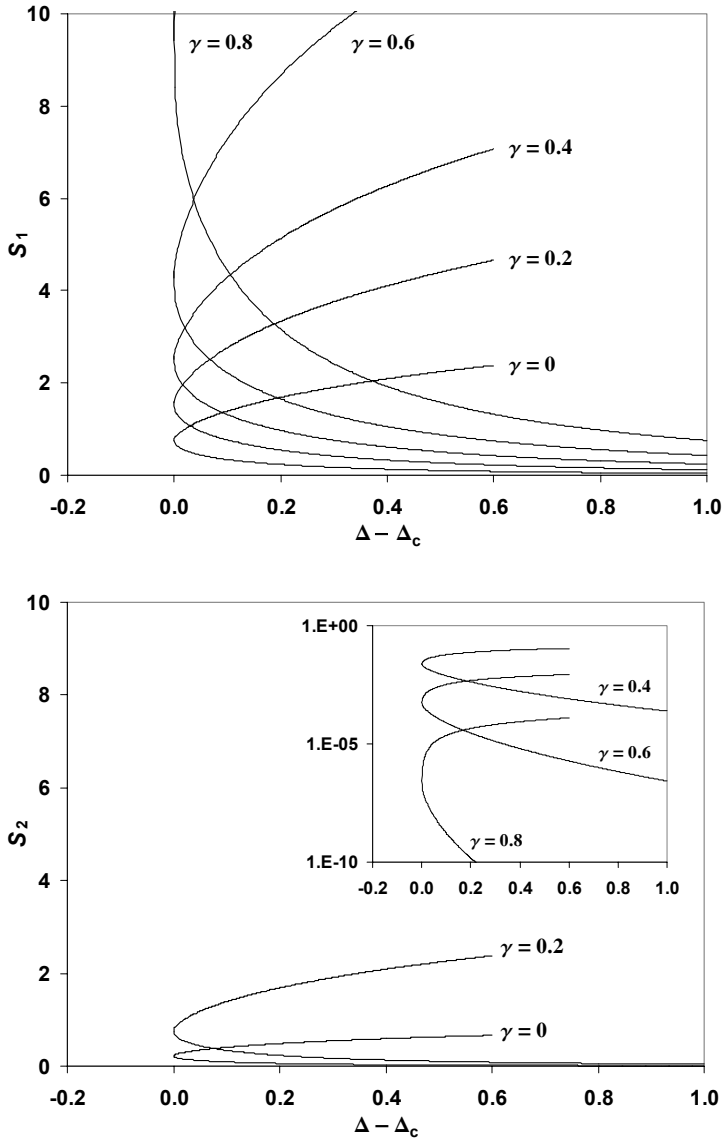

Figure 2.2. Leakage functions S_1 and S_2 as functions of $|\gamma|$ and Δ; for $\gamma > 0$ they correspond to S_F and S_O and for $\gamma < 0$ to S_O and S_F, respectively.

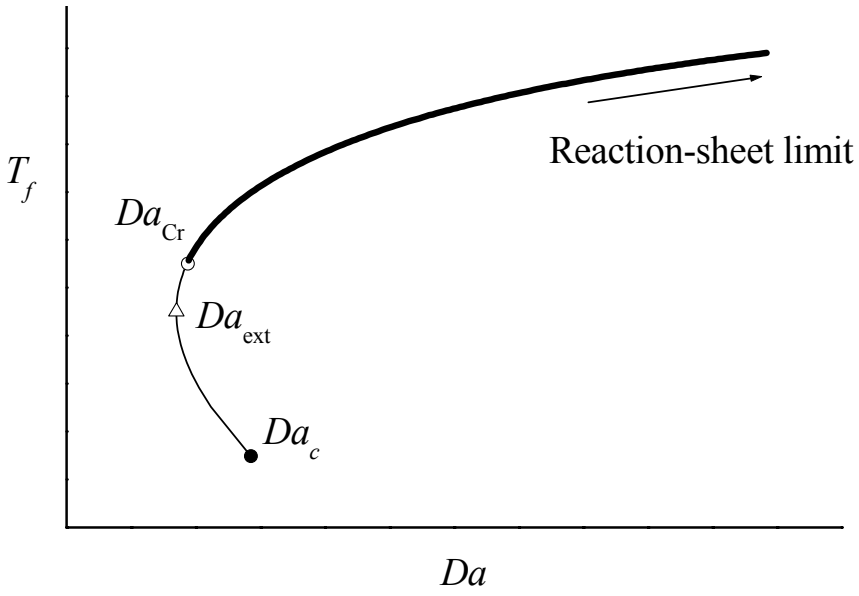

Figure 2.3. Schematic of a typical response curve of flame temperature T_f to the Damköhler number Da with the points Da_{ext} and Da_{Cr} corresponding to the extinction and onset of instability, respectively.

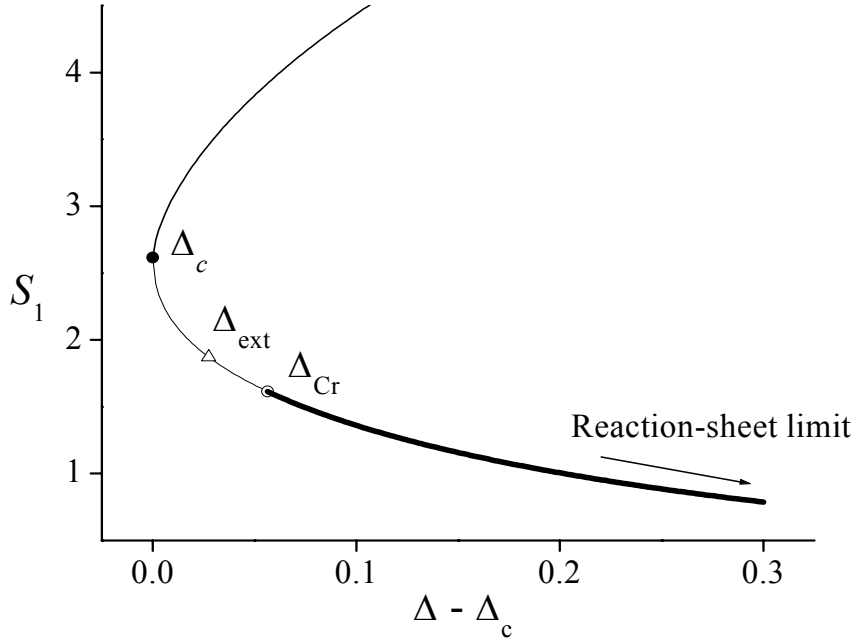

Figure 2.4. Schematic of a typical response curve of reactant leakage to the reduced Damköhler number Δ with the points Δ_{ext} and Δ_{Cr} corresponding to the extinction and onset of instability, respectively.

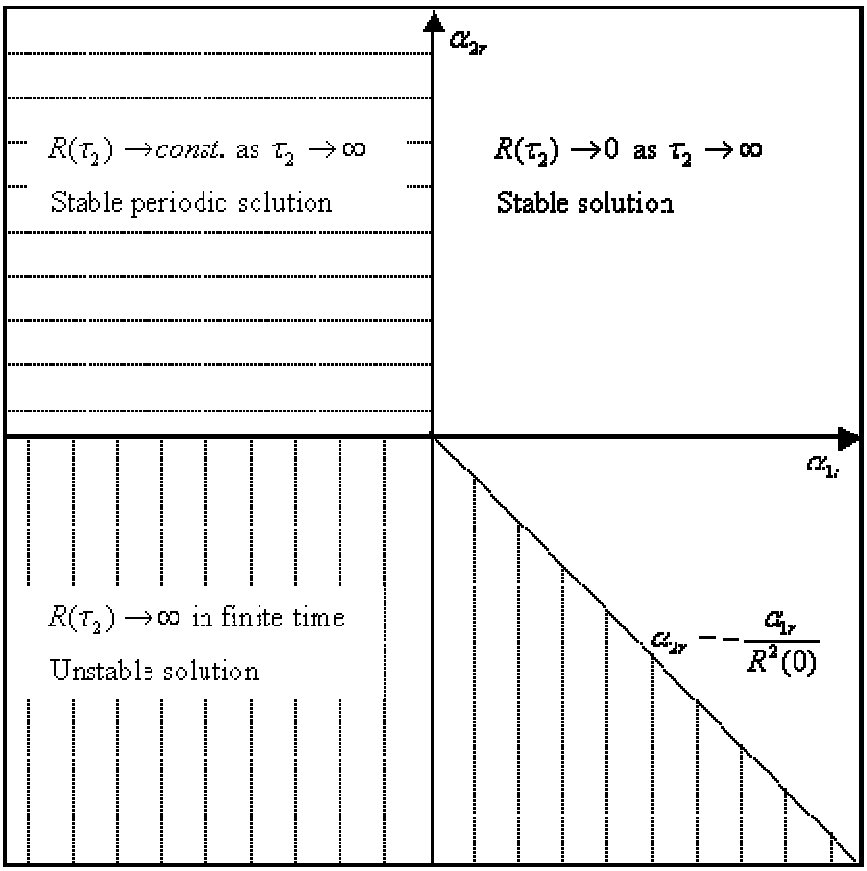

Figure 2.5. The long time behavior of $R(\tau_2)$ mapped out in the α_{1r} - α_{2r} parameter plane.

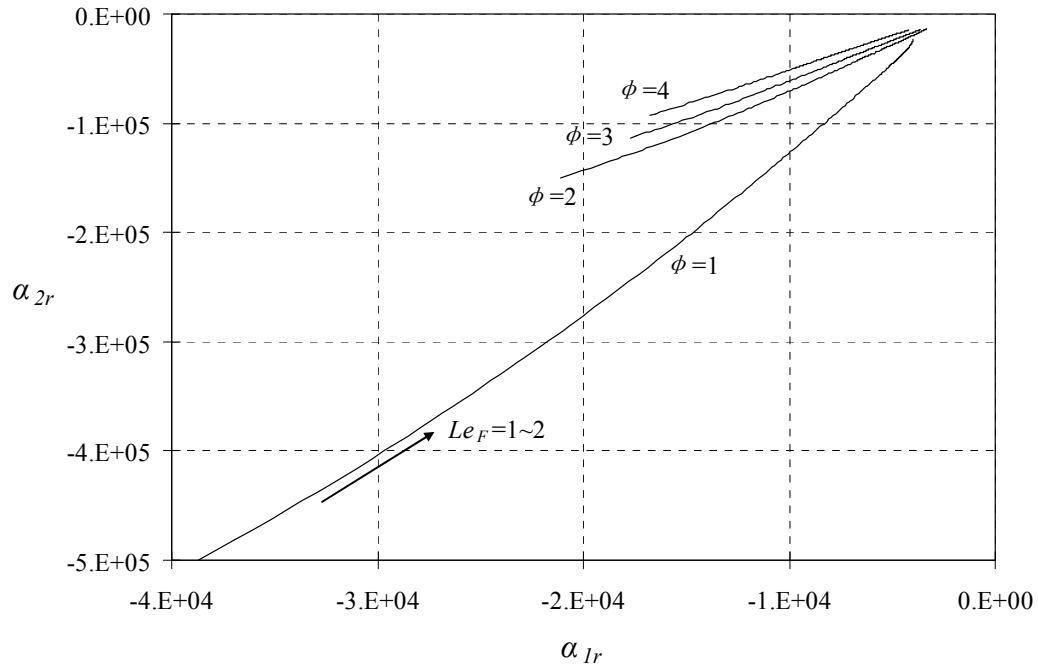

Figure 2.6. Variation of α_{1r} and α_{2r} with Le_F for several values of ϕ (with Le_O=1.2, $\Delta T = 0$ and $Da < Da_{\mathrm{Cr}}$).

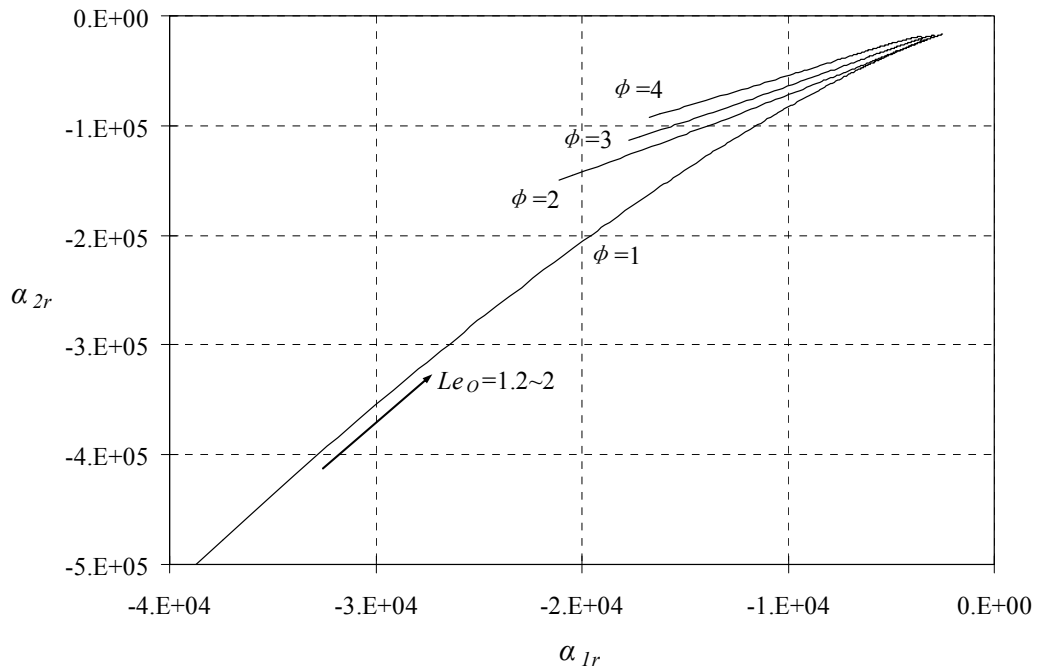

Figure 2.7. Variation of α_{1r} and α_{2r} with Le_O for several values of ϕ (with Le_F =1, $\Delta T = 0$ and $Da < Da_{Cr}$).

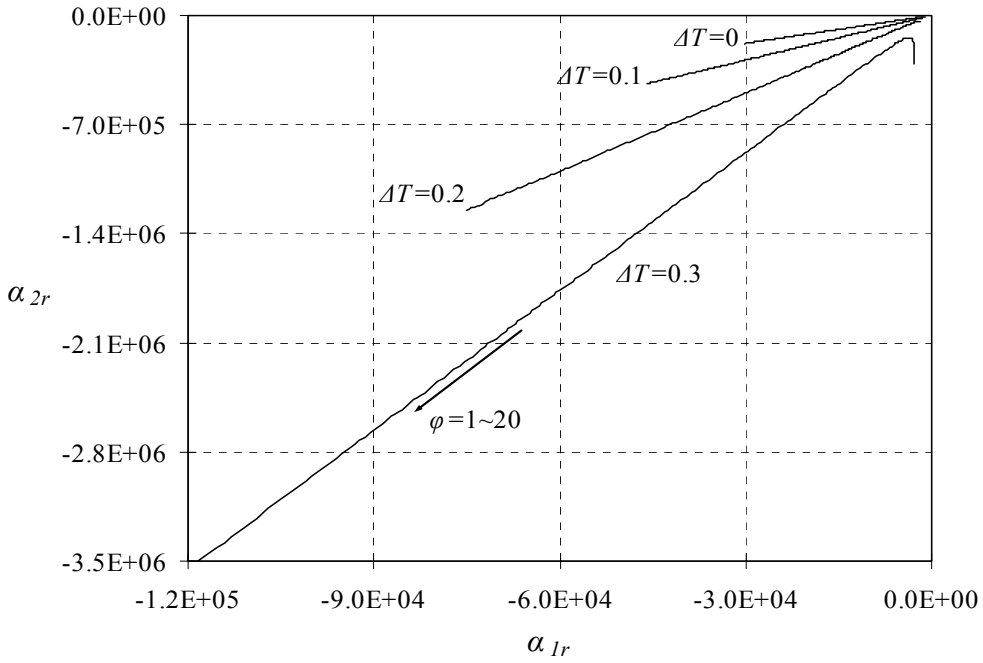

Figure 2.8. Variation of α_{1r} and α_{2r} with ϕ for several values of ΔT (with $Le_F = Le_O = 2$ and $Da < Da^*$).

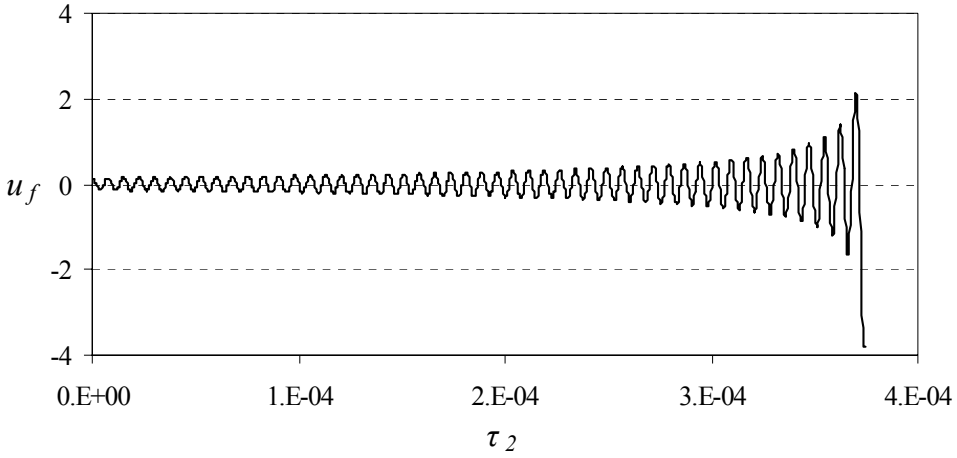

Figure 2.9. Flame temperature perturbation u_f as a function of slow time τ_2 for $Da < Da_{\mathrm{Cr}}$, with $Le_F = 1$, $Le_O = 2$, $\phi = 3$ and $\Delta T = 0$.

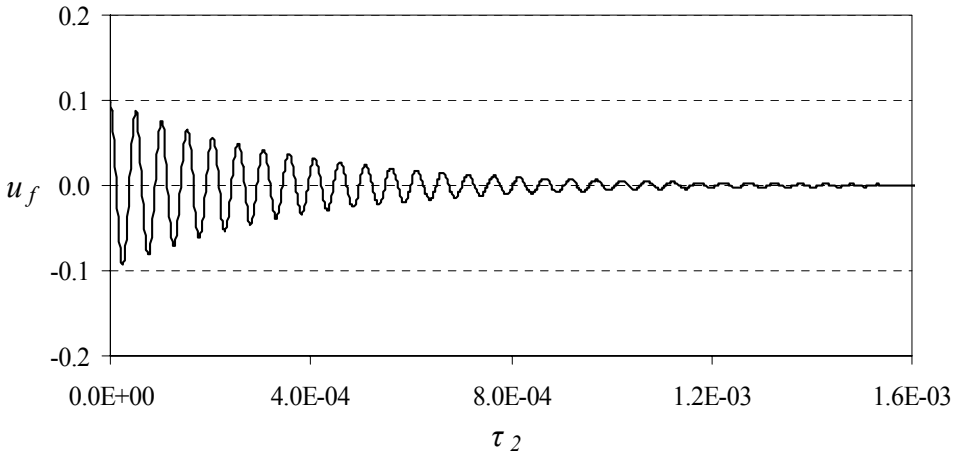

Figure 2.10. Flame temperature perturbation u_f as a function of slow time τ_2 for $Da >$ Da_{Cr}. The initial perturbation $R^2(0)$ is chosen to be smaller than $\left|\alpha_{1r}/\alpha_{2r}\right|$. ($Le_F$=1, Le_O=2, ϕ=3, ΔT=0).

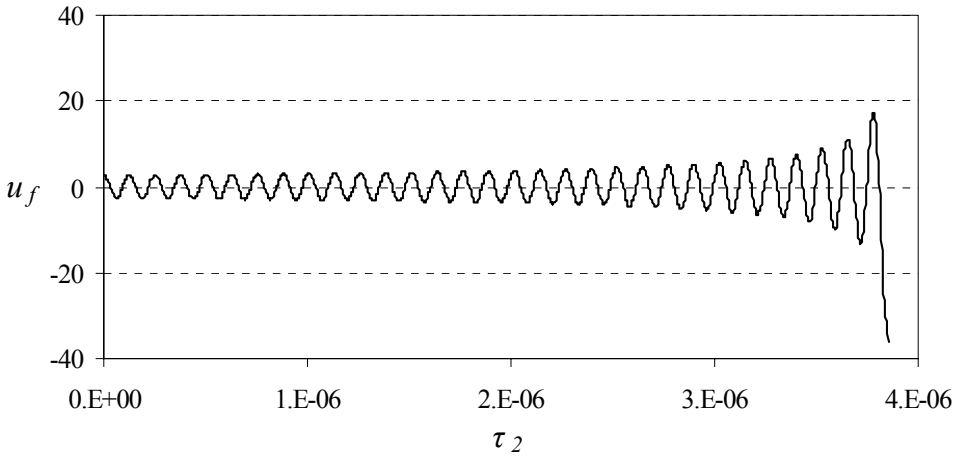

Figure 2.11. Flame temperature perturbation u_f as a function of slow time τ_2 for $Da >$ Da_{Cr}. The initial perturbation $R^2(0)$ is chosen to be larger than $\left|\alpha_{1r}/\alpha_{2r}\right|$. (Le_F =1, Le_O =2, ϕ =3, ΔT =0).

Chapter 3: Forced Oscillation in Diffusion Flames near Thermal-Diffusive Resonance

In this chapter, we study the forced flame oscillations in planar diffusion flames by incorporating the external forcing into the analysis of Chapter 2. Of particular interest is the resonance phenomenon between the forced and intrinsic flame oscillations driven by the thermal-diffusive instability. A linear response is first examined to identify the critical condition for the resonance to occur. The nonlinear near-resonant response is then studied with the Damköhler number *Da* chosen to be very close to the critical value by deriving an evolution equation for the amplitude of forced oscillation.

3.1. Formulation

We adopt the same flame configuration and asymptotic model as those in Chapter 2. The external forcing is introduced by independently imposing a flow field with small amplitude oscillations. Thus, the appropriate nondimensional governing equations in the convective-diffusive zone can be written as

$$\frac{\partial T}{\partial t} + U\frac{\partial T}{\partial x} - \frac{\partial^2 T}{\partial x^2} = 0 \tag{3.1}$$

$$\frac{\partial Y_F}{\partial t} + U\frac{\partial Y_F}{\partial x} - Le_F^{-1}\frac{\partial^2 Y_F}{\partial x^2} = 0 \tag{3.2}$$

$$\frac{\partial Y_O}{\partial t} + U\frac{\partial Y_O}{\partial x} - Le_O^{-1}\frac{\partial^2 Y_O}{\partial x^2} = 0 \tag{3.3}$$

The velocity U is expressed as

$$\begin{aligned} U &= 1+\beta^{-1}\varepsilon H(t) \\ H(t) &= h\exp(ict)+c.c. \end{aligned} \tag{3.4}$$

where ε is a small parameter satisfying $\beta^{-1} << \varepsilon << 1$, h the amplitude of velocity fluctuation, c the forced frequency and *c.c.* denotes the complex conjugate. Equations (3.1)-(3.4) are subjected to the boundary conditions, jump relations and leakage conditions given by Eqs. (2.4)-(2.9) of Chapter 2.

3.2. Linear Response

A linear analysis is first conducted by assuming $h = 1$ such that the velocity fluctuation is of $O(\beta^{-1}\varepsilon)$ relative to its mean value, as shown in Eq. (3.4). The solution under the harmonic fluctuating velocity field (3.4) can be written in the form of steady-state base solutions for temperature, mass fractions of fuel and oxidant, and the flame-sheet location under unity flow field plus a correction term accounting for the small velocity fluctuation:

$$T = T_b(x) + \beta^{-1}\varepsilon u(x,t) \tag{3.5}$$

$$Y_F = Y_{F,b}(x) + \beta^{-1}\varepsilon v(x,t) \tag{3.6}$$

$$Y_O = Y_{O,b}(x) + \beta^{-1}\varepsilon w(x,t) \tag{3.7}$$

$$x_f = x_{f,b} + \beta^{-1}\varepsilon l(x,t) \tag{3.8}$$

where u, v, w, and l are the correction terms for temperature, mass fractions of fuel and oxidant, and flame sheet location, respectively, and the base solutions T_b, $Y_{F,b}$, $Y_{O,b}$, and $x_{f,b}$ are respectively given by Eqs (2.12)-(2.13) in Chapter 2. We note that the unsteady

fluctuations induced by the perturbed flow field (3.4) are of O($\beta^{-1}\varepsilon$). The magnitude of these terms is sufficient to elicit an $O(1)$ response due to the extreme sensitivity of the Arrhenius reaction rate term. Substituting Eqs. (3.5)-(3.8) into the governing equations (3.1)-(3.3) for T, Y_F and Y_O and their boundary conditions, jump and leakage conditions (2.4)-(2.9) yields the governing equations for u, v and w:

$$u_t + u_x - u_{xx} = -\varepsilon\left(T_0\right)_x \exp(ict) + c.c. \tag{3.9}$$

$$v_t + v_x - Le_F^{-1} v_{xx} = -\varepsilon\left(Y_{F,0}\right)_x \exp(ict) + c.c. \tag{3.10}$$

$$w_t + w_x - Le_O^{-1} w_{xx} = -\varepsilon\left(Y_{O,0}\right)_x \exp(ict) + c.c. \tag{3.11}$$

subject to the same boundary, jump and leakage conditions as those given by Eqs. (2.23)-(2.27) in Chapter 2, where T_0, $Y_{F,0}$ and $Y_{O,0}$ are the leading-order base solutions in terms of β^{-1}, and the subscript "x" denotes differentiation with respect to x. Here and hereafter, all the unspecified parameters are the same as those defined in Chapter 2. Equations (3.9)-(3.11) imply that the flame oscillates under the external harmonic driving force due to the velocity fluctuation.

The solutions to u, v and w assume the form

$$\phi(x,t) = \phi_p(x)\exp(ict) + c.c. + \phi_c(x)\exp(\sigma t), \quad \phi = u, v, w$$

where the particular solution $\phi_p(x)\exp(ict)+c.c.$ accounts for the response to the velocity fluctuation and the common solution $\phi_c(x)\exp(\sigma t)$ is associated with the intrinsic instability. σ is a complex number whose real part identifies the growth rate. The Damköhler number Da of interest here is larger than its critical value Da_{Cr} corresponding to the marginal state of intrinsic instability. Thus, the flame is intrinsically stable so that the common solution $\phi_c(x)\exp(\sigma t)$ will damp out eventually, and hereafter, only the

particular solution $\phi_p(x)\exp(ict)+c.c.$ is considered. It should be noted that $u_p(x)$, $v_p(x)$ and $w_p(x)$ are complex functions whose modulus denote the oscillation amplitude while the phase angle denotes the phase shift of the oscillation from the imposed velocity fluctuation. The solutions to $u_p(x)$, $v_p(x)$ and $w_p(x)$ are

$$u_p(x) = \begin{cases} B_1 \exp[(1/2+\Lambda_T)x] + \dfrac{i}{c}(e^{-\xi_f} + \Delta T - 1)e^x, & x < x_f \\ B_2\{\exp[(1/2+\Lambda_T)x] - \exp[(1/2-\Lambda_T)x]\} + \\ \dfrac{i}{c}(\Delta T - 1)\{e^x - \exp[(1/2-\Lambda_T)x]\}, & x > x_f \end{cases}$$

$$v_p(x) = \begin{cases} C_1 \exp[(Le_F/2+\Lambda_F)x] - \dfrac{i}{c}Le_F e^{Le_F(x-\xi_f)}, & x < x_f \\ C_2\{\exp[(Le_F/2+\Lambda_F)x] - \exp[(Le_F/2-\Lambda_F)x]\}, & x > x_f \end{cases}$$

$$w_p(x) = \begin{cases} D_1 \exp[(Le_O/2+\Lambda_O)x], & x < x_f \\ D_2\{\exp[(Le_O/2+\Lambda_O)x] - \exp[(Le_O/2-\Lambda_O)x]\} + \\ \dfrac{i}{c}(1+\phi^{-1})Le_O\{e^{Le_O x} - \exp[(Le_O/2-\Lambda_O)x]\}, & x > x_f \end{cases}$$

where

$$\Lambda_J = \frac{1}{2}\sqrt{Le_J^2 + 4iLe_J c}, \qquad J = T, F, O$$

with $Le_T = 1$. The constants B_1, B_2, C_1, C_2, D_1 and D_2 are obtained by applying the jump and leakage conditions (2.24)-(2.27), which yield the inhomogeneous linear system

$$\begin{bmatrix} 1 & -1 & Le_F^{-1} & -Le_F^{-1} & 0 & 0 \\ 1 & -1 & 0 & 0 & Le_O^{-1} & -Le_O^{-1} \\ F_T & \frac{1}{2}-\Lambda_T & F_F & \frac{1}{2}-Le_F^{-1}\Lambda_F & 0 & 0 \\ F_T & \frac{1}{2}-\Lambda_T & 0 & 0 & F_O & \frac{1}{2}-Le_O^{-1}\Lambda_O \\ \frac{1-\gamma}{2}Le_F b_F & \frac{1+\gamma}{2}Le_F b_F & \frac{1-\gamma}{2}b_F-1 & 0 & 0 & \frac{1+\gamma}{2}\frac{Le_F}{Le_O}b_F \\ \frac{1-\gamma}{2}Le_O b_O & \frac{1+\gamma}{2}Le_O b_O & \frac{1-\gamma}{2}\frac{Le_O}{Le_F}b_O & 0 & 0 & \frac{1+\gamma}{2}b_O-1 \end{bmatrix} \begin{bmatrix} u_p^+ \\ u_p^- \\ v_p^+ \\ v_p^- \\ w_p^+ \\ w_p^- \end{bmatrix} = \frac{i}{c}\begin{bmatrix} 0 \\ 0 \\ q_3 \\ q_4 \\ 0 \\ 0 \end{bmatrix} \tag{3.12}$$

where

$$F_J = -\frac{1}{2} + Le_J^{-1}\Lambda_J \coth(\Lambda_J \xi_f), \quad J = T, F, O$$

$$\begin{aligned} q_3 = {} & (1/2-\Lambda_T)[1+(\Delta T-1)e^{\xi_f}]-(\Delta T-1)e^{\xi_f}[1/2-\Lambda_T\coth(\Lambda_T\xi_f)] \\ & -(\Delta T-1)\Lambda_T[1+\coth(\Lambda_T\xi_f)]\exp[(1/2-\Lambda_T)\xi_f]-(1/2-Le_F^{-1}\Lambda_F)Le_F \end{aligned}$$

$$\begin{aligned} q_4 = {} & (1/2-\Lambda_T)[1+(\Delta T-1)e^{\xi_f}]-(\Delta T-1)e^{\xi_f}[1/2-\Lambda_T\coth(\Lambda_T\xi_f)] \\ & -(\Delta T-1)\Lambda_T[1+\coth(\Lambda_T\xi_f)]\exp[(1/2-\Lambda_T)\xi_f] \\ & -(1+\phi^{-1})Le_O[1/2-Le_O^{-1}\Lambda_O\coth(\Lambda_O\xi_f)]e^{Le_O\xi_f} \\ & -(1+\phi^{-1})\mu_O[1+\coth(\mu_O\xi_f)]\exp[(Le_O/2-\mu_O)\xi_f] \end{aligned}$$

and u_p^+, u_p^-, v_p^+, v_p^-, w_p^+ and w_p^- are the values of u_p, v_p and w_p at the oxidant and fuel sides of the flame sheet, respectively. The coefficient matrix in Eq. (3.12) depends on the four prescribed parameters Le_F, Le_O, ϕ and ΔT defining the combustion system, the imposed frequency c, and the Damköhler number Da. The amplitude and phase shift of forced oscillations for T, Y_F and Y_O at both sides of the flame sheet can be obtained from u_p^+, u_p^-, v_p^+, v_p^-, w_p^+ and w_p^- by solving Eq. (3.12). However, under certain Damköhler numbers and forced frequencies, the determinant of the coefficient matrix in Eq. (3.12) could be zero, leading to infinitely large values of u_p^+, u_p^-, v_p^+, v_p^-, w_p^+ and w_p^-, i.e.

infinitely large amplitude of flame oscillations even under an $O(\varepsilon)$ weak forcing. This implies that resonance occurs under such an external forcing. The linear stability analysis performed by Kukuck & Matalon [1] for the intrinsic oscillation of the same flame yields a homogeneous linear system with the same coefficient matrix. The solvability condition, vanishing of the determinant of the coefficient matrix, produced the critical frequency and Damköhler number, c_0 and Da_{Cr}, corresponding to the marginally stable state. Thus, the imposed frequency and Damköhler number at resonance are identical to those at the onset of intrinsic oscillation, and hence the resonance occurs between the external forcing and intrinsic oscillation of the flame. Consequently, two conditions are required for the resonance of diffusion flames to occur: the flame is close to the stability boundary, i.e., $Da \to Da_{Cr}$, and the imposed frequency c approaches the critical frequency c_0.

The inhomogeneous system (3.12) gives the dependence of the amplitude and phase shifts of forced oscillation on the imposed frequency c and the Damköhler number Da. Figure 3.1 shows the amplitude of u_p^+ versus the imposed frequency c for different values of Da. It is seen that when the flame is at the instability boundary, i.e. $Da = Da_{\mathrm{Cr}}$, the imposed velocity fluctuation induces infinitely large flame oscillations, i.e. resonance, as c approaches c_0. For Da sufficiently larger than Da_{Cr}, the oscillation amplitude decreases monotonically with increasing c, while for Da close enough to Da_{Cr}, the oscillation amplitude peaks at the frequency close to but smaller than the natural frequency c_0. This differs from previous investigations that predicted only the monotonic attenuation of forced oscillation with the increase of the imposed frequency. Now we know that this monotonic dependence holds only when the flame is sufficiently away from the unstable state so that the resonance between the external forcing and intrinsic

oscillation of flame does not occur. Figure 3.2 shows variations of the phase shifts of u_p^+, u_p^-, v_p^+, v_p^- w_p^+ and w_p^- with the Damköhler number Da for $c = c_0$. It is seen that the oscillation of reactant leakages v_p^+ and w_p^- are always in phase. As Da approaches Da_{Cr}, i.e. the flame approaches the resonance condition, temperature oscillations on both sides of the flame sheet, u_p^+ and u_p^-, become in phase and oscillations of the mass fractions of fuel and oxidant on both sides of the flame sheet, v_p^+, v_p^- w_p^+ and w_p^-, become in phase as well. The phase difference between oscillations of temperature, u_p^+ and u_p^-, and mass fractions, v_p^+, v_p^- w_p^+ and w_p^-, is π when the flame is at resonance, indicating they are out of phase. This is because higher flame temperatures lead to less reactant leakages, and vice versa.

3.3. Nonlinear Response

The preceding analysis predicts infinite oscillation amplitude at the resonant frequency. However, the amplitude is expected to be limited by the inherent nonlinearities in the problem. Here we derive an evolution equation for the amplitude of forced oscillation near resonance. We adopt the scalings:

$$h = \varepsilon^2$$

$$(Da - Da_{\mathrm{Cr}}) / Da_{\mathrm{Cr}} = \varepsilon^2$$

$$(c - c_0) / c_0 = \omega\varepsilon^2 \tag{3.13}$$

so that the flame oscillation exhibits a weakly nonlinear characteristic and a long time transient behavior. Thus we introduce the "slow time" variables

$$\tau_1 = \varepsilon t, \quad \tau_2 = \varepsilon^2 t$$

associated with the long time transient behavior. The velocity fluctuation $H(t)$ can be rewritten as

$$H(t) = \varepsilon^3 \exp(ic_0\tau) + c.c.$$

where $\tau = t + \omega\tau_2$.

We expand the variables u_p, v_p and w_p in a power series in ε,

$$(u_p, v_p, w_p) = \sum_{m=0}^{\infty} (u_m, v_m, w_m)\varepsilon^m$$

and expand the governing equations, boundary, jump and leakage conditions for u, v and w (2.24)-(2.27) in terms of ε. Following the same process as that in Chapter 2, we can solve, to $O(1)$,

$$(u_0, v_0, w_0) = \begin{cases} A(\tau_1, \tau_2)\Phi_J^-(x)\exp(ic_0\tau) + c.c., & x < x_f \\ A(\tau_1, \tau_2)\Phi_J^+(x)\exp(ic_0\tau) + c.c., & x > x_f \end{cases}$$

Then from the solvability condition of higher order solutions, we have, to O(ε),

$$\partial A / \partial \tau_1 = 0$$

such that $A = A(\tau_2)$. Finally, at O(ε^2), we obtain the nonlinear evolution equation for the amplitude of oscillation

$$A' + (s\alpha_1 + ic_0\omega)A + \alpha_2 A|A|^2 + \alpha_3 = 0 \tag{3.14}$$

where

$$\alpha_3 = \frac{\alpha_{30}}{\alpha_0}$$

$$\alpha_{30} = \int_{-\infty}^{\xi_f} \left[\overline{\Psi}_T^-(T_0^-)_x + Le_F \overline{\Psi}_F^-(Y_{F,0}^-)_x + Le_O \overline{\Psi}_O^-(Y_{O,0}^-)_x \right] dx + \int_{\xi_f}^{0} \left[\overline{\Psi}_T^+(T_0^+)_x + Le_F \overline{\Psi}_F^+(Y_{F,0}^+)_x + Le_O \overline{\Psi}_O^+(Y_{O,0}^+)_x \right] dx$$

and all the other coefficients have been defined in Chapter 2. Note that the amplitude function A is complex and hence includes the information of both amplitude and phase. We construct solutions by first writing the amplitude function A in the polar form and separating α_1, α_2, and α_3 into their real and imaginary parts:

$$A = R(\tau_2)\exp[i\theta(\tau_2)]$$

$$\alpha_1 = \alpha_{1r} + i\alpha_{1i}, \quad \alpha_2 = \alpha_{2r} + i\alpha_{2i}, \quad \alpha_3 = \alpha_{3r} + i\alpha_{3i}$$

where R is the amplitude and θ the polar angle indicating phase shift. The complex evolution equation (3.14) can now be expressed as two real equations, for the amplitude and the phase shift:

$$R' + s\alpha_{1r}R + \alpha_{2r}R^3 + \alpha_{3r}\cos\theta + \alpha_{3i}\sin\theta = 0 \tag{3.15}$$

$$R\theta' + (s\alpha_{1i} + c_0\omega)R + \alpha_{2i}R^3 + \alpha_{3i}\cos\theta - \alpha_{3r}\sin\theta = 0 \tag{3.16}$$

We note that the evolution equations (3.14) or (3.15) and (3.16) have a very similar form as those describing nonlinear oscillators, e.g. the Van der Pol oscillator, under weak damping and forcing [2]. A simple comparison of these systems shows that the term $s\alpha_1$ in Eqs. (3.14) and (3.15), which quantifies the deviation of Da from Da_{Cr}, plays the role of damping for the forced flame oscillation.

Here, we study the steady-state solutions of Eqs. (3.15) and (3.16) in order to access the final amplitude and phase of the forced flame oscillation under external forcing. Combining the steady-state forms of equations (3.15) and (3.16) yields the following cubic equation for R^2

$$R^6 + \frac{2\left[s\left(\alpha_{1r}\alpha_{2r} + \alpha_{1i}\alpha_{2i}\right) + c_0\omega\alpha_{2i}\right]}{\left|\alpha_2\right|^2}R^4 + \frac{\left(s\alpha_{1r}\right)^2 + \left(s\alpha_{1i} + c_0\omega\right)^2}{\left|\alpha_2\right|^2}R^2 - \frac{\left|\alpha_3\right|^3}{\left|\alpha_2\right|^2} = 0 \qquad (3.17)$$

Equation (3.17) will possess three real and positive solutions whenever the following inequality is satisfied

$$\left|\frac{\alpha_{2i}}{\alpha_{2r}}\right| \geq \sqrt{3} \qquad (3.18)$$

It has a single real solution otherwise. We now consider the dependence of α_2 on the four prescribed parameters, Le_F, Le_O, ϕ and ΔT. In Fig. 3.3, we plot its variations with each prescribed parameter to determine conditions (if any) for which the inequality in Eq. (3.18) is satisfied, which would indicate multiplicity of solutions. The transition boundary, $\left|\alpha_{2i} / \alpha_{2r}\right| = \sqrt{3}$, is also plotted in each figure. As seen in Fig. 3.3, we have found that for a wide range of realistic parameter values, all curves lie to the left of the transition boundary, indicating that solutions to Eq. (3.17) are single-valued.

We now investigate the sensitivity of flames to the imposed velocity oscillations under different prescribed parameters through this single-valued solution. Figure 3.4 shows variation of the amplitude of forced oscillation, R, with the normalized frequency ω, defined in Eq. (3.13), for $Da = Da_{\mathrm{Cr}}$, $Le_F = 2$, $Le_O = 2$, $\phi = 1$ and $\Delta T = 0$. It is seen that the dependence of R on the imposed frequency shows similar behavior as those in Fig. 2.2 for Da slightly larger than Da_{Cr}, in that it peaks at the frequency close to but slightly smaller than the intrinsic flame oscillation frequency c_0. The finite amplitude of forced oscillation at the resonance condition, i.e. $Da = Da_{\mathrm{Cr}}$ and $c = c_0$, is due to the nonlinear effects considered through the nonlinear analysis. We hence can plot the dependence of this peak amplitude, $R_{\max}$, on the system parameters such as Le_F, Le_O, ϕ and ΔT to

examine at what conditions the flame is able to achieve the largest R_{max} and hence is most responsive to the external forcing. Since the maximum amplitude of forced oscillation is achieved under the smallest damping, R_{max} can be solved from Eq. (3.17), by setting the damping effect $s = 0$, as $R_{max} = (\alpha_3 / \alpha_{2r})^{1/3}$, which can be derived to occur at the normalized frequency $\omega = -\alpha_{2i}(\alpha_3 / \alpha_{2r})^{2/3}$. Thus, due to the nonlinearity, the flame oscillates with the maximum amplitude at the imposed frequency not necessarily equal to the natural frequency, c_0. It is noted that whether the maximum amplitude, R_{max}, occurs at the frequency smaller or larger than c_0 depends on the sign of α_{2i}, which in turns depends on the prescribed parameters. The peaking of the curves at $c < c_0$ shown in Figs. 3.1 and 3.4 is due to the parameters we have used, $Le_F = 2$, $Le_O = 2$, $\phi = 1$ and $\Delta T = 0$ that yield a positive α_{2i}. Figure 3.5 shows variations of R_{max} with Le_F for different values of ϕ. It is seen that except for $\phi = 1$, R_{max} increases monotonically with Le_F. In fact, R_{max} peaks at a much larger Le_F, e.g. $Le_F = 14.4$ for $\phi = 3$, which is out of the range of this plot. Since for most hydrocarbon–air diffusion flames $\phi > 1$ and fuels with such large Lewis number are rare, it can be considered that R_{max} increases with Le_F monotonically. Thus, in general the flame is more sensitive to the external forcing for larger Le_F.

Figure 3.6 shows variations of R_{max} with Le_O for different values of ϕ. It is seen that for $\phi > 1$ most of the $R_{max} \sim Le_O$ curves peak within the range of $1 < Le_O < 2$, which is a more practical range for the oxidant. Thus, flames with Le_O falling in this range are most responsive to the external forcing. Furthermore, it is seen from Figs. 3.5 and 3.6 that except for smaller Le_O where R_{max} is not sensitive to ϕ, R_{max} decreases with increasing ϕ over most of the parameter range for Le_F and Le_O. Figure 3.7 shows variations of R_{max}

with ϕ for different values of ΔT. It is seen that R_{max} decreases monotonically with increasing ϕ over most of its range except for larger ΔT and smaller ϕ, under which R_{max} increases with increasing ϕ over a very narrow range of ϕ. Thus, flames with smaller ϕ, in general, are more responsive to the external forcing.

3.4. Conclusions

The response of flame oscillations to external velocity fluctuations of small amplitude is examined. An analysis on the linear response is first conducted and the results show that when the flame is near the boundary of thermal-diffusive pulsating instability, the velocity fluctuation may induce resonance as the fluctuation frequency approaches the natural frequency of the intrinsic oscillation. Thus, the amplitude-frequency response curve exhibits a peak around the natural frequency. Monotonic dependence of the oscillation amplitude on the forced frequency holds only when the flame is sufficiently away from resonance. A nonlinear near-resonant response is then conducted to study the effects of inherent nonlinearities on the response of flame oscillation by deriving an evolution equation for the amplitude of forced oscillation. Examination of the derived evolution equation reveals that, in most situations, flames with larger Le_F, smaller ϕ and ΔT, and $1 < Le_O < 2$ have the largest oscillation amplitude at resonance. Thus, these flames are most responsive to the external forcing.

References

1. Kukuck, S. and Matalon, M., *Combust. Theory Modelling* **5**: 217-240 (2001).
2. Kevorkian, J. and Cole, J. D., *Perturbation Methods in Applied Mathematics*, Springer, New York, pp. 141-151 (1981).

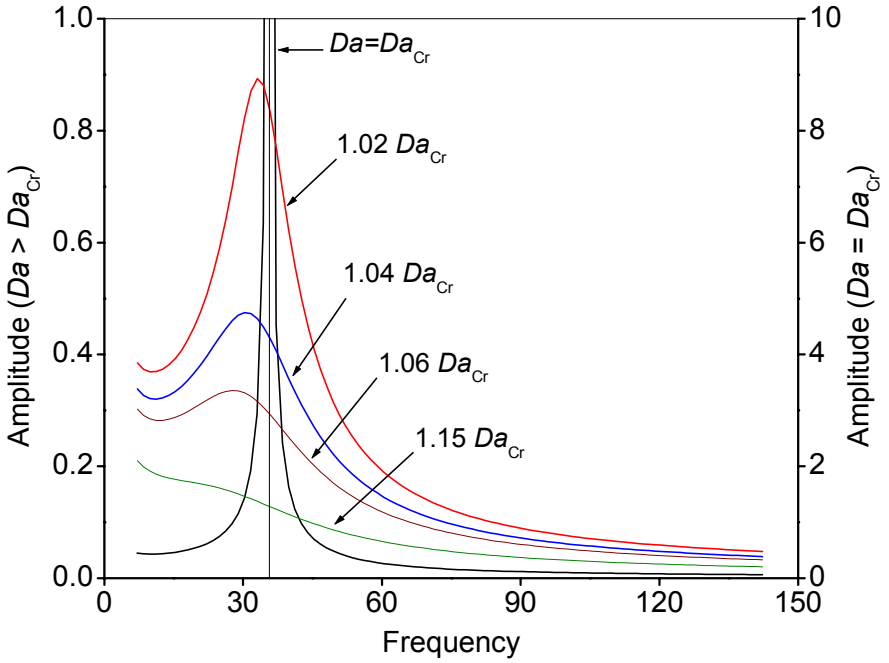

Figure 3.1. Amplitude of u_p^+ versus forced frequency c for different values of Da (with $Le_F = 2$, $Le_O = 2$, $\phi = 1$ and $\Delta T = 0$).

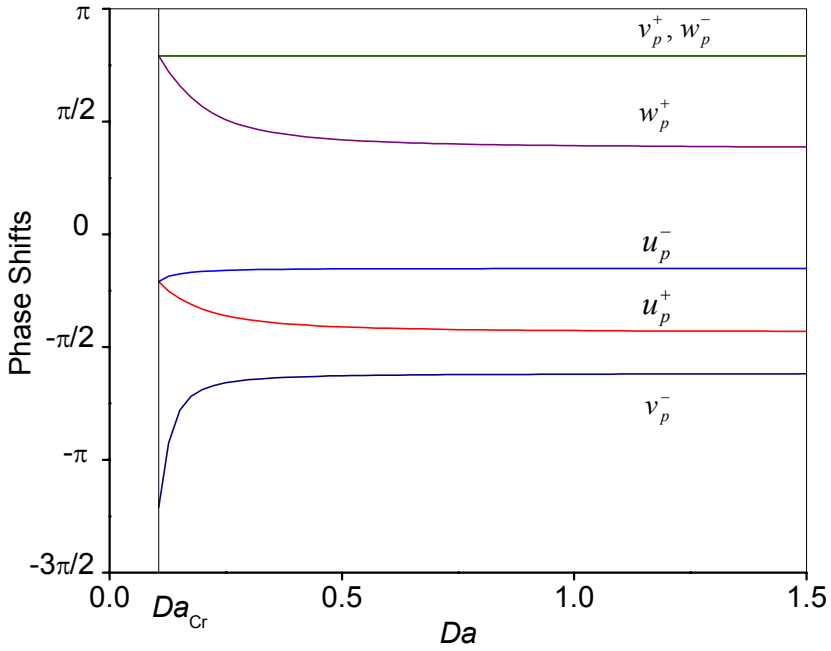

Figure 3.2. Phase shifts of u_p^+, u_p^-, v_p^+, v_p^- w_p^+ and w_p^- versus *Da* with $c = c_0$.

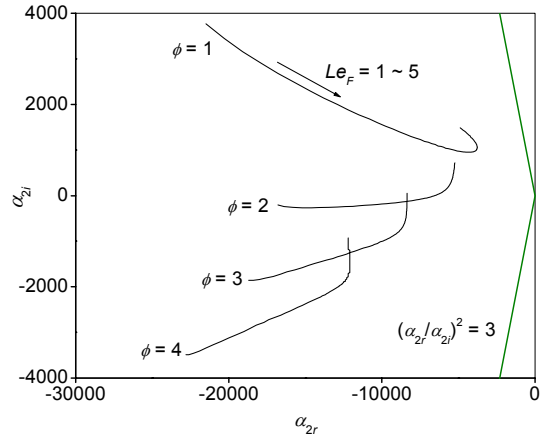

(a)

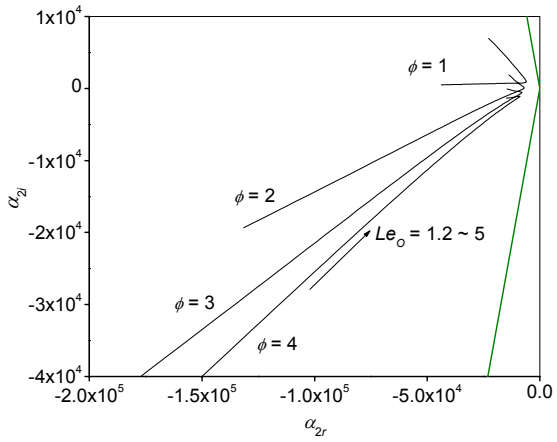

(b)

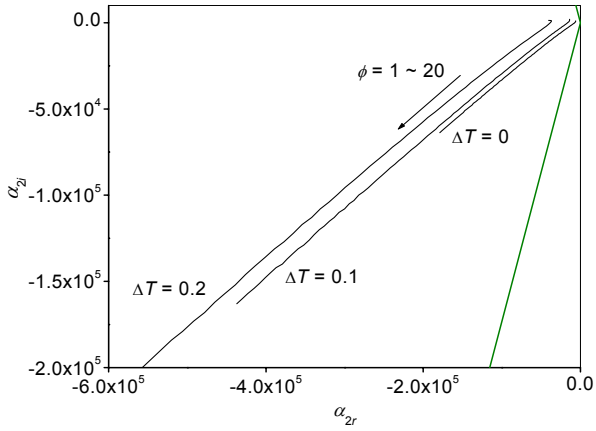

(c)

Figure 3.3. Variations of α_2 (a) with Le_F for different ϕ with $Le_O = 2$ and $\Delta T = 0$, (b) with Le_O for different ϕ with $Le_F = 2$ and $\Delta T = 0$, and (c) with ϕ for different ΔT with $Le_F = Le_O = 2$.

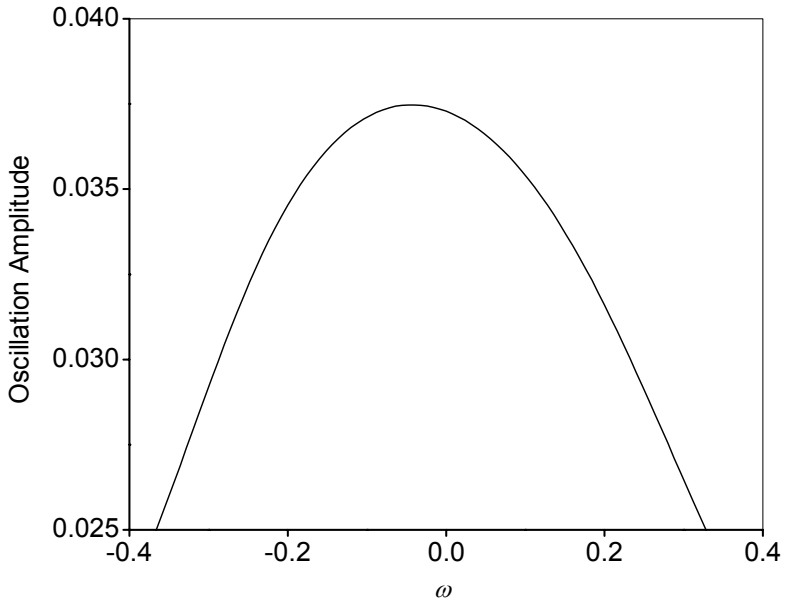

Figure 3.4. Variation of oscillation amplitude R with the normalized imposed frequency for $Da = Da_{\mathrm{Cr}}$ (with $Le_F = 2$, $Le_O = 2$, $\phi = 1$ and $\Delta T = 0$).

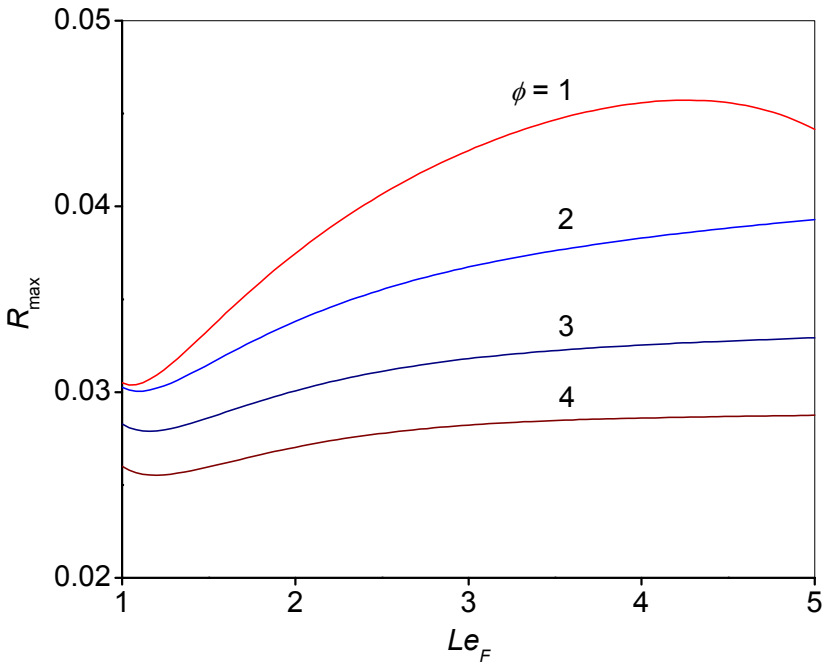

Figure 3.5. Variations of the maximum oscillation amplitude R_{max} with Le_F for different ϕ (with $Le_O = 2$ and $\Delta T = 0$)

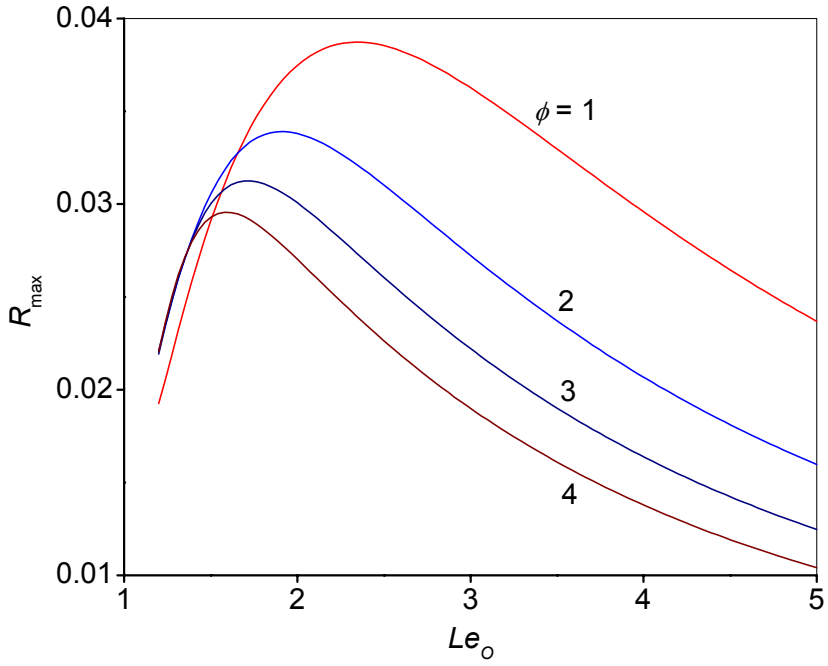

Figure 3.6. Variations of the maximum oscillation amplitude R_{max} with Le_O for different ϕ (with $Le_F = 2$ and $\Delta T = 0$).

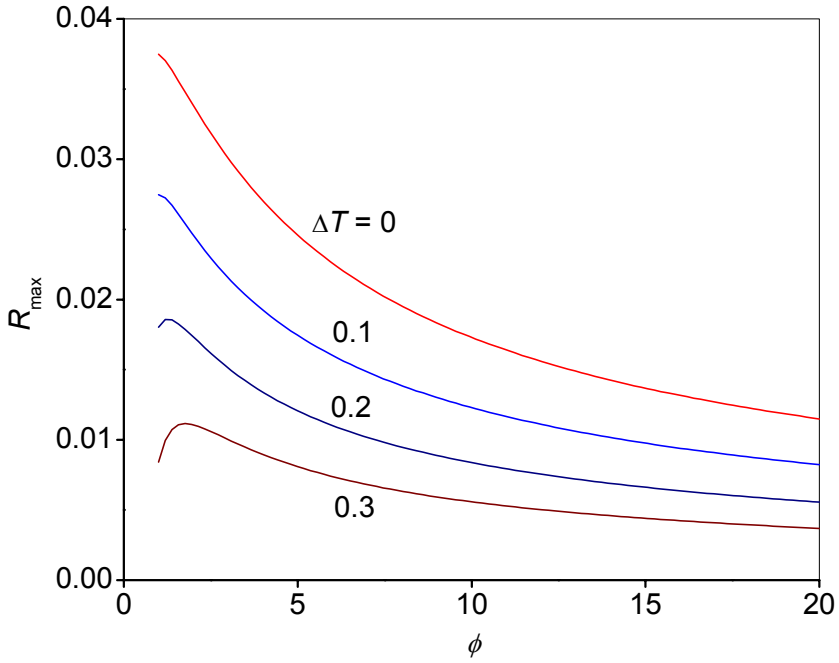

Figure 3.7. Variations of the maximum oscillation amplitude R_{max} with ϕ for different ΔT (with $Le_F = 2$ and $Le_O = 2$).

Chapter 4: Extinction of Radiative Diffusion Flames with Non-Unity Lewis numbers

4.1. Background

In this chapter, we carry out a systematic analysis for the structure and dual extinction limits of counterflow diffusion flames with flame radiation and non-unity Lewis numbers of the fuel and oxidant. This problem has been previously studied in a few analyses. Specifically, Sohrab *et al.* [1] proposed a multiscale asymptotic theory for the analysis of radiative flames by recognizing that while radiation is a temperature-sensitive process, it is nevertheless less sensitive than that of chemical reaction. Consequently, radiative loss is operative within a thin, $O(\delta)$, zone that sandwiches the $O(\varepsilon)$ reaction zone, but is in turn embedded within the much thicker $O(1)$ outer diffusive-convective zone, where ε is the reciprocal of the Zeldovich number, and δ satisfies $\varepsilon << \delta << 1$. Chao *et al.* [2] first successfully demonstrated, via the multi-scale asymptotic theory of Sohrab *et al.* [1], the existence of dual extinction states for droplet combustion with flame radiation. The analysis further showed that extinction for both limits, namely the kinetic and radiative extinction limits, is governed by Liñán's extinction criterion [3] as the consequence of excessive reactant leakage. Subsequently, this multi-scale asymptotics was employed by Oh *et al.* [4] for the diffusion flame stabilized on a condensed fuel with both flame and surface radiation, and by Liu *et al.* [5] for the counterflow diffusion flame with flame radiation and near unity reactant Lewis numbers. Specifically, Liu *et al.* [5] showed that

larger Lewis numbers lead to smaller flammable range of Damköhler number and smaller Lewis numbers increase this flammable range. Experimentally, the existence of the dual extinction limits was observed by Maruta *et al.* [6] in the counterflow diffusion flame of methane and air with flame radiation under microgravity.

These analyses, however, missed considering the excess/deficiency of the total enthalpy, i.e. excess enthalpy, in the reaction zone. Its importance was recognized by Kim & Williams [7] in their study of counterflow diffusion flame with non-unity Lewis number, *Le*. The excess enthalpy arises from the non-conservative nature of the total enthalpy, due to the imbalance of thermal and mass diffusion as the reactants leak through the flame as a result of finite-rate chemistry. It was shown that, although the amount of the excess enthalpy is small, typically of $O(\varepsilon)$, it can lead to $O(1)$ changes in the reaction rate. Furthermore, without considering the excess enthalpy, the dependence of *Da* on the reduced Damköhler number, Δ, is linear [3] so that the minimum of *Da* directly corresponds to the minimum of Δ, Δ_c. The physical extinction limit can be consequently determined from the reaction-sheet solution using Liñán's formula [3]. However, with the consideration of excess enthalpy, this dependence becomes nonlinear such that Δ_c does not necessarily correspond to the minimum of *Da*, and as such does not correctly identify the extinction condition. Recognizing that in addition to nonequidiffusion, which is the cause of excess enthalpy in the analysis of Kim & Williams [7], radiative loss from flames is the other major source of enthalpy loss in flames, overlooking the excess enthalpy is expected to produce $O(1)$ error on the radiative extinction limit, at which radiative loss is significant. Furthermore, previous analyses [1, 2, 4, 5] did not consider adequately the effect of nonequidiffusion. Since

extinction can be considered to be primarily attributed to the excessive heat loss from the reaction zone, which could be achieved through both conduction and radiation, it is necessary to consider the effects of non-unity *Le* and radiative loss at the same time. Although Liu *et al.* [5] considered non-unity *Le* with $O(\varepsilon)$ deviation from unity, such small deviation cannot describe all the *Le* dependency of the dual extinction limits, as will be shown later.

In view of the above considerations, one of the primary objectives of this chapter is to perform a rigorous multi-scale asymptotic analysis and develop a model for distinct and general Lewis numbers of fuel and oxidant, Le_F and Le_O, and with the proper consideration of excess enthalpy. This formulation is then applied to study the dual extinction limits of the radiative counterflow diffusion flames with non-unity Lewis numbers. It should be mentioned that Mills & Matalon [8] studied the extinction of burner-generated radiative spherical diffusion flames with non-unity Le_F and Le_O. However, the radiative loss was assumed to be an $O(\varepsilon)$ quantity and occurs within a zone of $O(1)$ thickness between the burner surface and flame, whose location and thickness are arbitrary given. Thus this analysis is based on different assumptions from the current study, in which radiative loss occurs within the radiation zone of $O(\delta)$ thickness determined from the temperature sensitivity of radiation, and hence has different scope of application. Furthermore, Mills & Matalon [8] found that the Lewis numbers of fuel and oxidant have significant effect on extinction limits, and steady burning is not possible when they are sufficiently large. This substantiates the need to conduct a rigorous extinction analysis for Lewis numbers sufficiently different from unity.

We further note that since the formulation developed in the current study is of a general nature, it can be applied to other phenomena affected by simultaneous radiative loss and mixture nonequidiffusion, such as the thermal-diffusive instability of radiation-affected diffusion flames. This possible extension will be subsequently discussed.

4.2. Formulation

4.2.1. Governing Equations

Figure 4.1 shows the counterflow configuration considered in this study, with the fuel and oxidant streams approaching from the left- (-∞) and right-hand (∞) sides respectively. Assuming constant physical and chemical properties of the reactants, constant density, one-step irreversible chemical reaction, and optically thin approximation for the radiative loss, the appropriate nondimensional governing equations can be written as

$$\frac{\partial T}{\partial t} - x\frac{\partial T}{\partial x} - \frac{\partial^2 T}{\partial x^2} = \omega - q_R \tag{4.1}$$

$$\frac{\partial Y_F}{\partial t} - x\frac{\partial Y_F}{\partial x} - Le_F^{-1}\frac{\partial^2 Y_F}{\partial x^2} = -\omega \tag{4.2}$$

$$\frac{\partial Y_O}{\partial t} - x\frac{\partial Y_O}{\partial x} - Le_O^{-1}\frac{\partial^2 Y_O}{\partial x^2} = -\omega \tag{4.3}$$

with the boundary conditions

$$\begin{aligned} &T = T_{-\infty}, \quad Y_F = Y_{F,-\infty}, \quad Y_O = 0 \quad \text{as} \quad x \to -\infty \\ &T = T_{\infty}, \quad Y_F = 0, \qquad Y_O = Y_{O,\infty} \quad \text{as} \quad x \to \infty \end{aligned} \tag{4.4}$$

where $\omega = Da_C Y_F Y_O \exp(-T_a/T)$ is the chemical reaction rate, $q_R = 4\sigma\kappa q^3 T^4/(\rho c_p^4 k)$ the rate of radiative heat loss, $Da_C = B_K \rho \tilde{Y}_{F,-\infty} \nu_O/(W_F k)$ the collision Damköhler number,

and T_a, k, σ, κ, q, ρ, c_p, B_K, respectively denote the activation temperature, stretch rate of the flow, Stefan-Boltzmann constant (1.36×10^{-11} kcal/m^2-sec-K^4), Planck's mean absorption coefficient, heat of combustion per unit mass of fuel supplied, density, specific heat, and pre-exponential factor for the reaction rate. The nondimensional T and Y_i are defined as

$$T = \frac{\widetilde{T}}{(q/c_p)},\ Y_F = \widetilde{Y}_F,\ Y_O = \widetilde{Y}_O / \nu$$

where $\nu = \nu_O W_O / \nu_F W_F$ is the stoichiometric mass ratio of the oxidant to the fuel and the over-tilde "~" designates the unscaled T and Y_i for differentiation with their nondimensional counterparts.

With the assumption of large activation energy, chemical reaction is confined within a thin zone of $O(\varepsilon)$ thickness, where $\varepsilon = T_f^2 / T_a$ and T_f is the flame temperature. Due to the temperature sensitive nature of radiation, radiative loss is assumed to be confined within a radiation zone of $O(\delta)$ thickness, with the reaction zone embedded within it, as shown by the flame structure in Fig. 4.1. Further recognizing that the diffusive-convective zone external to the radiation zone is of $O(1)$ thickness, we seek solution for the flame structure satisfying the relation $\varepsilon << \delta < 1$. Following Sohrab *et al.* [1], the rate of radiative loss, q_R, is approximated by an Arrhenius-type function

$$q_R = q_{Rf} \exp\left(\frac{T - T_f}{\delta T_f}\right) \tag{4.5}$$

where $q_{Rf} = 4\sigma\kappa q^3 T_f^4 / (\rho c_p^4 k)$ and $\delta = d(\ln T)/d(\ln q_R)$. With the assumptions of constant density and properties made in this study, δ=0.25.

4.2.2. Asymptotic Expansions

Following Chao *et al.* [2], the temperature T in the diffusive-convective, radiation, and reaction zones are respectively expanded in terms of ε and δ as

$$T_{\text{out}}^{\pm} \sim T_0^{\pm}(x,t) + \varepsilon T_1^{\pm}(x,t) + \delta\left[T_2^{\pm}(x,t) + \varepsilon T_3^{\pm}(x,t)\right] + O\left(\delta^2\right) \tag{4.6}$$

$$T_{\text{R}}^{\pm} \sim T_f + \varepsilon\Theta_1^{\pm}(\zeta) + \delta\left[\Theta_2^{\pm}(\zeta) + \varepsilon\Theta_3^{\pm}(\zeta)\right] + O(\delta^2) \tag{4.7}$$

$$T_{\text{in}} \sim T_f + \varepsilon\tau_1(\eta) + \varepsilon^2\tau_2(\eta) + \text{O}(\varepsilon^3) \tag{4.8}$$

where $\zeta = (x - x_f)/\delta$ and $\eta = (x - x_f)/\varepsilon$ are the stretched spatial coordinates in the radiation zone and reaction zone, respectively, and x_f is the flame-sheet location. The superscripts "+" and "–" denote solutions in the oxidant and fuel sides of the flame, respectively. The reason for expanding T_{in} only in terms of ε is that the reaction zone is very thin so that radiative loss from it can be assumed to be negligible.

Because Y_F and Y_O are not directly affected by radiative loss, their analyses only need to be conducted in two zones, namely the reaction zone and the diffusive-convective zone. Thus, they can be respectively expanded as

$$Y_{i,\text{out}}^{\pm} \sim Y_{i,0}^{\pm}(x,t) + \varepsilon Y_{i,1}^{\pm}(x,t) + \varepsilon^2 Y_{i,2}^{\pm}(x,t) + \text{O}(\varepsilon^3) \tag{4.9}$$

$$Y_{i,\text{in}} \sim \varepsilon y_{i,1}(\eta) + \varepsilon^2 y_{i,2}(\eta) + \text{O}(\varepsilon^3) \tag{4.10}$$

where i=F, O. We note that unlike the analysis of Chao *et al.* [2], the outer expansions for Y_F and Y_O do not have the $O(\delta)$ terms. This is because these terms do not have the corresponding matching terms in the reaction zone and because of their homogeneous boundary conditions at $x \to \pm\infty$. Consequently, it can be shown that they are identically zero throughout the diffusive-convective zone.

The above expansions for T are subject to the matching conditions between the radiation and reaction zones:

$$\left.\begin{aligned} &\Theta_1^{\pm}(0) \sim \tau_1\big|_{\eta\to\pm\infty}, \quad && \frac{d\Theta_1^{\pm}(0)}{d\zeta} \sim 0 \\ &\Theta_2^{\pm}(0) \sim 0, && \frac{d\Theta_2^{\pm}(0)}{d\zeta} \sim \frac{d\tau_1}{d\eta}\bigg|_{\eta\to\pm\infty} \\ &\Theta_3^{\pm}(0) \sim 0, && \frac{d\Theta_3^{\pm}(0)}{d\zeta} \sim \frac{d\tau_2}{d\eta}\bigg|_{\eta\to\pm\infty} \end{aligned}\right\} \tag{4.11}$$

and the matching conditions between the diffusive-convective and radiation zones:

$$\left.\begin{aligned} &T_f \sim T_0^{\pm}(x_f) \\ &\Theta_1^{\pm}\big|_{\zeta\to\pm\infty} \sim T_1^{\pm}(x_f), \quad && \frac{d\Theta_1^{\pm}}{d\zeta}\bigg|_{\zeta\to\pm\infty} \sim 0 \\ &\Theta_2^{\pm}\big|_{\zeta\to\pm\infty} \sim -\infty, && \frac{d\Theta_2^{\pm}}{d\zeta}\bigg|_{\zeta\to\pm\infty} \sim \frac{\partial T_0^{\pm}(x_f)}{\partial x} \\ &\Theta_3^{\pm}\big|_{\zeta\to\pm\infty} \sim -\infty, && \frac{d\Theta_3^{\pm}}{d\zeta}\bigg|_{\zeta\to\pm\infty} \sim \frac{\partial T_1^{\pm}(x_f)}{\partial x} \end{aligned}\right\} \tag{4.12}$$

The expansions for Y_F and Y_O are only subject to the matching conditions between the diffusive-convective and reaction zones:

$$\left.\begin{aligned} &0 \sim Y_{i,0}^{\pm}(x_f), \quad y_{i,1}\big|_{\eta\to\pm\infty} \sim \frac{\partial Y_{i,0}^{\pm}(x_f)}{\partial x}\eta + Y_{i,1}^{\pm}(x_f) \\ &\frac{dy_{i,1}}{d\eta}\bigg|_{\eta\to\pm\infty} \sim \frac{\partial Y_{i,0}^{\pm}(x_f)}{\partial x}, \quad \frac{dy_{i,2}}{d\eta}\bigg|_{\eta\to\pm\infty} \sim \frac{\partial^2 Y_{i,0}^{\pm}(x_f)}{\partial x^2}\eta + \frac{\partial Y_{i,1}^{\pm}(x_f)}{\partial x} \end{aligned}\right\} \tag{4.13}$$

4.2.3. Jump Relations and Reactant Leakages across the Reaction Zone

We aim to derive the jump relations and the reactant leakages that serve as the inner boundary conditions for the outer solutions in the diffusive-convective zone.

The matching conditions for the $O(1)$ outer solutions in Eqs. (4.12) and (4.13) yield the jump relations

$$[T_0]=[Y_{F,0}]=[Y_{O,0}]=Y_{F,0}^{+}(0)=Y_{O,0}^{-}(0)=0 \tag{4.14}$$

where we have adopted the notation $[T_0]=T_0^{+}(x_f)-T_0^{-}(x_f)$. Additional jump relations and reactant leakages are to be derived through the asymptotic analysis of the reaction zone. Substituting the inner expansions (4.8) and (4.10) and the stretched coordinate η into the governing equations (4.1)-(4.3) yields, to $O(\varepsilon)$,

$$d^2\tau_1/d\eta^2=-Day_{F,1}y_{O,1}e^{\tau_1} \tag{4.15}$$

$$d^2(\tau_1+y_{i,1}/Le_i)/d\eta^2=0, \quad i=F, O \tag{4.16}$$

and to $O(\varepsilon^2)$,

$$d^2(\tau_2+y_{i,2}/Le_i)/d\eta^2=0, \quad i=F, O \tag{4.17}$$

where $Da=\varepsilon^3 Da_C\exp(-T_a/T_f)$ is the reaction Damköhler number. Integrating Eq. (4.16) twice and applying the relevant matching conditions, (4.11) and (4.13), for τ_1, $y_{i,1}$, $d\tau_1/d\eta$ and $dy_{i,1}/d\eta$ yield

$$\tau_1+\frac{1}{Le_F}y_{F,1}=\frac{d\Theta_2^{+}(0)}{d\zeta}\eta+\Theta_1^{+}(0)+\frac{1}{Le_F}Y_{F,1}^{+} \tag{4.18}$$

$$\tau_1+\frac{1}{Le_O}y_{O,1}=\frac{d\Theta_2^{-}(0)}{d\zeta}\eta+\Theta_1^{-}(0)+\frac{1}{Le_O}Y_{O,1}^{-} \tag{4.19}$$

and the jump relations

$$\frac{d\Theta_2^{+}(0)}{d\zeta}-\frac{d\Theta_2^{-}(0)}{d\zeta}=-Le_F^{-1}\left[\frac{\partial Y_{F,0}}{\partial x}\right]=-Le_O^{-1}\left[\frac{\partial Y_{O,0}}{\partial x}\right] \tag{4.20}$$

$$\Theta_1^{+}(0)-\Theta_1^{-}(0)=-Le_F^{-1}[Y_{F,1}]=-Le_O^{-1}[Y_{O,1}] \tag{4.21}$$

Integrating Eq. (4.17) once and applying the relevant matching conditions, (4.11) and (4.13), for $d\tau_2/d\eta$ and $dy_{i,2}/d\eta$ yield the jump relation

$$\left(x_f\Theta_1^+(0)+\frac{d\Theta_3^+(0)}{d\zeta}\right)-\left(x_f\Theta_1^-(0)+\frac{d\Theta_3^-(0)}{d\zeta}\right)=-\left[x_fY_{F,1}+Le_F^{-1}\frac{\partial Y_{F,1}}{\partial x}\right]=-\left[x_fY_{O,1}+Le_O^{-1}\frac{\partial Y_{O,1}}{\partial x}\right] \tag{4.22}$$

So far we have derived the jump relations (4.14) and (4.20)-(4.22) across the reaction zone. However, for the current multi-scale analysis, the reaction zone is sandwiched in the radiation zone so that the temperature terms in these jump relations are expressed by the expansion terms in the radiation zone. Since we aim to derive the jump relations that are to be used as the inner boundary conditions of the outer expansions, the terms, $\Theta_1^{\pm}(0)$, $d\Theta_2^{\pm}(0)/d\zeta$, and $d\Theta_3^{\pm}(0)/d\zeta$ in Eqs. (4.20)-(4.22) need to be replaced by the outer expansion terms. This can be realized through integrating the structure equation of the radiation zone and applying the matching conditions between the radiation zone and the diffusive-convective zone. Substituting Eq. (4.7) into the chemically frozen form of Eq. (4.1) yields

$$d^2\Theta_2^{\pm}/d\zeta^2 = Ra\exp(\Theta_2^{\pm}/T_f) \tag{4.23}$$

$$d^2\Theta_1^{\pm}/d\zeta^2 = Ra\Theta_1^{\pm}\exp(\Theta_2^{\pm}/T_f)/T_f \tag{4.24}$$

$$d^2\Theta_3^{\pm}/d\zeta^2 + x_f\, d\Theta_1^{\pm}/d\zeta = Ra\Theta_3^{\pm}\exp(\Theta_2^{\pm}/T_f)/T_f \tag{4.25}$$

where $Ra = \delta q_{Rf}$. Integrating Eqs. (4.23)-(4.25) and applying the relevant matching conditions (see Appendix) yield

$$\frac{d\Theta_2^{\pm}(0)}{d\zeta} = A^{\pm}\frac{\partial T_0^{\pm}(x_f)}{\partial x} \tag{4.26}$$

$$\Theta_1^{\pm}(0) = A^{\pm}T_1^{\pm}(x_f) \tag{4.27}$$

$$\frac{d\Theta_3^{\pm}(0)}{d\zeta} \sim \frac{1}{2}\left(A^{\pm} - \frac{1}{A^{\pm}}\right)T_1^{\pm}(x_f) + \frac{1}{A^{\pm}}\frac{\partial T_1^{\pm}(x_f)}{\partial x} \tag{4.28}$$

where $A^{\pm} = \sqrt{1 + 2RaT_f \Big/ \left(\partial T_0^{\pm}(x_f)/\partial x\right)^2}$. Thus, the jump relations in terms of the outer solutions can be obtained by substituting Eqs. (4.26)-(4.28) into Eqs. (4.20)-(4.22), respectively,

$$\left[A\frac{\partial T_0}{\partial x}\right] = -Le_F^{-1}\left[\frac{\partial Y_{F,0}}{\partial x}\right] = -Le_O^{-1}\left[\frac{\partial Y_{O,0}}{\partial x}\right] \tag{4.29}$$

$$\left[AT_1\right] = -Le_F^{-1}\left[Y_{F,1}\right] = -Le_O^{-1}\left[Y_{O,1}\right] \tag{4.30}$$

$$\left[Bx_f T_1 + \frac{1}{A}\frac{\partial T_1}{\partial x}\right] = -\left[x_f Y_{F,1} + Le_F^{-1}\frac{\partial Y_{F,1}}{\partial x}\right] = -\left[x_f Y_{O,1} + Le_O^{-1}\frac{\partial Y_{O,1}}{\partial x}\right] \tag{4.31}$$

where $B^{\pm} = [(A^{\pm})^2 + 1]/2A^{\pm}$ and we have used the notation $\left[AT_1\right] = A^{+}T_1^{+}(x_f) - A^{-}T_1^{-}(x_f)$.

The jump relations (4.14) and (4.29) provide adequate inner boundary conditions for the $O(1)$ outer solutions. However, two additional conditions for the $O(\varepsilon)$ outer solutions are required to close the problem. They can be supplied by the amount of leakages of the fuel and oxidant through the reaction zone, and are given as

$$Y_{F,1}^{+}(x_f) = Le_F S_F(\gamma, \Delta), \qquad Y_{O,1}^{-}(x_f) = Le_O S_O(\gamma, \Delta) \tag{4.32}$$

by transforming the energy equation (4.15) into the Liñán's canonical form, where,

$$\gamma = -\left(A^{+}\frac{\partial T_0^{+}(x_f)}{\partial x} + A^{-}\frac{\partial T_0^{-}(x_f)}{\partial x}\right)\left[A\frac{\partial T_0}{\partial x}\right]^{-1} \tag{4.33}$$

and

$$\Delta = 4Le_F Le_O Da\left[A\frac{\partial T_0}{\partial x}\right]^{-2}\exp\left(\frac{1+\gamma}{2}h_O + \frac{1-\gamma}{2}h_F\right) \tag{4.34}$$

is the reduced Damköhler number, S_F and S_O are the leakage functions of the fuel and oxidant, respectively, and

$$\begin{aligned} h_F &= A^+ T_1^+(x_f) + Le_F^{-1} Y_{F,1}^+(x_f) \\ h_O &= A^- T_1^-(x_f) + Le_O^{-1} Y_{O,1}^-(x_f) \end{aligned} \tag{4.35}$$

are the excess/deficiency in the fuel and oxidant enthalpies, respectively, evaluated at the reaction sheet. This process is standard [3, 9] and is not repeated here.

The leakage functions S_F and S_O are obtained from solving the canonical form the structure equation and hence can take advantage of previous results [9, 10]. As we have discussed in Chapter 2, they are only dependent on Δ and γ, and their solutions exist only when $\Delta \geq \Delta_c$, where the critical value Δ_c is given by the expression of Liñán [3], shown previously, as

$$\Delta_c = e\left[(1-|\gamma|) - (1-|\gamma|)^2 + 0.26(1-|\gamma|)^3 + 0.055(1-|\gamma|)^4\right] \tag{4.36}$$

The term $h_f = (1+\gamma)h_O/2 + (1-\gamma)h_F/2$ in Eq. (4.34) represents the excess/deficiency of the total enthalpy in the reaction zone. This is the term that was overlooked in previous analyses [1, 2, 4, 5]. Without considering it, Δ depends linearly on Da so that its minimum value, Da_E, coincides with that of Δ, Δ_c. Because γ is determined from the leading order solutions, the extinction condition, represented by Da_E, can be accordingly determined directly from Δ_c. However, when the excess enthalpy is taken into consideration, Eq. (4.34) becomes a nonlinear relation between Δ and Da because h_f depends on the reactant leakages S_F and S_O, which, in turn, depend on Δ. Consequently, Δ_c does not correctly identify the extinction condition, Da_E, and the determination of Da from given Δ requires the $O(\varepsilon)$ outer solutions, which substantially complicates the solution procedure.

4.2.4. Summary of the Model

So far we have derived the jump relations in terms of the outer solutions and the reactant leakages across the reaction zone, which provide sufficient inner boundary conditions to fully determine the $O(1)$ and $O(\varepsilon)$ outer solutions and the flame sheet location. They are summarized as follows:

To $O(1)$:

$$[T_0]=[Y_{F,0}]=[Y_{O,0}]=Y_{F,0}^{+}(0)=Y_{O,0}^{-}(0)=0 \tag{4.37}$$

$$\left[A\frac{\partial T_0}{\partial x}\right]=-Le_F^{-1}\left[\frac{\partial Y_{F,0}}{\partial x}\right]=-Le_O^{-1}\left[\frac{\partial Y_{O,0}}{\partial x}\right] \tag{4.38}$$

To $O(\varepsilon)$:

$$[AT_1]=-Le_F^{-1}[Y_{F,1}]=-Le_O^{-1}[Y_{O,1}] \tag{4.39}$$

$$\left[Bx_fT_1+\frac{1}{A}\frac{\partial T_1}{\partial x}\right]=-\left[x_fY_{F,1}+Le_F^{-1}\frac{\partial Y_{F,1}}{\partial x}\right]=-\left[x_fY_{O,1}+Le_O^{-1}\frac{\partial Y_{O,1}}{\partial x}\right] \tag{4.40}$$

$$Y_{F,1}^{+}(x_f)=Le_FS_F(\gamma,\Delta),\quad Y_{O,1}^{-}(x_f)=Le_OS_O(\gamma,\Delta) \tag{4.41}$$

It is noted that we have not derived the jump relations for the $O(\delta)$ expansion terms of T. This is because the matching conditions $\Theta_2^{\pm}(0)\sim 0$ imply that the $O(\delta)$ terms can be solved separately on either side of the reaction zone.

4.2.5. Solutions of Counterflow Diffusion Flame

We now apply the model Eqs. (4.37)-(4.41) to the counterflow diffusion flame with non-unity Lewis numbers and radiative loss. The $O(1)$ outer solutions subject to the boundary condition (4.4) and jump relations (4.37) and (4.38) can be solved as

$$T_0(x)=\begin{cases}T_{-\infty}+(T_f-T_{-\infty})I^-(x;1)\big/I^-(x_f;1), & x<x_f\\ T_{\infty}+(T_f-T_{\infty})I^+(x;1)\big/I^+(x_f;1), & x>x_f\end{cases} \tag{4.42}$$

$$Y_{F,0}(x)=\begin{cases}Y_{F,-\infty}\left[1-I^-(x;Le_F)\big/I^-(x_f;Le_F)\right], & x<x_f\\ 0, & x>x_f\end{cases} \tag{4.43}$$

$$Y_{O,0}(x)=\begin{cases}0, & x<x_f\\ Y_{O,\infty}\left[1-I^+(x;Le_O)\big/I^+(x_f;Le_O)\right], & x>x_f\end{cases} \tag{4.44}$$

where

$$I^{\pm}(x;L)=\sqrt{\pi/2L}\left[\mp 1+erf\left(\sqrt{L/2}x\right)\right]$$

and the flame location x_f and temperature T_f can be respectively determined from the jump relation (4.38) implicitly as

$$\frac{Le_F^{-1}Y_{F,-\infty}\exp\left(-Le_Fx_f^2/2\right)}{I^-(x_f;Le_F)}=-\frac{Le_O^{-1}Y_{O,\infty}\exp\left(-Le_Ox_f^2/2\right)}{I^+(x_f;Le_O)} \tag{4.45}$$

$$\sqrt{\left(\frac{\partial T_0^+(x_f)}{\partial x}\right)^2+2RaT_f}+\sqrt{\left(\frac{\partial T_0^-(x_f)}{\partial x}\right)^2+2RaT_f}=\frac{Le_F^{-1}Y_{F,-\infty}\exp\left(-Le_Fx_f^2/2\right)}{I^-(x_f;Le_F)} \tag{4.46}$$

Equation (4.46) indicates that the chemical heat release is conducted away from the flame to both sides. It is seen that in additional to being used to heat up the reactants, the heat release now needs to compensate for the radiative loss through the term $2RaT_f$ in Eq. (4.46). However, the temperature gradient decreases at the same time due to the reduction of the flame temperature through radiative loss. Moreover, it is noted that the total heat release is controlled by the reactant consumption and hence is fixed. In most cases, these two opposite effects on heat transfer by radiative loss are not equal. Therefore, the overall outcome of radiative loss is to redistribute the proportions of heat transfer from the flame

to both sides and as such it plays the similar role as varying the thermal diffusivities of the reactants.

Applying the homogeneous boundary conditions at $x \to \pm\infty$ and the jump and leakage conditions (4.39)-(4.41), the $O(\varepsilon)$ outer solutions, $T_1^{\pm}$, $Y_{F,1}^{\pm}$ and $Y_{O,1}^{\pm}$, can be fully determined. Here we only show them in the form of the excess enthalpies, h_F and h_O, because they are the reason the $O(\varepsilon)$ outer solutions are required. Thus we have

$$h_F = C_{F,1} S_F(\gamma,\Delta) + C_{O,1} S_O(\gamma,\Delta)$$
$$h_O = C_{F,2} S_F(\gamma,\Delta) + C_{O,2} S_O(\gamma,\Delta)$$

and the total excess enthalpy is then given as

$$h_f = C_F S_F(\gamma,\Delta) + C_O S_O(\gamma,\Delta)$$

where

$$C_i = (1-\gamma)C_{i,1}/2 + (1+\gamma)C_{i,2}/2, \quad i = F, O$$

$$C_{F,1} = \left(\frac{M_T^+}{A^+} - \frac{M_T^-}{A^-}\right)^{-1} \left\{ -\left(Le_F M_F^+ - \frac{M_T^+}{A^+}\right) + \frac{\left(Le_F^{-1}\frac{M_T^-}{A^-} - M_F^-\right)\left(M_O^+ - \frac{Le_F}{Le_O}M_F^+\right)}{-Le_F^{-1}M_O^+ + Le_O^{-1}M_F^-} \right\}$$

$$C_{O,1} = \left(\frac{M_T^+}{A^+} - \frac{M_T^-}{A^-}\right)^{-1} \left\{ \frac{\left(Le_F^{-1}\frac{M_T^-}{A^-} - M_F^-\right)\left(M_O^+ - M_O^-\right)}{-Le_F^{-1}M_O^+ + Le_O^{-1}M_F^-} \right\}$$

$$C_{F,2} = \left(\frac{M_T^+}{A^+} - \frac{M_T^-}{A^-}\right)^{-1} \left\{ -\left(Le_F M_F^+ - \frac{M_T^+}{A^+}\right) + \frac{\left(Le_F^{-1}\frac{M_T^+}{A^+} - M_F^-\right)\left(M_O^+ - \frac{Le_F}{Le_O}M_F^+\right)}{-Le_F^{-1}M_O^+ + Le_O^{-1}M_F^-} \right\}$$

$$C_{O,2}=\left(\frac{M_T^+}{A^+}-\frac{M_T^-}{A^-}\right)^{-1}\left\{\left(\frac{M_T^+}{A^+}-\frac{M_T^-}{A^-}\right)+\frac{\left(Le_F^{-1}\dfrac{M_T^+}{A^+}-M_F^-\right)\left(M_O^+-M_O^-\right)}{-Le_F^{-1}M_O^++Le_O^{-1}M_F^-}\right\}$$

and

$$M_T^{\pm}=B^{\pm}x_f+\frac{1}{A^{\pm}}\frac{\exp\left(-x_f^2/2\right)}{I^{\pm}(x_f;1)}$$

$$M_i^{\pm}=x_f+Le_i^{-1}\frac{\exp\left(-Le_i x_f^2/2\right)}{I^{\pm}(x_f;Le_i)},\quad i=F,\ O$$

We note that the total excess enthalpy h_f is a linear combination of the reactant leakages, S_F and S_O, while γ and the coefficients C_F and C_O are only dependent on the leading order solutions and radiative loss. Thus, for a fixed system with given radiative loss, the total enthalpy h_f is solely determined by the value of Δ.

4.2.6. Extinction Analysis

Since the quantifying parameters ε, *Ra* and *Da* are functions of the flame temperature, T_f, which varies with radiative loss, it is necessary to rescale all the parameters to a fixed, absolute reference state [2]. Using the adiabatic flame temperature T_{ref} for $\widetilde{Y}_{F,-\infty}=1$, $\widetilde{Y}_{O,\infty}=0.23$ and $Le_F = Le_O = 1$ as the reference state, and denoting the associated quantities by the superscript "*", we have

$$Da^*=(T_{\text{ref}}^2/T_a)^3\,Da_C\exp\left(-T_a/T_{\text{ref}}\right)$$

$$Ra^*=4\delta\sigma\kappa q^3T_{\text{ref}}^4/(\rho c_p^4 k)$$

so that

$$Da = Da^* \left(T_f / T_{\text{ref}}\right)^6 \exp\left[T_a \left(1/T_{\text{ref}} - 1/T_f\right)\right]$$

$$Ra = Ra^* \left(T_f / T_{\text{ref}}\right)^4$$

and Eq. (4.34) becomes

$$\Delta e^{-h_f} = Da^* \left\{ 4 Le_F Le_O \left(\frac{T_f}{T_{\text{ref}}} \right)^6 \exp\left[T_a \left(\frac{1}{T_{\text{ref}}} - \frac{1}{T_f} \right) \right] \left[A \frac{\partial T_0}{\partial x} \right]^{-2} \right\} \tag{4.47}$$

The extinction Damköhler number Da_E^* corresponds to the minimum value of Da^*, i.e.

$$\partial S_F(\gamma, \Delta) / \partial Da^* \to \infty \tag{4.48}$$

We have known that for a fixed system with given Ra^*, all the terms in Eq. (4.47) other than Δ and Da^* can be determined. Thus, Eq. (4.47) gives a definite relation between Da^* and Δ. Substituting Eq. (4.47) into Eq. (4.48) yields the extinction condition

$$\left(\Delta \frac{\partial h_f}{\partial \Delta} \right)_{\text{ext}} - 1 = 0 \tag{4.49}$$

from which the reduced Damköhler number at extinction, Δ_{ext}, can be solved. Then the extinction Damköhler number Da_E^* can be solved by substituting Δ_{ext} into Eq. (4.47).

4.3. Results and Discussion

We use the CH_4/Air counterflow diffusion flame to demonstrate the dual extinction characteristics with the effects of radiative loss and non-unity Lewis numbers. The system parameters adopted are $\widetilde{T}_{-\infty} = \widetilde{T}_{\infty} = 300\text{K}$, $\widetilde{T}_a = 24{,}000\text{K}$, $c_p = 0.334$ kcal/Kg-K and $q = 11{,}990$ kcal/Kg. The boundary conditions for the fuel and oxidant fractions are fixed at $\widetilde{Y}_{F,-\infty} = 1$ and $\widetilde{Y}_{O,\infty} = 0.23$, respectively, throughout this study unless otherwise

specified. Thus, the initial mixture strength, defined as $\phi = \nu \widetilde{Y}_{F,-\infty} / \widetilde{Y}_{O,\infty}$, is 17.4 in the current study.

Figure 4.2 shows variations of the flame location, x_f, with the fuel and oxidant Lewis numbers, Le_F and Le_O, respectively. It is seen that the flame is always located at the oxidant side of the stagnation surface over the entire ranges of Le_F and Le_O, which is a consequence of the stoichiometric nature of diffusion flames. Furthermore, it is seen that with the decrease of Le_F (Le_O), the flame moves toward the oxidant (fuel) side and Le_F has a much stronger effect on the flame location than Le_O. This is because for the current problem the flame is located in the oxidant side of the stagnation surface. Thus, fuel diffusion has to overcome convection of the opposite direction to supply the fuel to the flame. Consequently, fuel diffusion plays a more important role than that of the oxidant such that variation of Le_F leads to a much larger shift of x_f.

Figure 4.3 shows variations of the coefficient of the fuel leakage in the total excess enthalpy, C_F, with Le_F and Le_O for different values of Ra^*, respectively. Here only the results for C_F are presented because the flame is located in the oxidant side of the stagnation surface for the current problem such that γ is sufficiently larger than zero and hence $S_F >> S_O$. It is seen that C_F decreases with increasing Le_F, Le_O and Ra^* and for $Le_F > 1$, $Le_O > 1$ and $Ra^* > 0$, C_F is always negative. Thus, the excess enthalpy is always negative under theses parameters. For flames with radiative loss, the only possibility for the excess enthalpy to be positive is that the Lewis numbers are sufficiently smaller than unity.

Figure 4.4 shows the fuel leakage S_F as functions of the reduced Damköhler number Δ (Fig. 4.4a) and Da^* (Fig. 4.4b) for $Le_F = Le_O = 1$ and different values of Ra^*. It

is seen that there exist minimum values for Δ and Da^*, Δ_c and Da_E^*, and there are two branches of solutions when $\Delta > \Delta_c$ and $Da^* > Da_E^*$, respectively. However, because of the nonlinear relation between Δ and Da^*, Δ_c does not coincide with Da_E^* except for the case of zero excess enthalpy when $Le_F = Le_O = 1$ and $Ra^* = 0$. It is noted that flame extinction corresponds to the minimum of Da^*, Da_E^*, which is a parameter that can be independently specified. However, it does not correspond to the minimum of Δ, Δ_c, which is not an independently specifiable parameter because it depends on the value of γ determined from the leading order solutions. As shown in Fig. 4.4b, the turning point Δ_c in the $S_F \sim \Delta$ plot, indicated by the "x" symbol, is located on the upper branch of the $S_F \sim Da^*$ plot. The extinction limit here, Da_E^*, indicated by the "♦" symbol, corresponds to the kinetic extinction limit at high stretch rates. Near this limit increasing Da^* leads to longer residence time and hence more complete burning and less reactant leakage. Thus, the lower branch is the physically realistic solution. Figure 4.4b also shows that the $S_F \sim Da^*$ curve shifts to the right with increasing Ra^*. This means that for larger Ra^* a higher Da^* is required for steady burning in order to compensate for the effect of radiative loss, and for a fixed Da^* the amount of fuel leakage S_F with larger Ra^* is more than that with smaller Ra^*. Consequently, the extinction limit, Da_E^*, increases with Ra^*.

To illustrate the effect of neglecting the excess enthalpy on the prediction of the extinction limit, the $S_F \sim Da^*$ curves for different Ra^* without considering the excess enthalpy are also plotted in Fig. 4.4b. It is observed that the fuel leakage at the same Da^* and the extinction Damköhler number, Da_E^*, are underestimated due to the omission of the excess enthalpy, and this underestimation becomes more significant with increasing

Ra^*. This is because the excess enthalpy is negative for the parameters used in this figure ($Le_F = Le_O = 1$ and $Ra^* > 0$) and therefore tends to weaken the flame. Thus omitting it would lead to flames that are more resistant to extinction, with smaller values of Da_E^*.

For a given Ra^*, the extinction Damköhler number, Da_E^*, can be solved from Eqs. (4.47) and (4.49). However, because both Ra^* and Da^* depend on the stretch rate k, the Da_E^* solved for a fixed Ra^*, such as those in Fig. 4.4b, is only relevant for studying the effects of varying the fuel/oxidant system for a counterflow of fixed stretch rate. On the other hand, an equally relevant question to ask is the effect of varying the stretch rate for a fixed fuel/oxidant system. Because of the inverse dependence of both Ra^* and Da^* on k, the relative effect of radiative heat loss can be evaluated by defining a parameter $\Gamma = Ra^*/Da^*$ [2], which represents the relative strength of the radiative loss to the chemical heat release. It depends only on the thermo-chemical parameters, but is independent of the stretch rate k. Thus, in additional to Eqs. (4.47) and (4.49), the extinction Damköhler numbers also need to satisfy $Ra^*/Da^* = \Gamma$ at the same time and hence can be obtained from the intersection points between the $Da_E^* \sim Ra^*$ curves and the $Da^* \sim Ra^*/\Gamma$ lines. Figure 4.5 shows the variation of Da_E^* with Ra^* for $Le_F = Le_O = 1$ and the $Da^* \sim Ra^*/\Gamma$ lines for different values of Γ. It is seen that for a fixed system with Γ smaller than the critical value $\Gamma_c \approx 0.298$, there are two intersection points and hence two extinction limits at different level of radiative loss. The one at smaller Ra^* leads to a smaller extinction Damköhler number, namely $Da_{E,K}^*$, and hence corresponds to the kinetic extinction limit, whereas the one at larger Ra^* corresponds to the radiative extinction limit occurring at a larger Da^*, namely $Da_{E,R}^*$. Thus, steady burning is only

possible within a limited range of Damköhler number, $Da^*_{E,K} < Da^* < Da^*_{E,R}$. Furthermore, it is seen that with increasing Γ the two extinction Damköhler numbers approach each other and there is no intersection point once Γ exceeds the critical value, Γ_c. This trend can be observed more clearly from the plot of the dual extinction Damköhler numbers versus Γ, shown in Fig. 4.6. It is seen that $Da^*_{E,R}$ decreases and $Da^*_{E,K}$ increases with increasing Γ, and the two branches of extinction Damköhler numbers ultimately merge at $\Gamma = \Gamma_c$ so that burning is not possible regardless of the stretch rate for $\Gamma > \Gamma_c$. Furthermore, it is noted that the merging is mostly effected by reducing $Da^*_{E,R}$ instead of increasing $Da^*_{E,K}$. Thus, $Da^*_{E,R}$ is more sensitive to Γ than $Da^*_{E,K}$. This is because $Da^*_{E,R}$ is usually much larger than $Da^*_{E,K}$ and hence increasing Γ implies a much larger increase of radiative loss at the radiative limit than the kinetic limit. Consequently, the extent of the decrease in $Da^*_{E,R}$ with increasing Γ is much larger than the increase in $Da^*_{E,K}$. To illustrate the effect of missing the excess enthalpy on the dual extinction limits, result without considering the excess enthalpy is also shown in Fig. 4.6 by the dashed curve. It is seen that while neglecting the excess enthalpy only has a very small effect on the kinetic extinction limit, it has a much larger effect on the radiative limit. This is due to the much larger radiative loss at the radiative extinction limit. As shown in Fig. 4.3, the excess enthalpy is negative and decreases with increasing radiative loss. Thus, the absolute value of the excess enthalpy at the radiative limit is much larger than that at the kinetic limit, and neglecting it as a factor of weakening the flame leads to an $O(1)$ overestimation of $Da^*_{E,R}$ and a slight underestimation of $Da^*_{E,K}$. For example, at

$\Gamma = 0.26$ missing the excess enthalpy leads to a 60% overestimation of $Da^*_{E,R}$ and a 13% underestimation of $Da^*_{E,K}$.

Figure 4.7 shows variations of the fuel leakage S_F with Da^* for $Le_F = Le_O = 1$ and different values of Γ. It is seen that the solutions are bounded by the two turning points, with the one at smaller Da^*, marked by "♦", represents the kinetic extinction limit, $Da^*_{E,K}$, and the one at larger Da^*, marked by "○", represents the radiative limit, $Da^*_{E,R}$. It is shown from the lower branch solution that with increasing Da^* from $Da^*_{E,K}$, S_F first decreases significantly and then levels off and finally increases as Da^* approaches $Da^*_{E,R}$, leading to the second turning point at larger Da^*. This trend is due to the fact that radiative loss is rather small near the kinetic extinction limit and insufficient residence time is the dominant mechanism for the excessive reactant leakage. Thus, increasing Da^* leads to a longer residence time and consequently more complete burning and less reactant leakage. However, for a fixed system increasing Da^* (decreasing the stretch rate) implies that the radiative loss, Ra^*, increases at the same time. Thus, at large enough Da^*, the radiative loss eventually becomes dominant and is expected to lead to substantial reduction in the flame temperature, and hence increased reactant leakage due to the substantial reduction in the reaction rate. Thus it can be concluded that the ultimate cause of extinction at the radiative limit is still the insufficient time for adequate reaction to complete. Moreover, it is seen that the fuel leakage S_F at the radiative extinction limit is smaller than that at the kinetic limit. This is because near the radiative limit, the flame is much weaker and hence is susceptible to extinguish with smaller reactant leakages. The upper branch of the solutions, plotted in dotted lines, shows the opposite dependence on

Da^* and thus is not physically realistic. The two branches of solutions form a closed isola-shaped $S_F \sim Da^*$ curve with two turning points instead of only one for the open C-shaped curve shown in Fig. 4.4b.

Figure 4.8 shows variations of the normalized flame temperature T_f/T_{ad} with Da^* for $Le_F = Le_O = 1$ and different values of Γ, where T_{ad} is the adiabatic flame temperature. It is seen that although the reactant leakage decreases and then increases with Da^*, as shown in Fig. 4.7, the flame temperature decreases monotonically because the flame suffers more radiative loss with larger Da^*.

We now study effects of the Lewis numbers of the fuel and oxidant, Le_F and Le_O, on the extinction characteristics of the counterflow diffusion flame with radiative loss. Figure 4.9 shows variations of the extinction Damköhler number, Da_E^*, with Le_F and Le_O for different values of Ra^*, respectively. It is seen that for the adiabatic flame ($Ra^* = 0$), Da_E^* increases monotonically with increasing Le_O and Le_F, consistent with the results of Seshadri & Trevino [11]. In the presence of radiative loss, Da_E^* increases monotonically with Le_O whereas it decreases and then increases with Le_F. Specifically, at small Le_F, Da_E^* is very sensitive to the radiative loss such that even a very small amount of loss, e.g. Ra^*=2E-4, is able to induce a very large relative increase of Da_E^*. However, at larger Le_F this sensitivity becomes moderate, leading to the non-monotonic dependence of Da_E^* on Le_F for a fixed Ra^*, as shown in Fig. 4.9a. The ratio of Da_E^* to its adiabatic value, $Da_{E,ad}^*$, can be obtained from Eq. (4.47)

$$\frac{Da_E^*}{Da_{E,ad}^*} = \left(\frac{T_{ad}}{T_f}\right)^6 \exp\left[T_a\left(\frac{1}{T_f} - \frac{1}{T_{ad}}\right)\right] \exp\left(h_{f,ad} - h_f\right) \frac{\Delta_{ext}}{\Delta_{ext,ad}} \tag{4.50}$$

where the subscript "ad" designates the value corresponding to the adiabatic state, i.e. Ra^* = 0. It is seen from Eq. (4.50) that radiative loss modulates Da_E^* through its effects on the flame temperature, $f_T = (T_{\text{ad}}/T_f)^6 \exp[T_a(1/T_f - 1/T_{\text{ad}})]$, excess enthalpy, $f_h = \exp\left(h_{f,\text{ad}} - h_f\right)$, and the reduced extinction Damköhler number $f_\Delta = \Delta_{\text{ext}}/\Delta_{\text{ext,ad}}$. Thus, it is necessary to evaluate their relative contributions to Da_E^* at different Lewis numbers and radiative loss.

Figure 4.10 shows variations of $Da_E^*/Da_{E,\text{ad}}^*$, f_T, f_h and f_Δ with Le_F and Le_O for Ra^* = 2.E-4, respectively. It is seen that the relative contributions from f_T, f_h and f_Δ are different at small and large values of Le_F and Le_O. Specifically, at small Le_F, radiative loss induces a very large increase of Δ_{ext}, which contributes mostly to the increase of Da_E^*. This contribution decreases significantly with increasing Le_F such that the contribution from the temperature term, f_T, becomes dominant at large Le_F. Over the entire range of Le_F, the contribution from the excess enthalpy, f_h, is secondary. However, it contributes most to the increase of Da_E^* at small Le_O, as shown in Fig. 4.10b. The contribution then decreases significantly with increasing Le_O and becomes a secondary effect as Le_O is sufficiently large. The variation of f_Δ with Le_O shows the opposite trend to f_h. It is small at small Le_O but increases with increasing Le_O and becomes comparable with f_T at large Le_O. Over the entire range of Le_O, f_T plays a consistently important role, although it is a little smaller than f_h at small Le_O. The radiative loss, Ra^* = 2.E-4, used in Fig. 4.10 can be treated as a typical order of value at which kinetic extinction occurs. Figure 4.11 shows variations of $Da_E^*/Da_{E,\text{ad}}^*$, f_T, f_h and f_Δ with Le_F and Le_O, respectively, for Ra^* = 0.01, which can be considered as a typical value at which radiative extinction

occurs. For example, for $Le_F = Le_O = 1$ and $\Gamma = 0.1$, the kinetic and radiative extinction occur at $Ra^* = 1.2E\text{-}4$ and 0.017, respectively. It is seen from Fig. 4.11 that the variations of f_Δ and f_h with Le_F and Le_O exhibit the same trend as those for small radiative loss Ra^*=2.E-4, whereas the relative contribution from the temperature term, f_T, is much larger. This is due to the larger reduction of the flame temperature under larger radiative loss. Furthermore, Figs. 4.10a and 4.11a show that it is the very large increase of Δ_{ext} from the adiabatic value at small Le_F that leads to a very large relative increase of Da_E^*, as shown in Fig. 4.9a.

Because Eq. (4.36) shows that the minimum of Δ, Δ_c, is determined by γ and in general the reduced extinction Damköhler number, Δ_{ext}, is close to Δ_c, it is instructive to explore the very high sensitivity of Δ_{ext} to radiative loss at small Le_F by studying the variations of γ with Le_F. Figure 4.12 shows variations of γ and the corresponding Δ_{ext} with Le_F for different values of Ra^*, respectively. It is seen that for the adiabatic flame, γ is close to unity at small Le_F, implying that most of the chemical heat release is conducted to the oxidant side and the flame is nearly adiabatic to the fuel side. This is because at small Le_F the flame location is very close to the oxidant stream. It is seen from Fig. 4.12b that in this case Δ_{ext} is close to zero. However, in the presence of radiative loss, which is assumed to occur at both sides of the reaction zone in the current study, the flame always has heat conducted to the fuel side to compensate for the radiative loss. Thus, γ decreases, leading to an increase of Δ_{ext} from its adiabatic value. Furthermore, because the adiabatic value of Δ_{ext} is close to zero, even a small increase of Δ_{ext} from this value, induced by a very small amount of radiative loss, implies a very large relative increase in Δ_{ext}. For example, at $Le_F = 0.5$, with the radiative loss $Ra^* = 2.E\text{-}4$, γ decreases

from 0.98 to 0.93 whereas Δ_{ext} increases from 0.053 to 0.18 which is about 3.4 times larger.

For a fixed system with radiative strength Γ, however, we have known that the extinction Damköhler number needs to satisfy $Ra^*/Da^* = \Gamma$ at the same time. Thus, Fig. 4.9 alone is not enough to demonstrate variations of the dual extinction Damköhler numbers with the Lewis numbers. In the same manner as that in Fig. 4.5, Fig. 4.13 shows variations of Da_E^* with Ra^* for $Le_F = 1$, $\Gamma = 0.1$ and different values of Le_O and the $Da^* \sim Ra^*/\Gamma$ line with $\Gamma = 0.25$. It is seen that due to the monotonic increase of Da_E^* with Le_O , increasing Le_O leads to an increase of $Da_{E,K}^*$ and a decrease of $Da_{E,R}^*$, and hence a smaller flammable range of Da^*. Furthermore, it is expected that there are no intersection points between the $Da_E^* \sim Ra^*$ curve and the $Da^* \sim Ra^*/\Gamma$ line if Le_O is larger than a critical value, indicating that steady burning is not possible if Le_O is too large.

Figure 4.14 shows variations of the dual extinction Damköhler numbers with Γ for different values of Le_O and Le_F, respectively. It is seen that for the same Γ the flammable range of Da^* diminishes with increasing Le_O, leading to a smaller Γ_c that the system can sustain. Thus increasing Le_O tends to weaken the flame monotonically. Although the dependence of Da_E^* on Le_F is not monotonic over its entire range, Fig. 4.9a shows that, with an increase of Le_F, Da_E^* decreases and increases monotonically for small and large Le_F respectively. Thus, for the same reason, it is seen from Fig. 4.14b that the flammable range of Da^* diminishes as Le_F increases from 1.5 to 2.5, and extends as Le_F increases from 0.6 to 0.8. It is noted that Mills & Matalon [8] predicted monotonic

dependence of the flammable range of Damköhler number on the Lewis number of the fuel, Le_F. This is because the radiative loss was assumed to be an O(ε) quantity and hence does not affect the leading order flame temperature. Thus radiative loss affects extinction only through the excess enthalpy which depends monotonically on Le_F.

Figure 4.15 shows variations of the dual extinction Damköhler numbers with Le_F for different values of Le_O and $\Gamma = 0.1$. It is seen that the flammable range of Da^* decreases with increasing Le_O and Le_F as it is sufficiently large. When they are both large enough, steady burning is not possible for this value of Γ. With the increase of Le_O, the maximum value of Le_F the system can sustain decreases. Figure 4.15 indicates that steady burning for radiative diffusion flames is only possible within a limited range of Lewis numbers. This is because flame extinction is purely thermal in nature under the assumption of one-step reaction and since thermal conduction and radiation are both heat loss mechanisms for flame extinction**;** extincton is induced if either of them is large enough.

4.4. Conclusions

The present study has yielded the following specific contributions and understandings regarding the subject phenomena. First, we have performed a multi-scale asymptotic analysis for the counterflow diffusion flame with flame radiative heat loss, and developed a formulation for general Lewis numbers of the fuel and oxidant with the proper consideration of the excess enthalpy that was overlooked in previous analyses. This formulation is expressed by the jump relations in terms of the outer solutions and the reactant leakages through the reaction zone. The reactant leakages are obtained from

solving the canonical form of the structure equation and hence can take advantage of previous results, such as those of Cheatham & Matalon [9]. The reason for the structure equation of the reaction zone, with a radiation zone sandwiching it in the current analysis, still can degenerates to Liñán's canonical form [3] is that the thin reaction zone is reactive-diffusive in nature. Consequently, its structure may not be directly affected by the particulars of the system. Thus, it is possible to perform a generalized analysis of the reaction zone with the influences of all the outside processes including radiative loss coming in from the boundary conditions through matching.

Second, this formulation is then applied to study the extinction characteristics of the radiative counterflow diffusion flame with non-unity Lewis numbers of the fuel and oxidant. In addition to the dual extinction limits, namely the kinetic limit at lower Damköhler numbers and radiative limit at higher Damköhler numbers, identified in previous analyses [2, 4-5], the current study has also gained some additional understandings, especially on the effects of non-unity Lewis numbers. It is found that the kinetic extinction limit is minimally affected by radiative loss so that extinction occurs close to the adiabatic flame temperature, while substantial amount of heat loss is associated with the radiative limit such that the flame temperature at extinction is significantly reduced from the adiabatic value. Reactant leakage, however, is ultimately the root cause for both limits, with the extent of leakage being higher for the kinetic limit. The flammable range of the Damköhler number decreases monotonically with increasing Le_O, indicating that increasing Le_O tends to weaken the flame. However, this range shows non-monotonic dependence on Le_F in that it increases and decreases with increasing Le_F as it is sufficiently small and large respectively. This non-monotonic dependence is due

to the very high sensitivity of the extinction Damköhler number to radiative loss at small Le_F. The cause for this phenomenon is that the flame is located very close to the oxidant stream at small Le_F so that most of the chemical heat release is conducted to the oxidant side and the flame is nearly adiabatic to the fuel side. A small amount of radiative loss can lead the flame to deviate from this condition and hence to a rather large relative increase of the extinction Damköhler number. The influence of radiative loss on the extinction Damköhler numbers is found to be through its effects on the flame temperature, excess enthalpy and the reduced extinction Damköhler number, and their relative contributions are different under different radiative loss and Lewis numbers of the fuel and oxidant. In most cases, the contribution from the flame temperature is the largest and its relative importance increases with increasing radiative loss. The contributions from the other two, however, are also important in some cases. At small Le_F when the flame is located very close to the oxidant stream, the contribution from the reduced extinction Damköhler number is large and even dominant in the case of small radiative loss. The contribution from the excess enthalpy is important for small Le_O and it may be comparable to that from the flame temperature when radiative loss is small. Thus, overlooking the excess enthalpy in previous analyses may result in rather large errors in the predicted extinction Damköhler numbers, especially the kinetic one. Moreover, it is found that for a fixed relative radiative strength, steady burning may not be possible when the Lewis numbers of the fuel and oxidant are too large. Finally, it should be noted that the above discussions are meant for large initial mixture strengths so that the flame is located in the oxidant side of the stagnation surface. The roles of Le_F and Le_O should be

interchanged for small initial mixture strengths under which the flame is located in the fuel side of the stagnation surface.

Third, the relations (4.37)-(4.41), developed in this study for the counterflow diffusion flame with flame radiation as a demonstration problem, can be applied to any one-dimensional configuration with Eq. (4.41) revised as

$$\left[Bu_f T_1 - \frac{1}{A}\frac{\partial T_1}{\partial x} \right] = -\left[u_f Y_{F,1} - Le_F^{-1}\frac{\partial Y_{F,1}}{\partial x} \right] = -\left[u_f Y_{O,1} - Le_O^{-1}\frac{\partial Y_{O,1}}{\partial x} \right]$$

where u_f is the flow speed at the flame sheet.

Furthermore, although this formulation is applied exclusively to the extinction analysis in the current study, it is also applicable to the analyses of thermal-diffusive instabilities in a similar manner as those in Cheatham & Matalon [9] and Kukuck & Matalon [10]. For example, we introduce small perturbations in the form

$$(T, Y_F, Y_O) = (T_b, Y_{F,b}, Y_{O,b}) + \varepsilon\alpha(u(x), v(x), w(x))\exp(ik_1 y + \sigma t) \qquad (4.51)$$

where the subscript "b" designates the basic steady state solutions, y is the transverse direction, k_1 the wave number in this direction, σ a complex number whose real part identifies the growth rate of the perturbation, α a small parameter and u, v and w the perturbations for T, Y_F and Y_O, respectively. Substituting Eq. (4.51) into the governing equations (4.1)-(4.3) and Eqs. (4.37)-(4.41) yields the governing equations and the jump and leakage conditions for the perturbations, from which the dispersion relation relating the growth rate to the parameters describing the combustion system, such as the Damköhler number and the Lewis numbers of the fuel and oxidant, is formed. Because this model is able to predict the dual extinction limits of radiative diffusion flames, it is expected to predict the neutral stability boundaries near both the kinetic and radiative

extinction limits. This work will be discussed in detail in the next chapter using the same chambered planar flame as that in Chapter 2.

Finally, it should be emphasized that although the inclusion of excess enthalpy does not lead to qualitative differences in the extinction results, it is a crucial element in the stability analyses, as indicated by Matalon [12]. Thus, the model developed in this chapter with the proper consideration of the excess enthalpy is essential for the following studies on the flame oscillations driven by the thermal-diffusive instability in radiation-affected diffusion flames.

Appendix

Integrating Eq. (4.23) and applying the matching conditions, $\Theta_2^{\pm}\big|_{\zeta\to\pm\infty} \sim -\infty$ and $\Theta_2^{\pm}(0) \sim 0$, yield

$$\frac{d\Theta_2^{\pm}}{d\zeta} = \mp\sqrt{\left(\frac{\partial T_0^{\pm}(x_f)}{\partial x}\right)^2 + 2RaT_f \exp\left(\frac{\Theta_2^{\pm}}{T_f}\right)} \tag{4.A1}$$

and

$$\frac{d\Theta_2^{\pm}(0)}{d\zeta} = A^{\pm}\frac{\partial T_0^{\pm}(x_f)}{\partial x} \tag{4.A2}$$

Multiplying Eq. (4.24) by $d\Theta_2^{\pm}/d\zeta$, integrating once and applying the matching conditions (4.12) for $d\Theta_1^{\pm}/d\zeta$, $d\Theta_2^{\pm}/d\zeta$ and $\Theta_2^{\pm}$ as $\zeta \to \pm\infty$ yield

$$\frac{d\Theta_1^{\pm}(0)}{d\zeta}\frac{d\Theta_2^{\pm}(0)}{d\zeta} = Ra\Theta_1^{\pm}\exp\left(\frac{\Theta_2^{\pm}}{T_f}\right) \tag{4.A3}$$

Substituting Eq. (4.23) into (4.A3) to replace the term $Ra\exp\left(\Theta_2^{\pm}/T_f\right)$ by $d^2\Theta_2^{\pm}/d\zeta^2$, integrating once and applying the matching condition (4.12) for $\Theta_1^{\pm}$ and $\Theta_2^{\pm}$ as $\zeta \to \pm\infty$ yield

$$\Theta_1^{\pm} = \left(\frac{T_1^{\pm}(x_f)}{\partial T_0^{\pm}(x_f)/\partial x}\right)\frac{d\Theta_2^{\pm}}{d\zeta} = T_1^{\pm}(x_f)\sqrt{1+\frac{2RaT_f}{\left(\partial T_0^{\pm}(x_f)/\partial x\right)^2}\exp\left(\frac{\Theta_2^{\pm}}{T_f}\right)} \tag{4.A4}$$

and

$$\Theta_1^{\pm}(0) = A^{\pm}T_1^{\pm}(x_f) \tag{4.A5}$$

Integrating Eq. (4.25) once in the same manner yields

$$\frac{d\Theta_2^{\pm}}{d\zeta}\frac{d\Theta_3^{\pm}}{d\zeta} = -x_f\int\frac{d\Theta_1^{\pm}}{d\zeta}\frac{d\Theta_2^{\pm}}{d\zeta}d\zeta + Ra\Theta_3^{\pm}\exp\left(\frac{\Theta_2^{\pm}}{T_f}\right) + C^{\pm} \tag{4.A6}$$

where $C^{\pm}$ are integral constants. Substituting Eq. (4.A4) into (4.A6) to replace the term $d\Theta_2^{\pm}/d\zeta$ by $\left(\frac{\partial T_0^{\pm}(x_f)/\partial x}{T_1^{\pm}(x_f)}\right)\Theta_1^{\pm}$ and applying the matching condition (4.12) for $\Theta_1^{\pm}$, $\Theta_2^{\pm}$ and $d\Theta_3^{\pm}/d\zeta$ as $\zeta \to \pm\infty$ lead to

$$C^{\pm} = \frac{\partial T_0^{\pm}(x_f)}{\partial x}\left(\frac{\partial T_1^{\pm}(x_f)}{\partial x} + \frac{1}{2}x_f T_1^{\pm}(x_f)\right)$$

and

$$\frac{d\Theta_3^{\pm}}{d\zeta} = -\frac{1}{2}x_f T_1^{\pm}(x_f)\sqrt{1+\frac{2RaT_f\exp\left(\Theta_2^{\pm}/T_f\right)}{\left(\partial T_0^{\pm}(x_f)/\partial x\right)^2}} + \frac{T_1^{\pm}(x_f)}{\left(\partial T_0^{\pm}(x_f)/\partial x\right)^2}Ra\Theta_3^{\pm}\exp\left(\frac{\Theta_2^{\pm}}{T_f}\right)$$
$$+\frac{\partial T_1^{\pm}(x_f)/\partial x + \frac{1}{2}x_f T_1^{\pm}(x_f)}{\sqrt{1+\frac{2RaT_f\exp\left(\Theta_2^{\pm}/T_f\right)}{\left(\partial T_0^{\pm}(x_f)/\partial x\right)^2}}}$$

Then, applying the matching conditions, $\Theta_2^{\pm}(0) \sim 0$ and $\Theta_3^{\pm}(0) \sim 0$, yields

$$\frac{d\Theta_3^{\pm}(0)}{d\zeta} \sim \frac{1}{2}\left(A^{\pm} - \frac{1}{A^{\pm}}\right)T_1^{\pm}(x_f) + \frac{1}{A^{\pm}}\frac{\partial T_1^{\pm}(x_f)}{\partial x} \qquad (4.A7)$$

References

1. Sohrab, S. H., Liñán, A. and Williams, F. A., *Combust. Sci. Technol.* **27**: 143-154 (1982).
2. Chao, B. H., Law, C. K., T'ien, J. S., *Proc. Combust. Inst.* **23**: 523–531 (1990).
3. Liñán, A., *Acta Astronautica* **1**: 1007-1039 (1974).
4. Oh, T. K., Lee, J. S. and Chung, S. H., *Int. J. Heat Mass Transfer* **37**: 2893-2900 (1994).
5. Liu, F., Smallwood, G. J., Gulder, O. L. and Ju, Y., *Combust. Flame* **121**: 275-287 (2000).
6. Maruta, K., Yoshida, M., Guo, H., Ju, Y. and Niioka, T., *Combust. Flame* **112**: 181-187 (1998).
7. Kim, J. S. and Williams, F. A., *J. Eng. Math.* **31**: 101-118 (1997).
8. Mills, K. and Matalon, M., *Proc. Combust. Inst.* **27**: 2535–2541 (1998).
9. Cheatham, S. and Matalon, M., *J. Fluid Mech.* **414**: 105-144 (2000).
10. Kukuck, S. and Matalon, M., *Combust. Theory Modelling* **5**: 217-240 (2001).
11. Seshadri, K. and Trevino, C., *Combust. Sci. and Technol.* **64**: 243-261 (1989).
12. Matalon, M., *Ann. Rev. Fluid Mech.* **39**: 163-191 (2007).

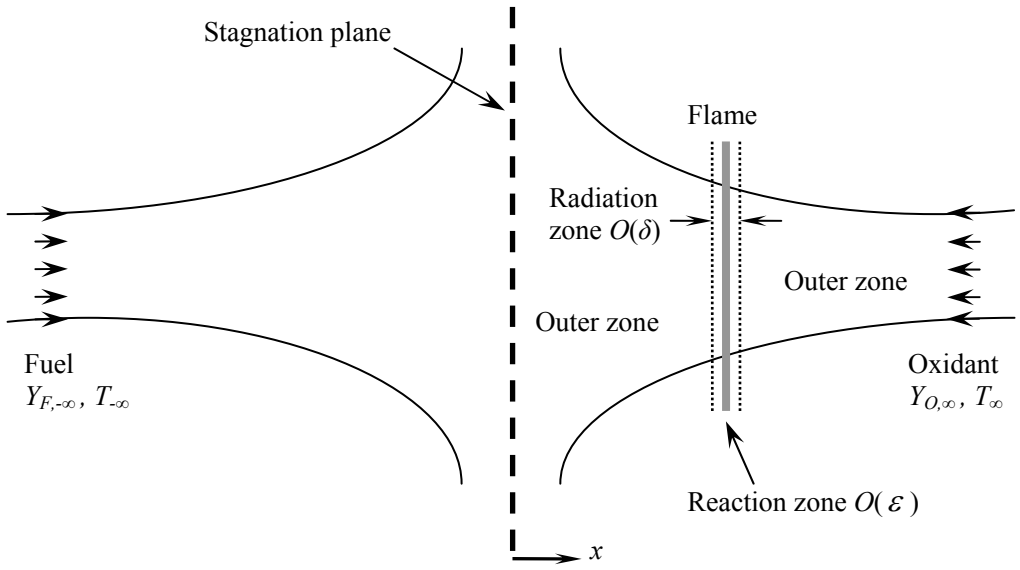

Figure 4.1. Schematic of a counterflow diffusion flame.

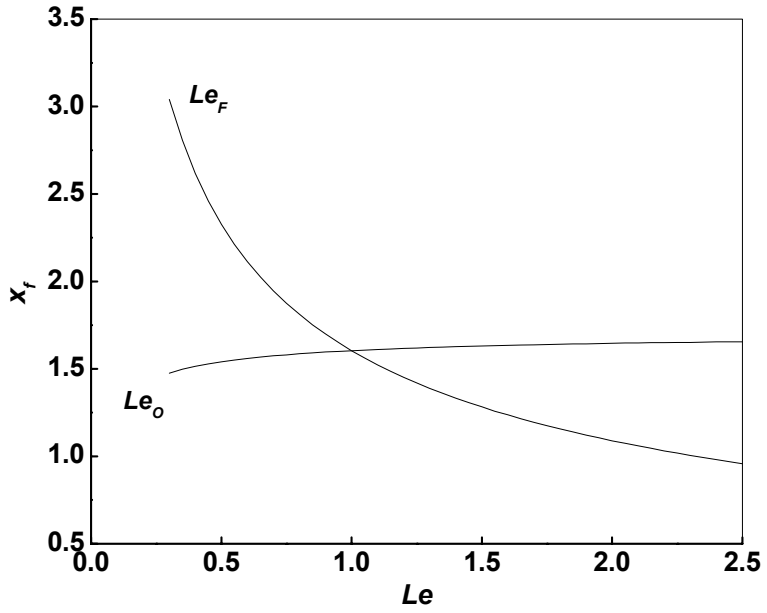

Figure 4.2. Variations of the flame sheet location, x_f, with the fuel and oxidant Lewis numbers, Le_F ($Le_O = 1$) and Le_O ($Le_F = 1$).

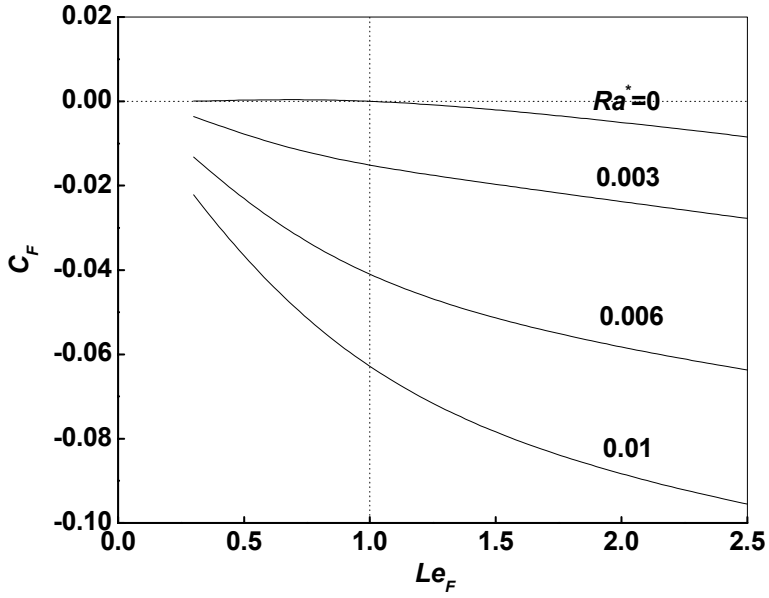

(a)

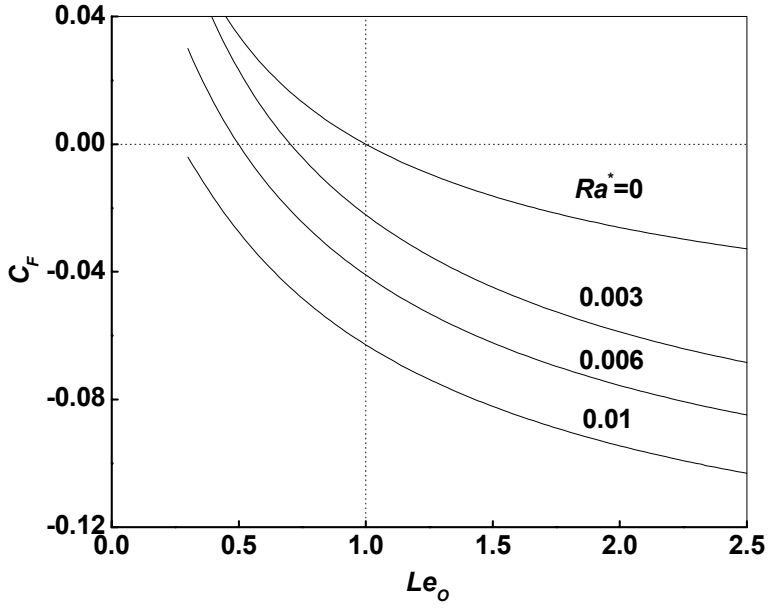

(b)

Figure 4.3. Variations of the coefficient of fuel leakage in the total excess enthalpy, C_F, with Le_F ($Le_O = 1$) (a), and Le_O ($Le_F = 1$) (b), for different values of radiative loss, Ra^*.

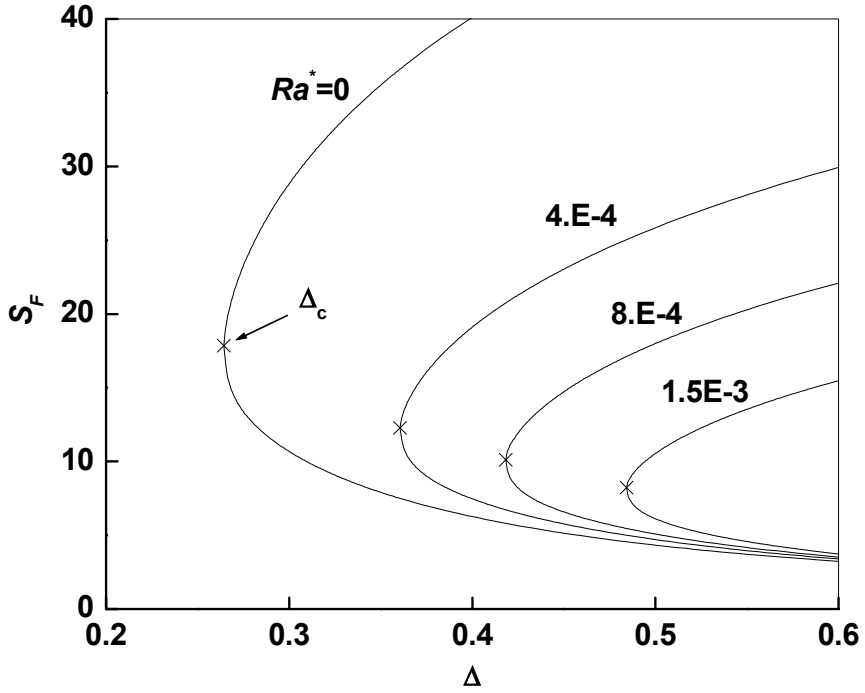

(a)

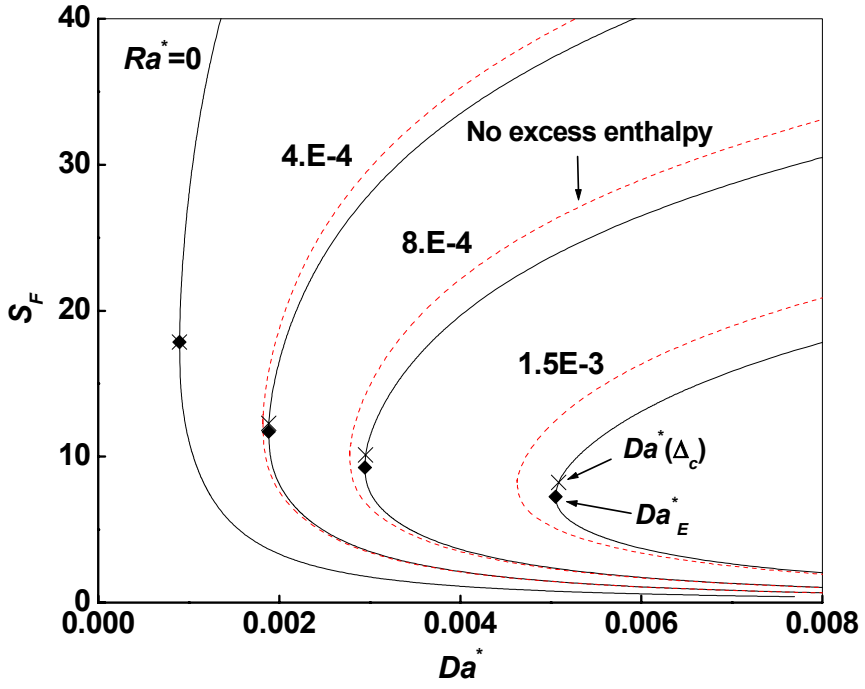

(b)

Figure 4.4. Fuel leakage S_F as functions of the reduced Damköhler number Δ and Damköhler number Da^* for $Le_F = Le_O = 1$ and different values of radiative loss, Ra^*.

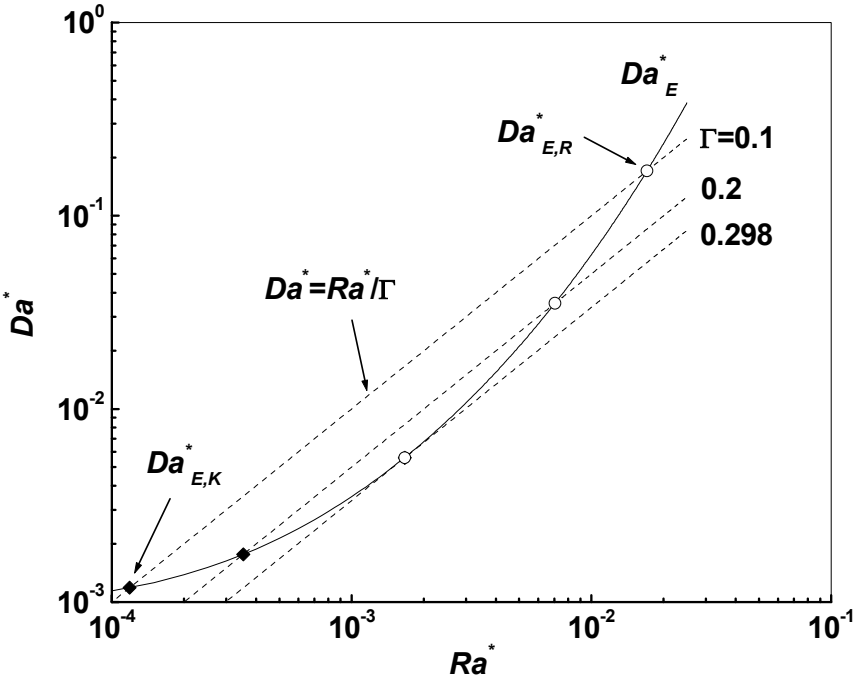

Figure 4.5. Variations of the extinction Damköhler number, Da_E^*, with the radiative loss, Ra^*, for $Le_F = Le_O = 1$ and the Da^* versus Ra^*/Γ lines for different relative radiative strength, Γ.

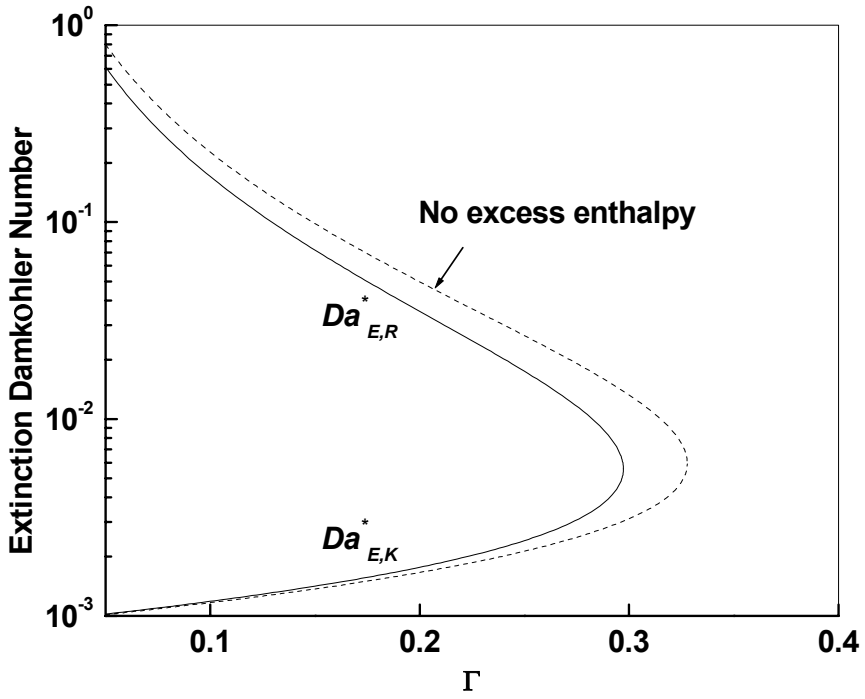

Figure 4.6. Variations of the dual extinction Damköhler numbers with the relative radiative strength Γ for $Le_F = Le_O = 1$ with and without considering the excess enthalpy.

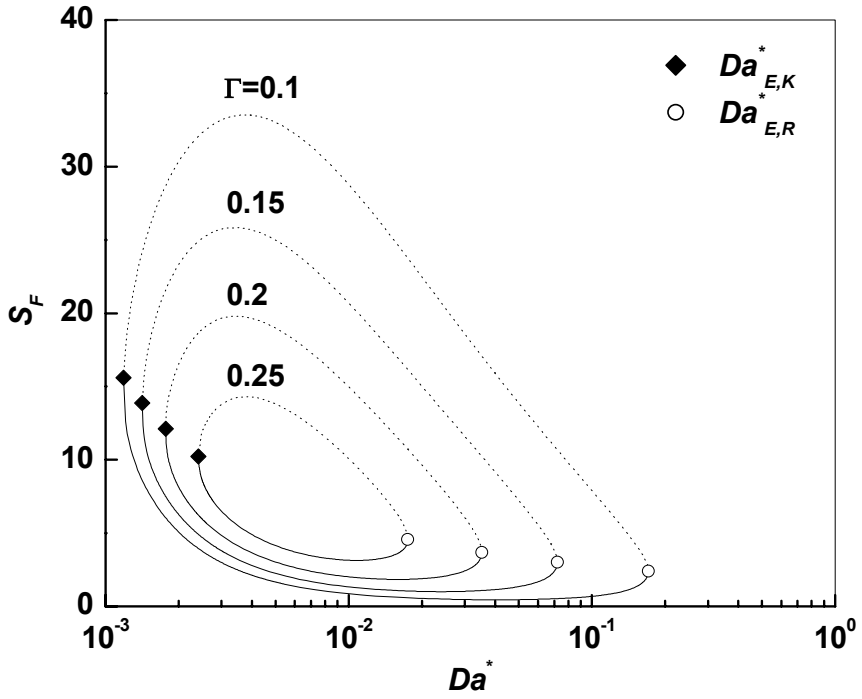

Figure 4.7. Fuel leakage S_F as a function of the Damköhler number Da^* for $Le_F = Le_O = 1$ and different relative radiative strength Γ.

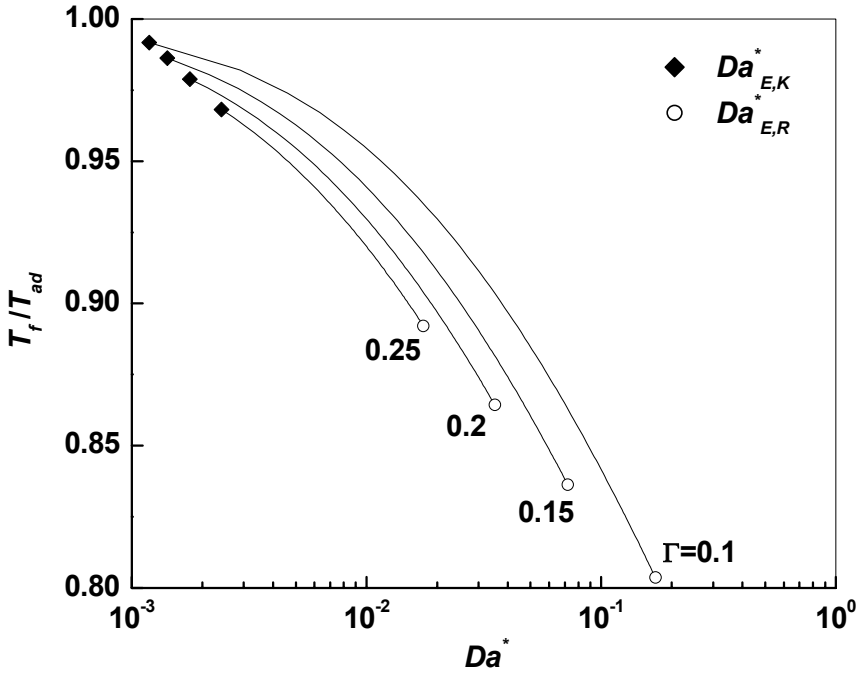

Figure 4.8. Variations of the normalized flame temperature T_f / T_{ad} with the Damköhler number Da^* for $Le_F = Le_O = 1$ and different relative radiative strength Γ.

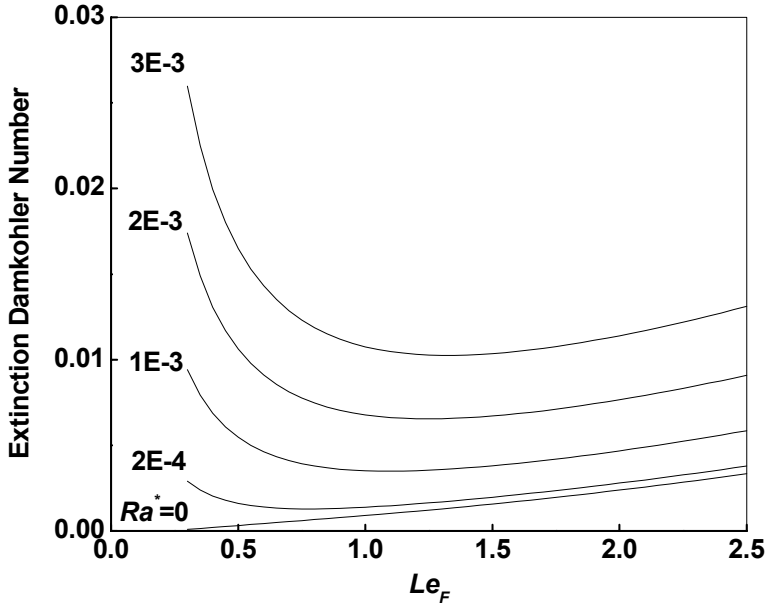

(a)

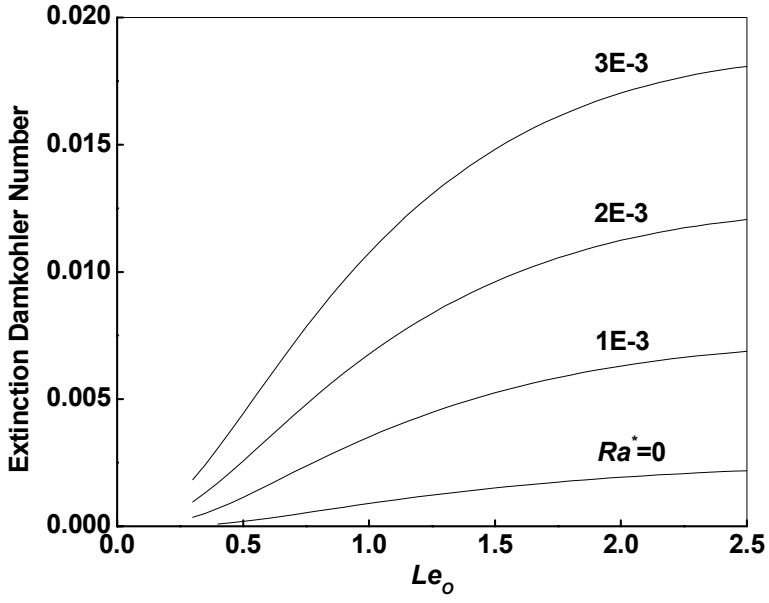

(b)

Figure 4.9. Variations of the extinction Damköhler number Da_E^* with Le_F (Le_O = 1) (a), and Le_O (Le_F = 1) (b), for different values of radiative loss, Ra^*.

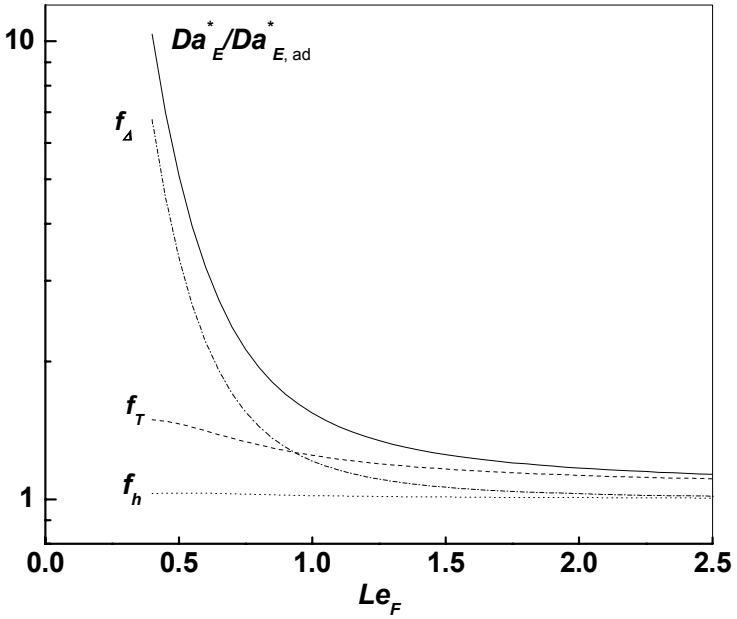

(a)

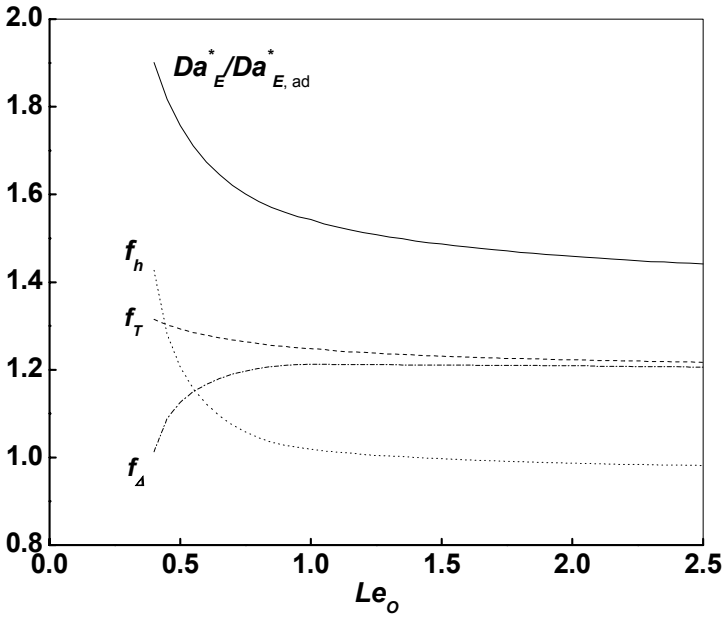

(b)

Figure 4.10. Variations of the ratio of the extinction Damköhler number $Da_E^* / Da_{E,\mathrm{ad}}^*$ and the contributions from the effects of radiative loss on the flame temperature, f_T, excess enthalpy, f_h, and the reduced extinction Damköhler number, f_Δ, with Le_F (Le_O = 1) (a), and Le_O (Le_F = 1) (b), for radiative loss Ra^* = 2.E-4.

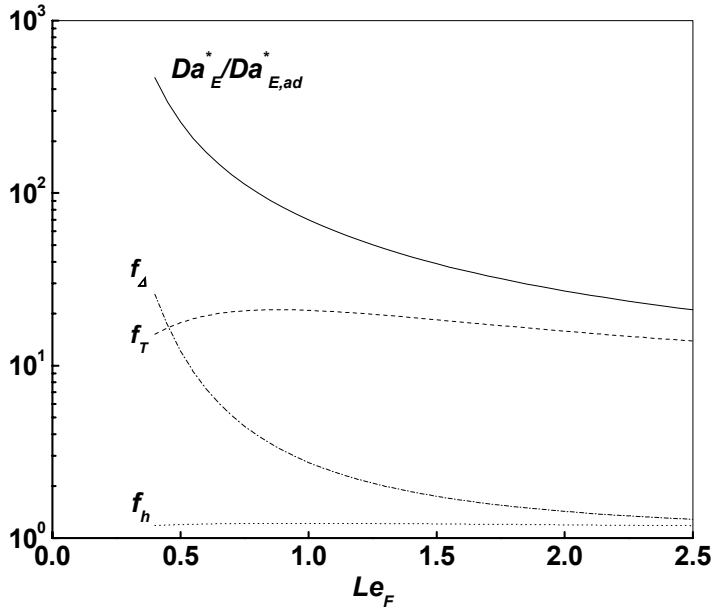

(a)

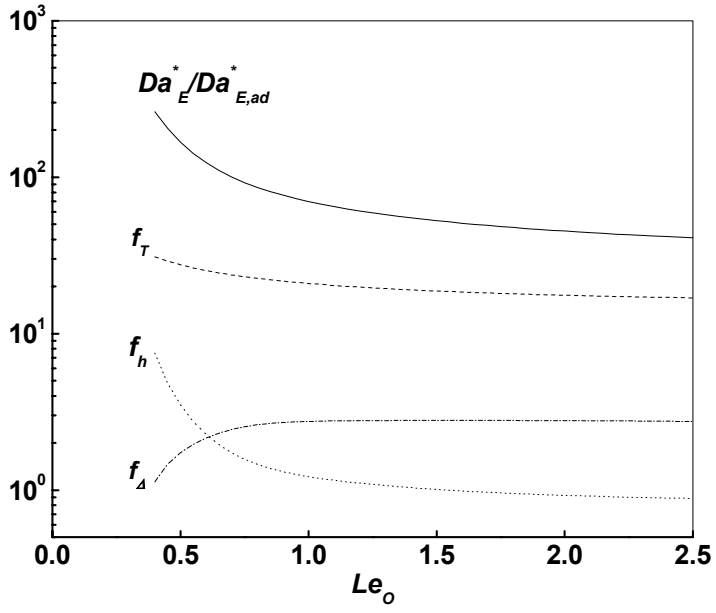

(b)

Figure 4.11. Variations of the ratio of the extinction Damköhler number $Da^*_E / Da^*_{E,\mathrm{ad}}$ and the contributions from the effects of radiative loss on the flame temperature, f_T, excess enthalpy, f_h, and the reduced extinction Damköhler number, f_Δ, with Le_F (Le_O = 1) (a), and Le_O (Le_F = 1) (b), for radiative loss Ra^* = 0.01.

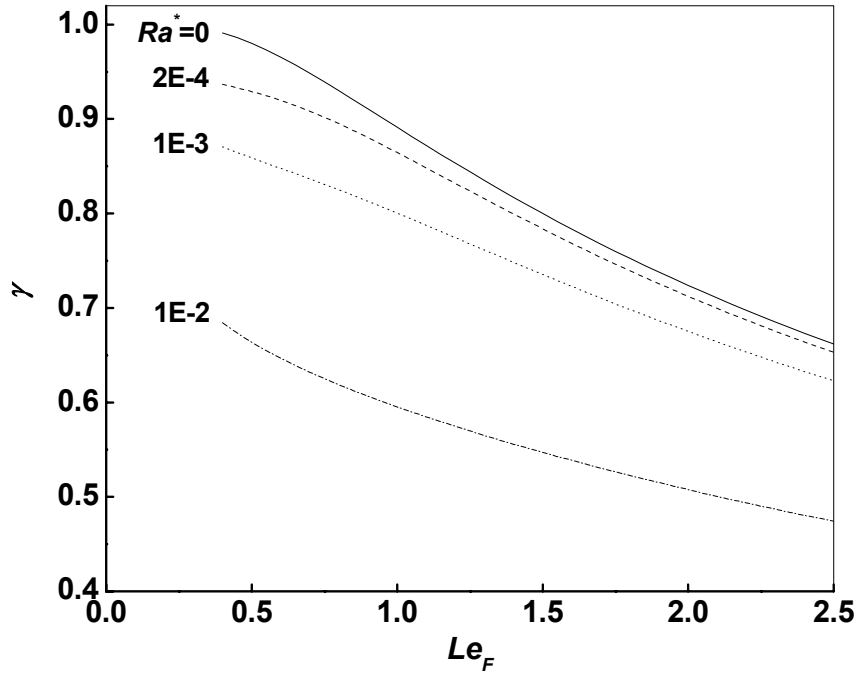

(a)

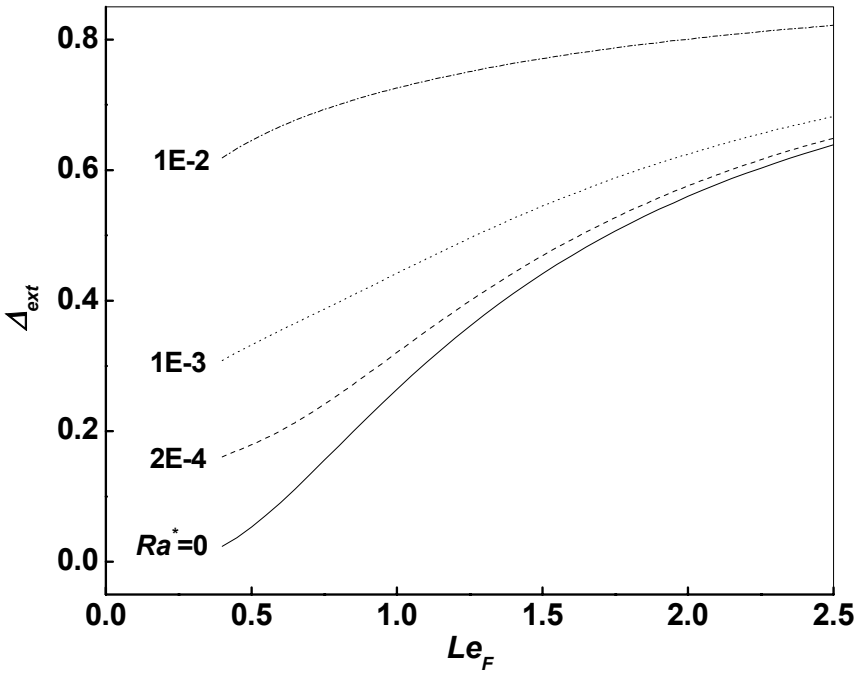

(b)

Figure 4.12. Variations of γ (a), and the reduced extinction Damköhler number Δ_{ext} (b), with Le_F for $Le_O = 1$ and different values of radiative loss, Ra^*.

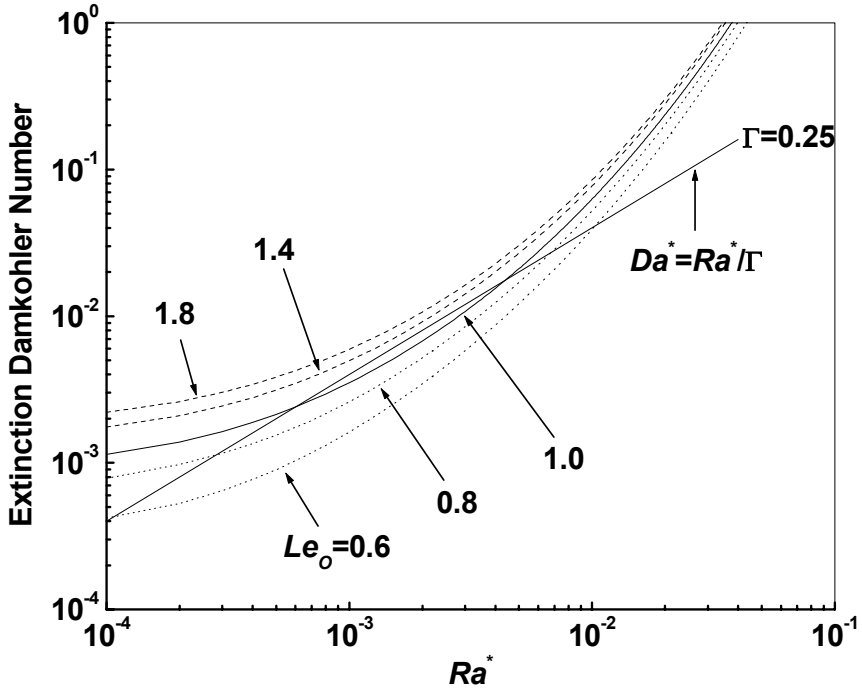

Figure 4.13. Variations of the extinction Damköhler number, Da_E^*, with radiative loss, Ra^*, for Le_F = 1, Γ = 0.1 and different values of Le_O and the Da^* versus Ra^*/Γ line with relative radiative strength Γ = 0.25.

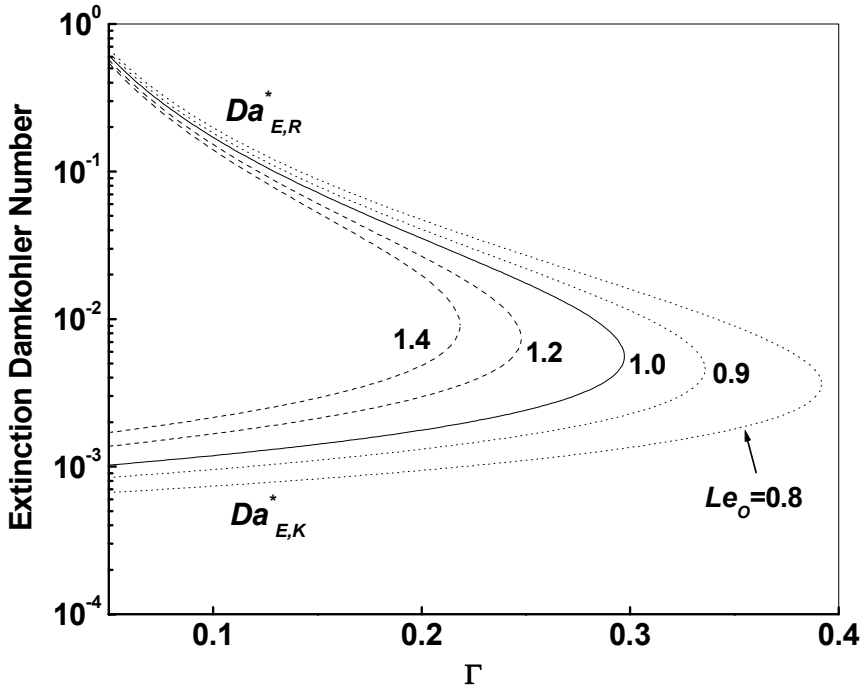

(a)

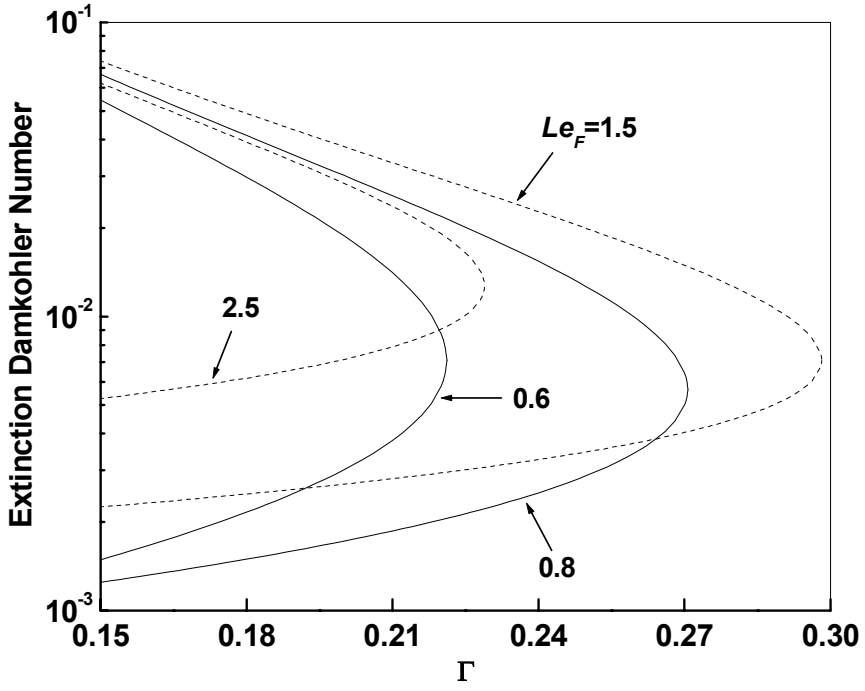

(b)

Figure 4.14. Variations of the dual extinction Damköhler numbers with relative radiative strength Γ for different values of Le_O (Le_F = 1) (a), and Le_F (Le_O = 1) (b).

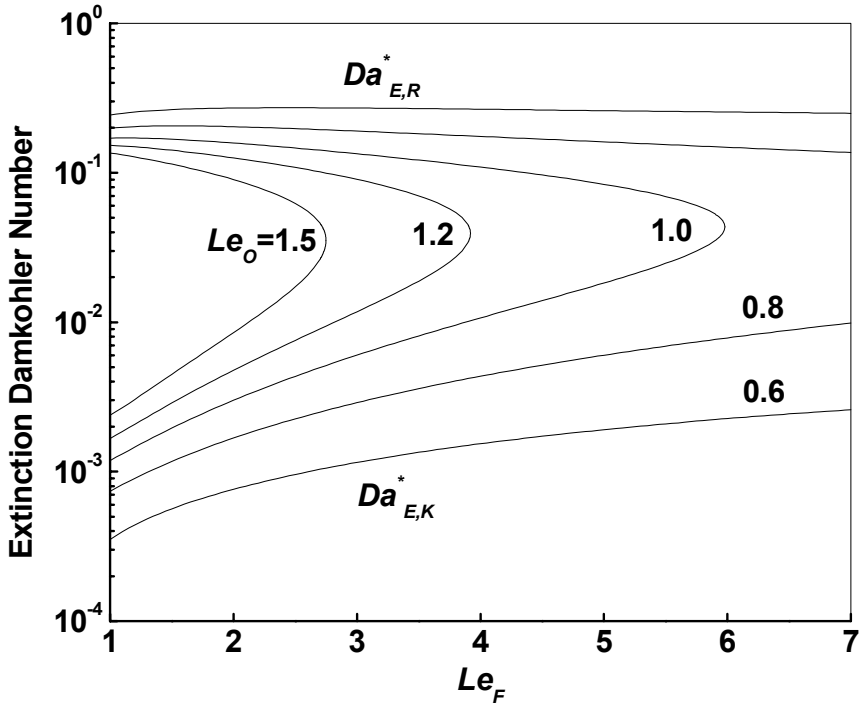

Figure 4.15. Variations of the dual extinction Damköhler numbers with Le_F for different values of Le_O and relative radiative strength $\Gamma = 0.1$.

Chapter 5: Intrinsic Oscillation in Radiation-Affected Diffusion Flames

5.1. Background

In this chapter, we conduct a linear stability analysis on the onset of intrinsic flame oscillations in 1D chambered planar flames with radiative heat loss. The primary objective of the present study is to generalize the oscillatory instability analysis of [1] to include arbitrary heat loss so that it is applicable to situations near both the kinetic and radiative extinction limits. Drawing insight from the results of Chapter 4 that the steady-state reaction zone structures and the states of extinction for both the kinetic and radiative extinction limits are canonically the same, being described by Liñán's solution [2], it is reasonable to expect that a similar canonical representation should also exist for the kinetically and radiatively induced oscillation. The fact that oscillation can develop near either extinction limit has also been demonstrated through several numerical studies [3-5]. Specifically, Christiansen *et al.* [3] simulated the transient behavior of burner-supported spherical diffusion flames using detailed chemistry and transport, and observed oscillatory instability near both limits. It is further found that flame oscillation near both limits always grows in amplitude leading to flame extinction, although the flame near the radiative limit is able to sustain longer time of oscillation. Sohn *et al.* [4] studied the nonlinear evolution of oscillation triggered by radiative heat loss in a diffusion flame established in the stagnant mixing layer, and identified three different transient flame

evolution behaviors, namely decaying oscillatory solution, diverging solution to extinction, and stable limit-cycle solution, with the last one achievable only near the radiation limit. Miklavčič *et al.* [5] numerically studied the island [6] evolution from the S-curve of steady states and flame oscillation in radiating diffusion flames, and found that stable oscillation may develop at large Damköhler numbers if radiative loss is sufficiently large.

The formulation and results are sequentially presented in the following. It will be shown that we have indeed succeeded in obtaining a unified solution that describes the loss of stability at both the kinetic and radiative limits. Using this general solution, interesting characteristics of radiation-induced oscillation are identified.

5.2. Formulation

5.2.1. Governing Equations

We consider the same 1D flame configuration as those in Chapters 2 and 3, as shown in Fig. 5.1 with the structure of the radiation zone. With the same assumptions as those employed in Chapter 4, the appropriate nondimensional governing equations can be written as

$$\frac{\partial T}{\partial t}+\frac{\partial T}{\partial x}-\frac{\partial^2 T}{\partial x^2}=\omega-q_R \tag{5.1}$$

$$\frac{\partial Y_F}{\partial t}+\frac{\partial Y_F}{\partial x}-Le_F^{-1}\frac{\partial^2 Y_F}{\partial x^2}=-\omega \tag{5.2}$$

$$\frac{\partial Y_O}{\partial t}+\frac{\partial Y_O}{\partial x}-Le_O^{-1}\frac{\partial^2 Y_O}{\partial x^2}=-\omega \tag{5.3}$$

subject to the boundary conditions

$$T = T_{-\infty} \qquad Y_F = 1 \qquad Y_O = 0 \qquad \text{as } x \to -\infty \tag{5.4}$$

$$T = T_{-\infty} + \Delta T \qquad Y_F = 0 \qquad Y_O = \phi^{-1} \quad \text{at } x = 0 \tag{5.5}$$

where $\omega = Da_C Y_F Y_O \exp(-T_a/T)$ is the chemical reaction rate, $q_R = 4\sigma\kappa q^3 \lambda T^4/(\tilde{\rho}^2 c_p^5 \tilde{U}^2)$ the radiative heat loss, $Da_C = B_K \tilde{Y}_{F,-\infty} \lambda \nu_O/(W_F c_p \tilde{U}^2)$ the collision Damköhler number, λ and U respectively denote the thermal conductivity and convection velocity, and the over-tilde "~" designates dimensional or unscaled quantities. Here and hereafter, all the unspecified parameters have been defined in previous chapters.

Equations (5.1)-(5.3) are subjected to the jump and leakage conditions derived in Chapter 4 with only Eq. (4.31) being accommodated with the current flame configuration:

$$[T_0] = [Y_{F,0}] = [Y_{O,0}] = Y_{F,0}^+(0) = Y_{O,0}^-(0) = 0 \tag{5.6}$$

$$\left[A\frac{\partial T_0}{\partial x}\right] = -Le_F^{-1}\left[\frac{\partial Y_{F,0}}{\partial x}\right] = -Le_O^{-1}\left[\frac{\partial Y_{O,0}}{\partial x}\right] \tag{5.7}$$

$$[AT_1] = -Le_F^{-1}[Y_{F,1}] = -Le_O^{-1}[Y_{O,1}] \tag{5.8}$$

$$\left[BT_1 - \frac{1}{A}\frac{\partial T_1}{\partial x}\right] = -\left[Y_{F,1} - Le_F^{-1}\frac{\partial Y_{F,1}}{\partial x}\right] = -\left[Y_{O,1} - Le_O^{-1}\frac{\partial Y_{O,1}}{\partial x}\right] \tag{5.9}$$

$$Y_{F,1}^+(x_f) = Le_F S_F(\gamma, \Delta), \quad Y_{O,1}^-(x_f) = Le_O S_O(\gamma, \Delta) \tag{5.10}$$

where

$$\gamma = \left(A^+\frac{\partial T_0^+(x_f)}{\partial x} + A^-\frac{\partial T_0^-(x_f)}{\partial x}\right)\left[A\frac{\partial T_0}{\partial x}\right]^{-1} \tag{5.11}$$

$$\Delta = 4Le_F Le_O Da\left[A\frac{\partial T_0}{\partial x}\right]^{-2}\exp\left(\frac{1+\gamma}{2}h_O + \frac{1-\gamma}{2}h_F\right) \tag{5.12}$$

and $Da = \varepsilon^3 Da_C \exp(-T_a/T_f)$.

5.2.2. Steady-State Basic Solutions

Applying the boundary conditions and the jump relations (5.4)-(5.7), the $O(1)$ outer solutions, T_0, $Y_{F,0}$ and $Y_{O,0}$ can be respectively solved as

$$T_0 = \begin{cases} T_{-\infty} + \left(T_f - T_{-\infty}\right)e^{x-x_f}, & x < x_f \\ T_f + \left(T_{-\infty} + \Delta T - T_f\right)\dfrac{e^x - e^{x_f}}{1 - e^{x_f}}, & x > x_f \end{cases}$$

$$Y_{F,0} = \begin{cases} 1 - e^{Le_F(x-x_f)}, & x < x_f \\ 0, & x > x_f \end{cases}$$

$$Y_O = \begin{cases} 0, & x < x_f \\ -1 + (1+\phi^{-1})e^{Le_O x}, & x > x_f \end{cases}$$

where the flame location x_f and temperature T_f are solved from the jump relation (5.7) as $x_f = -Le_O^{-1}\ln(1+\phi^{-1})$ and

$$\sqrt{\left(\frac{\partial T_0^+(x_f)}{\partial x}\right)^2 + 2RaT_f} + \sqrt{\left(\frac{\partial T_0^-(x_f)}{\partial x}\right)^2 + 2RaT_f} = 1 \tag{5.13}$$

As discussed in Chapter 4, Eq. (5.13) states that the heat release is conducted away from the reaction zone to both sides. Radiative heat loss enhances heat conduction through the term $2RaT_f$ to compensate for the heat loss, and suppresses it through the reduction of the temperature gradient. Thus, the net effect of radiative loss is to modify the heat conduction rate, and as such it plays the similar role as varying the thermal diffusivity of the reactants.

Applying the homogeneous boundary conditions as well as the jump and leakage conditions (5.8)-(5.10) for the $O(\varepsilon)$ outer solutions, T_1, $Y_{F,1}$ and $Y_{O,1}$ can be completely

determined. Here we only show them in the form of excess enthalpies, h_F and h_O, because they are the reason why the $O(\varepsilon)$ outer solutions are required. Thus we have

$$h_F = [A^+ a_{1F}(1-e^{x_f})+1]S_F + A^+ a_{1O}(1-e^{x_f})S_O$$

$$h_O = (A^- a_{2F} e^{x_f})S_F + (A^- a_{2O} e^{x_f}+1)S_O$$

where

$$a_{1O} = K^{-1}(B^- - 1/A^-)$$

$$a_{2O} = K^{-1}[B^+ e^{-x_f} - (B^+ - 1/A^+)]$$

$$a_{1F} = K^{-1}[A^- - (B^- - 1/A^-)Le_O^{-1}(1-e^{Le_O x_f})]Le_F(1-e^{Le_F x_f})^{-1}$$

$$a_{2F} = K^{-1}e^{-x_f}\{A^+(1-e^{x_f}) - [B^+ - (B^+ - 1/A^+)e^{x_f}]Le_O^{-1}(1-e^{Le_O x_f})\}Le_F(1-e^{Le_F x_f})^{-1}$$

$$K = A^+(B^- - 1/A^-)(1-e^{x_f}) - A^-[B^+ - (B^+ - 1/A^+)e^{x_f}]$$

5.2.3. Linear Stability Analysis

We introduce small planar perturbations, with amplitude $\alpha << 1$, superimposed onto the steady-state basic solutions identified below by subscript "b":

$$(T, Y_F, Y_O) = (T_b, Y_{F,b}, Y_{O,b}) + \varepsilon\alpha e^{\sigma}(u(x), v(x), w(x)) \tag{5.14}$$

where σ is a complex number whose real part identifies the growth rate of the perturbation. Substituting Eq. (5.14) into the chemically and radiatively frozen form of Eqs. (5.1)-(5.3) yields the governing equations for the perturbations,

$$u_{xx} - u_x - \sigma u = 0 \tag{5.15}$$

$$v_{xx} - Le_F v_x - \sigma Le_F v = 0 \tag{5.16}$$

$$w_{xx} - Le_O w_x - \sigma Le_O w = 0 \tag{5.17}$$

Equations (5.15)-(5.17) are subjected to the homogeneous boundary conditions at $x \to -\infty$ and $x = 0$ and can be solved as

$$(u,v,w) = \begin{cases} C_J^- \exp[(Le_J/2 + \lambda_J)x], & x < x_f \\ C_J^+ \{\exp[(Le_J/2 + \lambda_J)x] - \exp[(Le_J/2 - \lambda_J)x]\}, & x > x_f \end{cases}$$

where $J = T, F, O$ correspond to the solutions of u, v and w, respectively, and we have employed the notation

$$\lambda_J = \sqrt{(Le_J/2)^2 + Le_J \sigma}$$

with $Le_T = 1$. The integration constants C_J^- and C_J^+ are to be determined through the jump and leakage conditions for the perturbations that are derived by inserting Eq. (5.14) into Eqs. (5.8)-(5.10),

$$[Au] = -Le_F^{-1}[v] = -Le_O^{-1}[w] \tag{5.18}$$

$$\left[Bu - A^{-1}u_x\right] = -\left[v - Le_F^{-1}v_x\right] = -\left[w - Le_O^{-1}w_x\right] \tag{5.19}$$

$$(1-\gamma)Le_F b_F A^+ u^+ + (1+\gamma)Le_F b_F A^- u^- + \{(1-\gamma)b_F - 2\}v^+ + \{(1+\gamma)Le_F b_F / Le_O\}w^- = 0 \tag{5.20}$$

$$(1-\gamma)Le_O b_O A^+ u^+ + (1+\gamma)Le_O b_O A^- u^- + \{(1-\gamma)Le_O b_O / Le_F\}v^+ + \{(1+\gamma)b_O - 2\}w^- = 0 \tag{5.21}$$

where $b_i = \Delta_b \partial S_i(\gamma, \Delta_b)/\partial \Delta_b$, (i=F, O), and Δ_b is the reduced Damköhler number evaluated at the steady state condition.

The jump relations (5.18) and (5.19) yield

$$A^+ u^+ - A^- u^- + Le_F^{-1}v^+ - Le_F^{-1}v^- = 0 \tag{5.22}$$

$$A^+ u^+ - A^- u^- + Le_O^{-1}w^+ - Le_O^{-1}w^- = 0 \tag{5.23}$$

$$f_T u^+ + g_T u^- + f_F v^+ + (1/2 - Le_F^{-1}\lambda_F)v^- = 0 \tag{5.24}$$

$$f_T u^+ + g_T u^- + f_O w^+ + (1/2 - Le_O^{-1}\lambda_O) w^- = 0 \tag{5.25}$$

where

$$f_T = -B^+ + \left(1/2 + \lambda_T \coth(\lambda_T x_f)\right) / A^+$$

$$g_T = B^- - \left(1/2 + \lambda_T\right) / A^-$$

$$f_i = -1/2 + Le_i^{-1}\lambda_i \coth(\lambda_i x_f), \; i=F, O.$$

The six equations (5.20)-(5.25) form a homogeneous linear system whose solvability condition yields the dispersion relation

$$\begin{vmatrix} A^+ & -A^- & Le_F^{-1} & -Le_F^{-1} & 0 & 0 \\ A^+ & -A^- & 0 & 0 & Le_O^{-1} & -Le_O^{-1} \\ f_T & g_T & f_F & 1/2 - Le_F^{-1}\lambda_F & 0 & 0 \\ f_T & g_T & 0 & 0 & f_O & 1/2 - Le_O^{-1}\lambda_O \\ \frac{1-\gamma}{2} Le_F b_F A^+ & \frac{1+\gamma}{2} Le_F b_F A^- & \frac{1-\gamma}{2} b_F - 1 & 0 & 0 & \frac{1+\gamma}{2}\frac{Le_F}{Le_O} b_F \\ \frac{1-\gamma}{2} Le_O b_O A^+ & \frac{1+\gamma}{2} Le_O b_O A^- & \frac{1-\gamma}{2}\frac{Le_O}{Le_F} b_O & 0 & 0 & \frac{1+\gamma}{2} b_O - 1 \end{vmatrix} = 0 \tag{5.26}$$

The dispersion relation (5.26) relates the complex growth rate σ of the parameters describing the combustion system: the Damköhler number *Da*, the radiative loss, the Lewis numbers Le_F and Le_O, the initial mixture strength ϕ and the temperature difference ΔT.

5.3. Results and Discussion

5.3.1. Dual Extinction Limits

For the same reason as stated in Chapter 4, the radiative loss parameter, *Ra*, and Damköhler number, *Da*, need to be rescaled to a fixed reference state as

$$Da^* = (T_{\text{ref}}^2 / T_a)^3 \, Da_C \, \exp(-T_a / T_{\text{ref}})$$

$$Ra^* = 4\delta\sigma\kappa q^3 \lambda T_{\text{ref}}^4 / (\tilde{\rho}^2 c_p^5 \tilde{U}^2)$$

so that

$$Da = Da^* (T_f / T_{\text{ref}})^6 \exp[T_a (1/T_{\text{ref}} - 1/T_f)]$$

$$Ra = Ra^* (T_f / T_{\text{ref}})^4$$

where T_{ref} is the adiabatic flame temperature at the reference state with $Le_F = 1$, $Le_O = 1$, $\phi = 1$ and $\Delta T = 0$. The relevant parameters adopted are $T_a = 12.16$ and $T_{-\infty} = 0.152$. Because of the inverse dependence of both Ra^* and Da^* on the convection velocity $\tilde{U}$, the effect of radiative loss can be evaluated by defining a parameter $\Gamma = Ra^* / Da^*$ which represents the relative strength of the radiative loss to the chemical heat release [6]. Γ is independent of $\tilde{U}$ and for a fixed Γ, increasing Da^* (decreasing $\tilde{U}$) implies that Ra^* and hence the radiative loss increases at the same time. Thus, at large enough Da^*, radiative loss becomes dominant and leads to substantial reduction in the flame temperature and hence increased reactant leakage. This dependence of reactant leakage on Da^* is shown by the lower branch of the solutions in Fig. 5.2 for different values of Γ. The upper branch shows the opposite dependence on Da^* and thus is not physically realistic. The two solution branches form an isola for the $S_F \sim Da^*$ curve with two turning points instead of only one for the open C-shaped curve in the absence of radiative loss (see, for example, Fig. 4.4a). The turning point marked by "■" at smaller Da^* represents the kinetic extinction limit, $Da_{E,K}^*$, while that at larger Da^* marked by "▲" represents the radiative limit, $Da_{E,R}^*$. Burning is only possible when $Da_{E,K}^* < Da^* < Da_{E,R}^*$.

Figure 5.3 shows variations of the kinetic and radiative extinction Damköhler numbers with Γ for different Le_O. The upper and lower branches respectively represent the radiative and kinetic extinction limits. It is seen that the flammable range of Da^* diminishes with increasing Γ, and that burning is not possible when Γ exceeds a maximum value, Γ_{max}. Furthermore, this maximum loss decreases significantly with increasing Le_O, for which the flame sheet moves closer to the cold oxidant boundary, leading to lower flame temperatures. The flame is therefore weaker and as such is only able to sustain smaller radiative loss. For the same reason, increasing ϕ and decreasing ΔT play a similar role as increasing Le_O.

5.3.2. Onset of Near-Limit Oscillations

We note that without radiative loss, $A^{\pm} = 1$ and the dispersion relation (5.26) recovers to that of Kukuck & Matalon [1] for adiabatic diffusion flames, which has been shown to fail to have a solution as $Da^* \to \infty$ or $Le_F = Le_O = 1$, indicating that the flame is unconditionally stable under these circumstances. In the presence of radiative loss, however, we have shown in Figs. 5.2 and 5.3 that burning is only possible within a limited range of the Damköhler number, namely $Da^*_{E,K} < Da^* < Da^*_{E,R}$. Thus, the case $Da^* \to \infty$ does not exist for the present study. For a given set of prescribed parameters (Le_F = 2, Le_O = 1.6, ϕ = 1, ΔT = 0 and Γ = 2E-4), we solve from the dispersion relation (5.26) the complex growth rate, σ, for Da^* varying from $Da^*_{E,K}$ to $Da^*_{E,R}$. Its trace with Da^* is shown in Fig. 5.4. It is seen that with increasing Da^* from $Da^*_{E,K}$, σ moves from the positive Re(σ) side to the negative side crossing the imaginary axis at $Da^*_{C,K}$,

implying that the flame transits from the unstable to the stable state. However, unlike the adiabatic case [1], σ then moves back to the positive Re(σ) side with a very close trace, crossing the imaginary axis for the second time at $Da^*_{C,R}$. Since Im(σ) $\neq 0$ at the crossing points, two critical Damköhler numbers, $Da^*_{C,K}$ and $Da^*_{C,R}$, corresponding to the onset of flame oscillations near the kinetic and radiative extinction limits, respectively, are identified. The flame is unstable within the Damköhler number ranges $Da^*_{E,K} < Da^* < Da^*_{C,K}$ and $Da^*_{C,R} < Da^* < Da^*_{E,R}$. The critical Damköhler number $Da^*_{C,K}$ has been identified previously by Kukuck & Matalon [1] and Cheatham & Matalon [7]. The other critical Damköhler number, $Da^*_{C,R}$, identified here, indicates that the flame is also able to develop spontaneous oscillation near the radiation-induced extinction limit. The neutral stability points at $Da^*_{C,K}$ and $Da^*_{C,R}$ are marked by "□" and "Δ", respectively, on the $S_F \sim Da^*$ plot in Fig. 5.2. Consequently, steady burning is only possible for $Da^*_{C,K} < Da^* < Da^*_{C,R}$ when flame instability is considered.

Figure 5.5 shows variations of the extinction and critical Damköhler numbers with the radiative strength Γ. It is seen that with the consideration of flame instability, the Damköhler number range for steady burning contracts, leading to a smaller maximum radiative loss, Γ_{max}, the system can sustain. However the extent of contraction is rather small unless Γ is sufficiently close to Γ_{max}. From Fig. 5.5 we can expect that the normalized unstable ranges of the Damköhler number near both limits, namely $\Omega_K = \left(Da^*_{C,K} - Da^*_{E,K}\right)/Da^*_{E,K}$ and $\Omega_R = \left(Da^*_{E,R} - Da^*_{C,R}\right)/Da^*_{E,R}$, would exhibit a fast increase as Γ approaches Γ_{max}.

We now study the dependence of the unstable ranges of the Damköhler number on the prescribed parameters, such as Le_F, Le_O, ϕ and ΔT. Since radiative loss near the kinetic extinction limit has been shown to be relatively small [6] and the flame oscillation characteristics near this limit have been studied, hereafter only results for the near-radiative-limit oscillation will be presented. Figure 5.6 then shows the variations of Ω_R with Le_F for Le_O = 1, ϕ = 1, ΔT = 0 and different Γ's. It is seen that, as identified by Kukuck & Matalon [1] near the kinetic limit, flame oscillation near the radiative limit is also only possible within a restricted range of Le_F , and that the unstable range of Damköhler number Ω_R increases with increasing radiative loss Γ. Specifically, increasing Γ extends the upper limit of the unstable range of Le_F. However, it is important to note that Ω_R approaches zero as $Le_F \to 1$ whatever the value of Γ is, implying that flame oscillation is not possible for $Le_F \le 1$ and Le_O=1. Although not shown here, the same behavior exists for oscillation near the kinetic limit with the same set of parameters. This is contrary to results from previous investigations which showed that flame oscillation may develop under unity or sub-unity Lewis numbers when radiative loss is substantial [3-5, 8]. However, we have shown that radiative loss has two opposite effects on the heat transfer to either side of the reaction zone. Thus there exist certain parameters for which these two opposite effects cancel out so that radiative loss does not play the role of varying thermal diffusivity. This corresponds to the case of $A^{\pm} = 1$ so that the dispersion relation (5.26) degenerates to the one for adiabatic flame, from which the flame has been shown to be unconditionally stable for unity Lewis number [1]. From Eq. (5.13) the condition $A^{\pm} = 1$ yields the relationship $\phi^{-1}+2\Delta T$=1 for $Le_F = Le_O$=1. The parameters we used in Fig. 5.6 satisfy this condition as $Le_F \to 1$. Thus

we next plot the variation of Ω_R with Le_F for different Γ in Fig. 5.7 with a different set of parameters, $Le_O = 1$, $\phi = 1$ and $\Delta T = 0.1$, for which $A^{\pm} \neq 1$ so that the dispersion relation (5.26) may have solutions even when $Le_F = Le_O = 1$. It is then seen from Fig. 5.7 that flame oscillation may indeed develop for Le_F well below unity and the unstable range of Le_F is extended with increasing radiative loss, Γ. Thus, it can be concluded that the imbalance between the thermal and mass diffusions induced by radiative loss under unity Lewis numbers triggers flame oscillations near the radiative extinction limit. Consequently, the oscillatory instability near the radiative limit can still be considered to be thermal-diffusive in nature.

Figures 5.8a ~ 5.8c respectively show the variation of Ω_R with Le_F, ϕ and ΔT for different Le_O. It is seen from Fig. 5.8a that for a given Le_O instability only occurs within a limited range of Le_F, and this range can be extended well below Le_F=1 with increasing Le_O. Figure 5.8b shows that the unstable range of Damköhler number, Ω_R, increases monotonically with ϕ and this increase is significant before the dispersion relation (5.26) ceases to have a solution. This is because the maximum radiative loss, Γ_{max}, decreases significantly with increasing ϕ (and with increasing Le_O and decreasing ΔT). Thus, with increasing ϕ, Γ_{max} decreases rapidly toward the value of $\Gamma = 10^{-5}$ used in this figure, leading to a significant increase in Ω_R, as shown in Fig. 5.5. Since Γ_{max} also decreases with Le_O, this rapid increase in Ω_R with ϕ occurs at smaller ϕ for higher Le_O. Figure 5.8c shows that, for $Le_O = 1.2$, oscillation is only possible within a restricted range of ΔT. For Le_O = 1.4 and 1.6, the flame also shows the same tendency, although Ω_R increases rapidly with decreasing ΔT as it is sufficiently small. This rapid increase results from the

same reason as above. Furthermore, Fig. 5.8 shows that the unstable range of Damköhler number, Ω_R, increases monotonically with Le_O.

Lastly, it is shown in Fig. 5.4 that radiative loss only has very slight effect on the nondimensional oscillation frequency, $\mathrm{Im}(\sigma)$. However, in dimensional form the frequency is given by $f = \tilde{U}^2\,\mathrm{Im}(\sigma)/2\pi D_{th}$, where D_{th} is the thermal diffusivity. Since oscillation near the radiative limit occurs at relatively larger Da^* and hence smaller $\tilde{U}$, the oscillation frequency near the radiative limit should be smaller than that near the kinetic limit. This is consistent with the numerical results of Christiansen *et al.* [3].

5.4. Conclusions

We have performed a linear stability analysis on flame oscillation with radiative heat loss in one-dimensional chambered diffusion flames using large-activation-energy asymptotics. Oscillatory instability near the *radiation-induced* extinction limit is identified, in addition to the one near the kinetic limit that has been identified previously. Thus, flame oscillation is also possible when the Damköhler number is sufficiently large, and steady burning is only possible if the Damköhler number falls within the two critical values corresponding to the marginally stable states near the kinetic and radiative limits, respectively.

It is also shown that although flame oscillation near the radiative limit may develop under unity Lewis number, this oscillatory instability is still thermal-diffusive in nature. This is because radiative loss plays a similar role as varying the thermal diffusivity of the reactants. Thus, the thermal and mass diffusion of the reactants may not be balanced even for unity Lewis number. This imbalance leads to intrinsic flame

oscillation near flame extinction. Radiative heat loss, however, also affects flame stability through the total excess enthalpy $(1+\gamma)h_O/2+(1-\gamma)h_F/2$ in Eq. (5.12), which comes from the imbalance of thermal and mass diffusion as the reactants leak through the reaction zone, as well as from radiative loss. It is known that oscillatory instability is characterized by the negative total excess enthalpy [9] whose value decreases with radiative loss. Thus with increasing radiative loss, the negative total excess enthalpy and hence flame oscillation can be achieved over a wider parameter range.

The extinction analysis has shown that there is a maximum radiative loss for a combustion system to sustain, above which burning is impossible. As radiative loss approaches this maximum value, the unstable ranges of Damköhler number near both extinction limits increase dramatically. As radiative loss is sufficiently smaller than this maximum value, the unstable range of Damköhler numbers near the radiative extinction limit Ω_R shows similar parametric dependence on Le_F, Le_O and ϕ to that near the kinetic limit, namely it increases monotonically with Le_O and ϕ and flame oscillation is only possible within a restricted range of Le_F. However, flame oscillation near the radiative limit is only possible within a limited range of ΔT. This is different from the near-kinetic-limit oscillation that the unstable range of Damköhler numbers decreases with increasing ΔT.

Lastly, we note that radiative loss shows only small effects on the nondimensional frequency of flame oscillation near both extinction limits. However, since the nondimensionalization uses the diffusion time scale and since the radiation-induced extinction occurs at relatively larger Damköhler numbers and hence smaller diffusion

times, the dimensional oscillation frequency near the radiative limit is found to be smaller than that near the kinetic limit.

References

1. Kukuck, S. and Matalon, M., *Combust. Theory Modelling* **5**: 217-240 (2001).
2. Liñán, A., *Acta Astronautica* **1**: 1007-1039 (1974).
3. Christiansen, E. W., Tse, S. D. and Law, C. K., *Combust. Flame* **134**: 263-278 (2003).
4. Sohn, C. H., Kim, J. S., Chung, S. H. and Maruta, K., *Combust. Flame* **123**: 95-106 (2000).
5. Miklavčič, M., Moore, A. B. and Wichman, I. S., *Combust. Theory Model.* **9**: 403-416 (2005).
6. Chao, B. H., Law, C. K., T'ien, J. S., *Proc. Combust. Inst.* **23**: 523–531 (1990).
7. Cheatham, S. and Matalon, M., *J. Fluid Mech.* **414**: 105-144 (2000).
8. Cheatham, S. and Matalon, M., *Proc. Combust. Inst.* **26**: 1063-1070 (1996).
9. Matalon, M., *Ann. Rev. Fluid Mech.* **39**: 163-191 (2007).

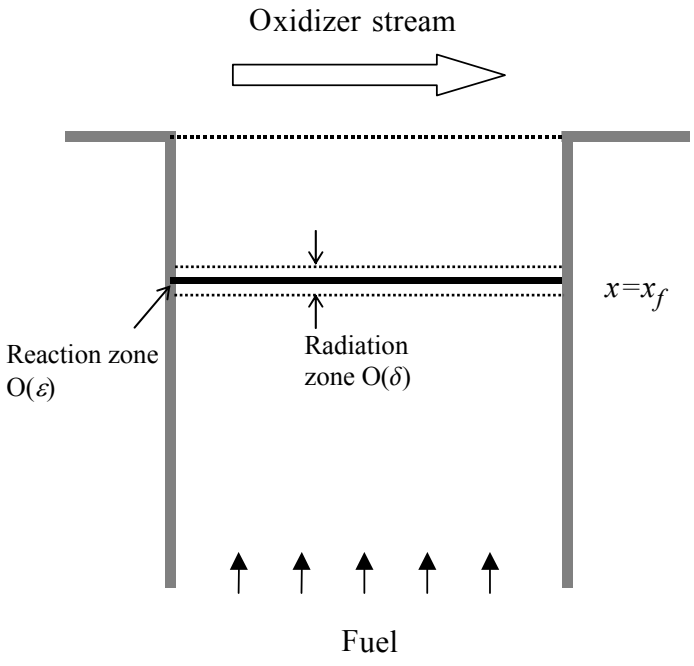

Figure 5.1. The one-dimensional flame configuration.

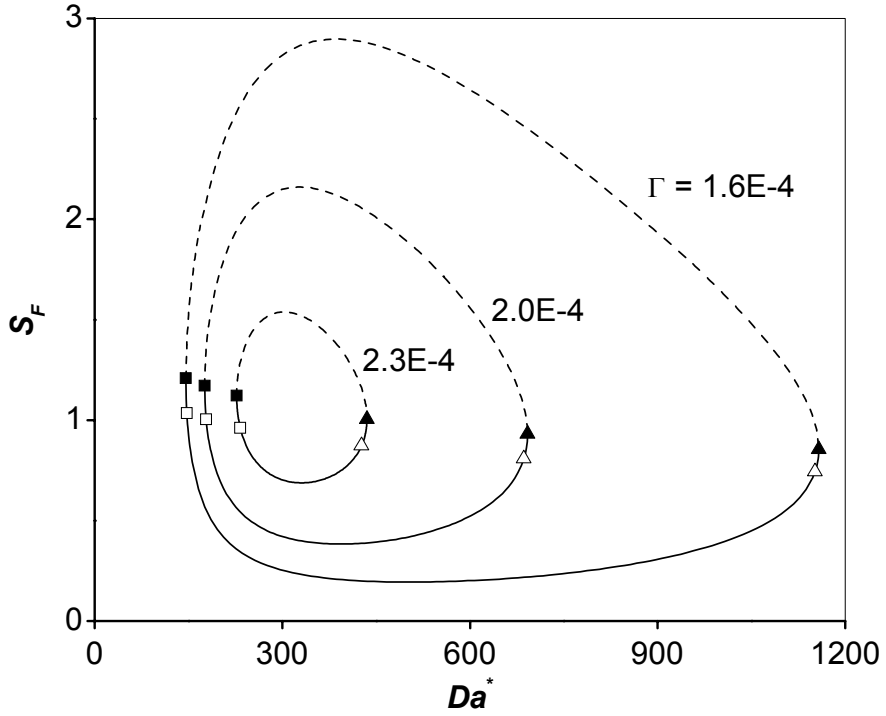

Figure 5.2. Fuel leakage S_F versus Da^* for different Γ with the kinetic (■) and radiative (▲) extinction limits as well as the neutral stability points (□ and Δ) (with $Le_F = 2$, $Le_O = 1.6$, $\phi = 1$ and $\Delta T = 0$).

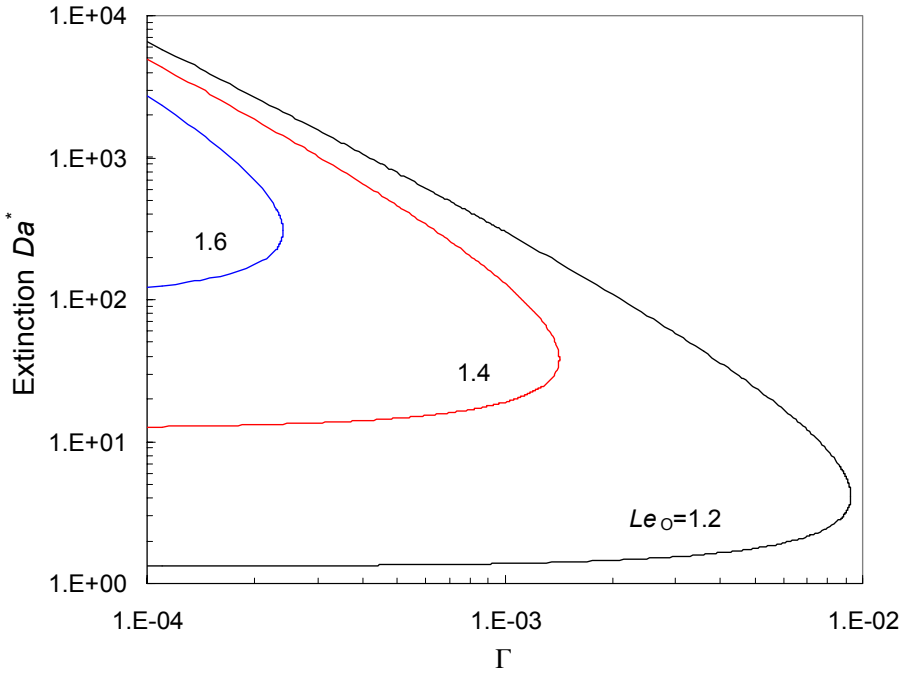

Figure 5.3. Extinction Damköhler numbers versus Γ for different Le_O (with $Le_F = 2$, $\phi = 1$ and $\Delta T = 0$). The upper branch represents the radiative extinction limit and lower branch the kinetic limit.

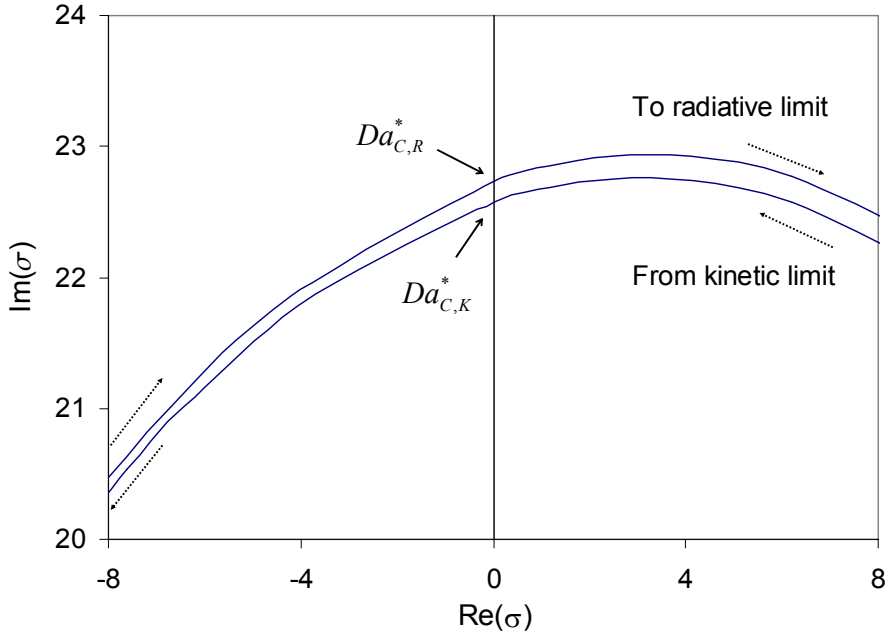

Figure 5.4. Trace of the complex growth rate σ with Da^* from $Da^*_{E,K}$ to $Da^*_{E,R}$ (with Le_F = 2, Le_O = 1.6, ϕ = 1, ΔT = 0 and Γ = 2.E-4).

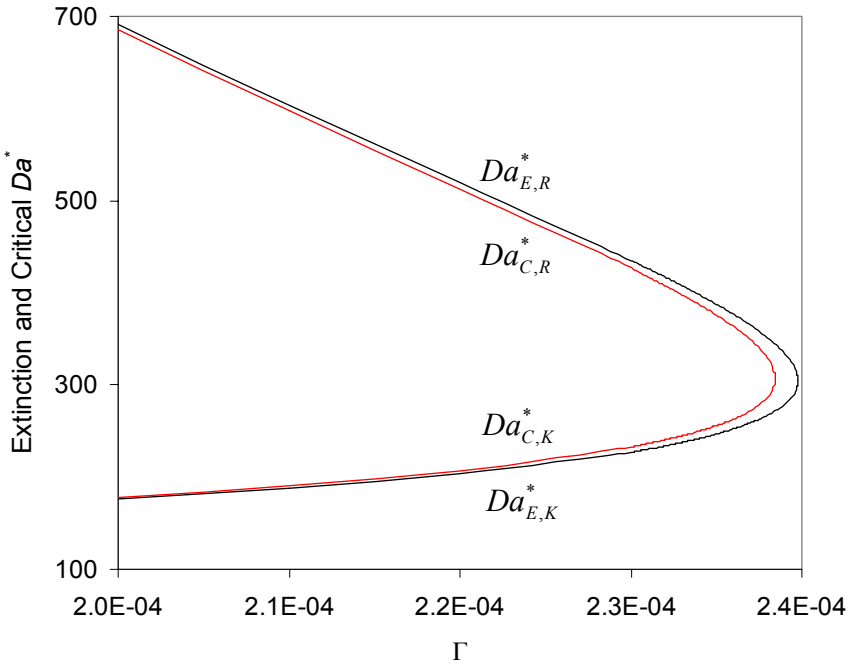

Figure 5.5. Extinction and critical Damköhler numbers versus Γ (with $Le_F = 2$, $Le_O = 1.6$, $\phi = 1$ and $\Delta T = 0$).

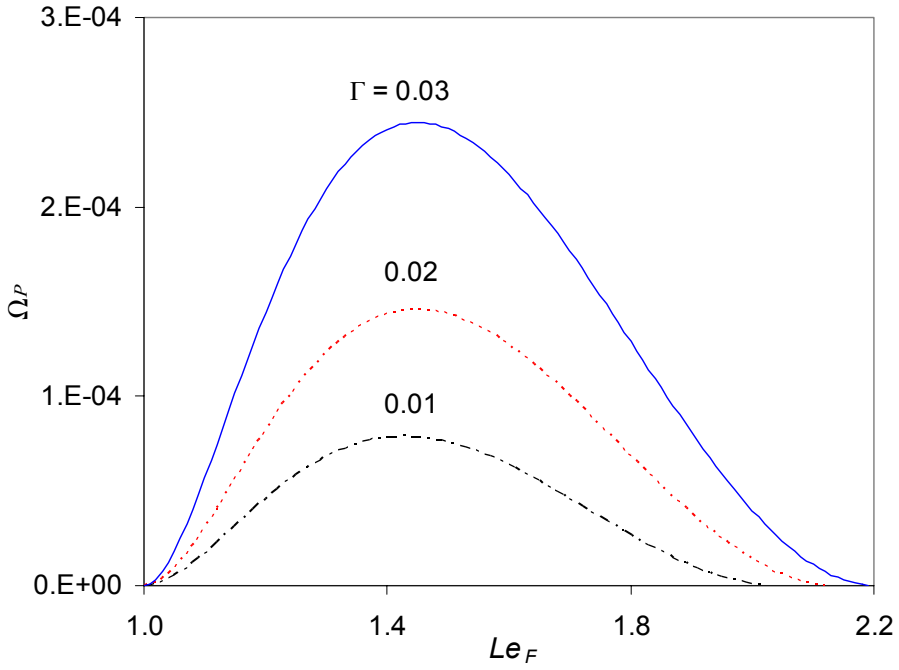

Figure 5.6. Normalized unstable range of Damköhler number for flame oscillations near the radiative extinction limit versus Le_F for different Γ (with $Le_O = 1$, $\phi = 1$ and $\Delta T = 0$).

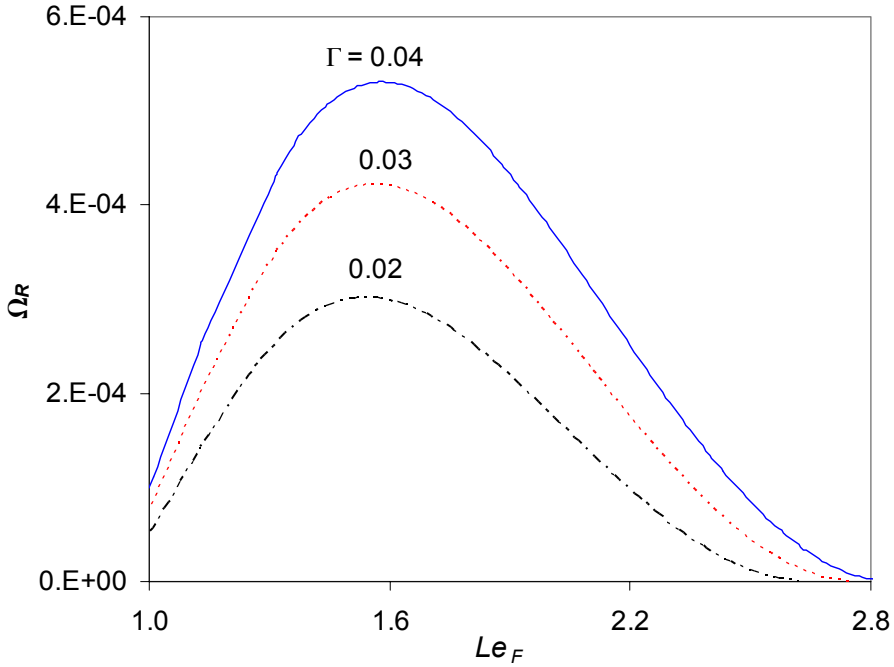

Figure 5.7. Normalized unstable range of Damköhler number for flame oscillations near the radiative extinction limit versus Le_F for different Γ (with $Le_O = 1$, $\phi = 1$ and $\Delta T = 0.1$).

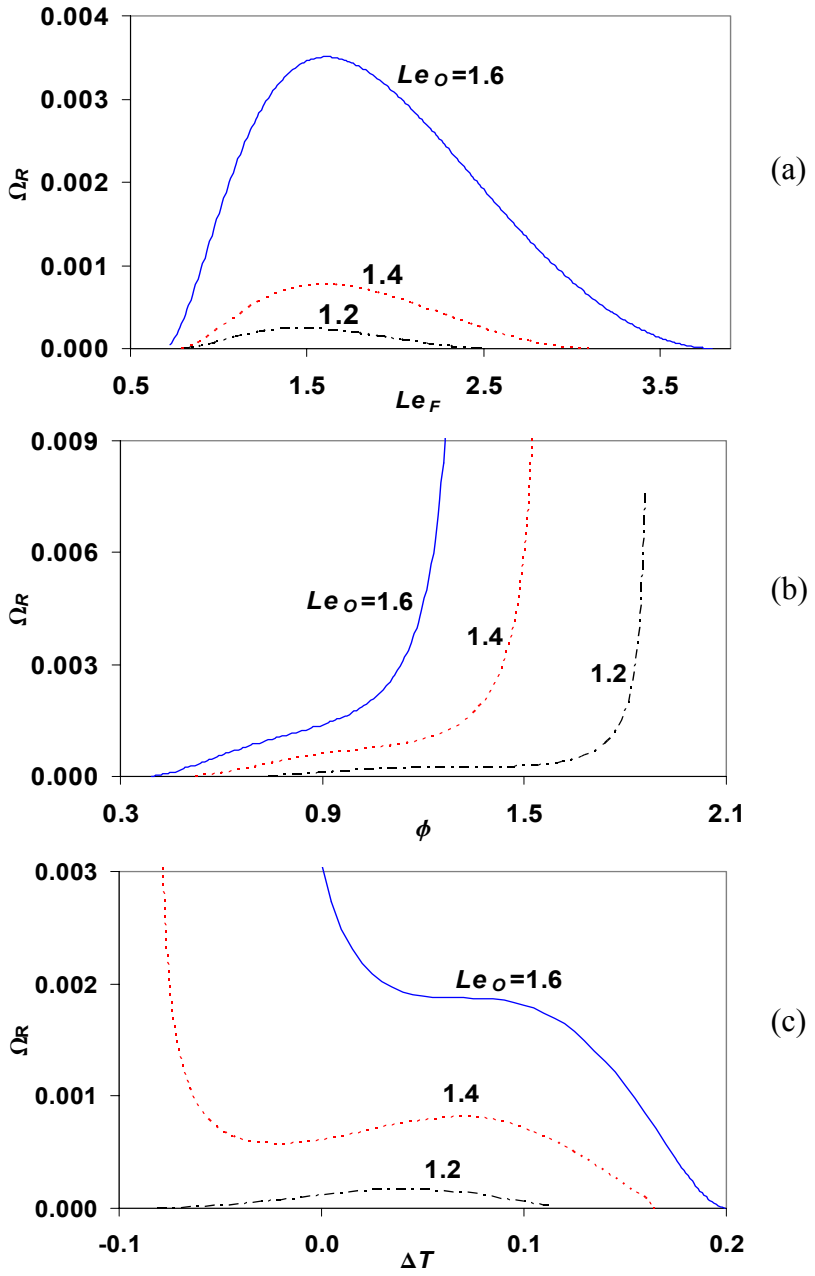

Figure 5.8. Normalized ranges of Damköhler number for flame oscillations near the radiative limit (a) versus Le_F with $\phi = 1$, $\Delta T = 0$ and Γ = 1.E-4, (b) versus ϕ with $Le_F = 2$, $\Delta T = 0$ and Γ = 1.E-5, and (c) versus ΔT with $Le_F = 1$, $\phi = 1$ and Γ = 1.E-4, for different Le_O.

Chapter 6: Linear Response of Stretch-Affected Premixed Flames to Flow Oscillations

6.1. Background

In this chapter we study the response of premixed flames to flow oscillations. This problem is of particular interest because it constitutes the key elementary process in the development of the thermo-acoustic instability. In particular, the Rayleigh criterion [1] can be described by the phenomenological inequality

$$\iint p'(x,t)q'(x,t)dvdt > \iint \Phi(x,t)dvdt$$

where p' are q' are the perturbations in pressure and heat release, respectively, Φ is the acoustic energy dissipation, and the integral is over a period of oscillation and the combustor volume. This inequality implies that thermo-acoustic instability occurs only when the heat release perturbation is in phase with the flow perturbation and at the same time possesses sufficiently large amplitude to overcome the dissipation process. Thus, it is essential to determine the response of heat release rate to the flow perturbations. There has been a number of work addressing this problem. However, as reviewed in the Introduction, these analyses assumed constant flame speed that is independent of flame stretch, and as such, are not adequate to study the flame response at high frequencies where the curvature of flame wrinkles becomes relatively large. In addition, flame stretch is also believed to be responsible for the observed damping of perturbation-induced flame wrinkling [2]. Thus, variations in stretch-induced flame speeds are able to affect

the heat release rate not only through the change of local burning rate, but also through the modulations of flame surface area. Thus, the objective of this chapter is to study the role of flame stretch through the curvature of the flame wrinkles on the premixed flame response to flow oscillations. This is further motivated by the recognition that studies since the 1980s have conclusively identified the essential and significant influence of stretch on the response of both premixed and diffusion flames [3]. The influence is further augmented in the presence of nonequidiffusion because of the associated modification of the flame temperature. Since the present phenomena involve flame wrinkling at various scales, it behooves us to assess how and to what extent they are affected by stretch and nonequidiffusion. We shall subsequently show that such an influence is indeed significant and as such needs to be accounted for in the analyses of combustion instability.

In the following we shall first report some experimental results for the damping phenomenon of the perturbation-induced wrinkling, and show that these observations are consistent with the concept of stretch. These results are adapted from our collaboration work with Professor Lieuwen of the Georgia Institute of Technology. We shall then present the theoretical analysis, yielding appropriate nondimensional parameters and assessments of the flame response.

6.2. Experimental Observations

In this section, we present flame images of the "filtering" phenomenon. These images were obtained with a 2.54 cm diameter Bunsen burner, previously described in Rajaram and Lieuwen [4]. Acoustic oscillations were excited with a loudspeaker placed at the

bottom of the burner tube. The flame was stabilized with a methane-fueled (ϕ = 1.15) annular pilot.

Experiments were performed with two fuels, methane and propane, which are respectively thermal-diffusively stable under rich and lean conditions when subjected to spatial perturbations through the action of stretch [3], and unstable otherwise. The controlling Lewis numbers (*Le*) for the stable and unstable cases are respectively greater and smaller than unity, with methane being only weakly nonequidiffusive because its *Le* deviates just slightly from unity.

Figure 6.1 shows images of the lean and rich methane flames under perturbations of similar frequencies. It is seen that while the wrinkling decays in the downstream direction for the rich flame, it persists for the lean flame. Figure 6.2 shows images of two lean propane flames, with the frequency of the right image being twice that of the left, resulting in wrinkles with smaller and larger wavelengths, respectively. It is seen that while the wrinkles persist along the flame front for the smaller frequency, similar to previous observations [2], they decay rather rapidly for the larger frequencies. The latter situation, apparently, is the "filtering" phenomenon reported by Bourehla & Baillot [2].

The above observations demonstrate the two crucial parameters governing the evolution of the imposed wrinkles on the flame surface, namely curvature-induced stretch coupled through the action of mixture nonequidiffusion, and the frequency of the perturbation. In particular, Fig. 6.1 shows that, when the mixture is thermal-diffusively more stable as characterized by a larger Lewis number for the rich methane flame, the wrinkles are smoothed more rapidly as they propagate downstream along the flame surface. In addition, Fig. 6.2 shows that, for the thermal-diffusively stable lean propane

flames, the efficiency of stabilization is also promoted with decreasing wavelength and thereby increasing curvature of the wrinkles. These suggest that the fundamental mechanism governing the persistence or decay of the imposed wrinkles is that of stretch in the presence of mixture nonequidiffusion. We now present an analysis that quantitatively describes this phenomenon.

6.3. Theoretical Analysis

6.3.1. Basic Considerations

Under a harmonic perturbation velocity field, $u'(\mathbf{x},t)$, the flame surface oscillates around its steady-state position. This leads to fluctuations of the heat release rate that may couple to the perturbation field, resulting in oscillations with either growing or decaying amplitude. Thus the basic problem of interest is to determine the response of the flame position, $\zeta(\mathbf{x},t)$, and the heat release rate of the flame, to a given $u'(\mathbf{x},t)$. The global heat release rate of the flame is then given by

$$Q(t) = \int \rho_u s_u q dA \tag{6.1}$$

where ρ_u is the density of the unburned mixture, s_u the local flame speed, q the heat release per unit mass of the reactant, and the integral is over the entire flame surface area, A. Equation (6.1) shows that there exist three fundamentally different sources of generating heat release perturbations in a premixed flame, namely perturbations in the mass burning rate, $\rho_u s_u$, the heat of reaction, q, and the flame surface area, A.

Since we are primarily interested in the flame response to flow perturbations, we assume constant q and ρ_u; analyses of the effects of these two sources of perturbation through fluctuations in the mixture composition and pressure are given in Cho &

Lieuwen [5] and McIntosh [6], respectively. It is noted that although a velocity perturbation that is acoustic in origin is accompanied by a pressure perturbation, their relative impacts differ greatly, on the order of the Mach number of the flame speed. As such, our subsequent calculations focus on the quantity:

$$\frac{Q'}{\overline{Q}} = \frac{\int s_u' d\overline{A}}{\int \overline{s}_u d\overline{A}} + \frac{A'}{\overline{A}} \tag{6.2}$$

in the linear limit, where the overbar and prime respectively denote the steady-state and disturbed values. The response of the flame to the flow perturbation is then evaluated by the transfer function, defined as the ratio of the normalized fluctuation of the heat release rate to that of the flow velocity:

$$G = \frac{\left(Q'/\overline{Q}\right)}{\left(u'/u_o\right)} \tag{6.3}$$

where u_o is the mean flow velocity. This transfer function consists of contributions from the perturbation to both the flame speed and flame surface area, which are expected to be also coupled since variations in the flame speed would cause corresponding variations in the shape of the wrinkles and hence the flame surface area. This is to be contrasted to previous studies [7-12] in which the transfer function is only affected by fluctuations of the flame surface area because the flame speed is assumed to be constant.

6.3.2. Modeling Approach

Figure 6.3 illustrates the geometry considered in the analysis, which is a two-dimensional wedge flame stabilized by a bluff body. The streamwise and transverse dimensions of the flame are given by the flame length, L_f, and its half width, W, without imposed perturbation. The instantaneous flame-sheet location at the transverse location, y, is given

by $x = \zeta(y,t)$ and is assumed to be a single-valued function of y.

The analytical approach used here closely follows that of Baillot *et al.* [7] and Fleifel *et al*. [8]. The flame dynamics are modeled with the front tracking equation [3, 13]:

$$\frac{\partial \zeta}{\partial t} = u - v\frac{\partial \zeta}{\partial y} - s_u\sqrt{1+\left(\frac{\partial \zeta}{\partial y}\right)^2} \tag{6.4}$$

where u and v denote the streamwise and transverse components of the flow velocity, respectively.

The flame speed can be expressed as [14]

$$s_u / s_u^o = 1 - \ell_{\mathrm{D}}\nabla\cdot\mathbf{n} + \frac{\beta}{2}\left(\frac{1}{Le}-1\right)\ell_{\mathrm{D}}\frac{\kappa}{s_u^o} \tag{6.5}$$

where s_u^o is the constant, planar laminar flame speed, $\mathbf{n}$ the local normal on the flame front pointing toward the unburned mixture, ℓ_{D} the thermal thickness of the flame, β the Zel'dovich number, and κ the flame stretch rate given by

$$\kappa = -\mathbf{n}\cdot\nabla\times(\mathbf{v}\times\mathbf{n}) + (\mathbf{V}\cdot\mathbf{n})(\nabla\cdot\mathbf{n}) \tag{6.6}$$

where $\mathbf{v} = (u, v)$ is the flow velocity at the flame front on the unburned side and $\mathbf{V} = d\mathbf{x}/dt$ the local velocity of the flame front. We shall limit our study to the case of weak stretch, namely small ℓ_{D}/L_f, and assume $\beta(Le^{-1}-1) \sim O(1)$. It is seen from the second and third terms of Eq. (6.5) that the modification of the flame speed by stretch is given by the sum of the pure curvature effect and the nonequidiffusion-related stretch effect.

The flow is assumed to be purely streamwise, i.e. $v = 0$. Then, the mean streamwise velocity u_o is related to the laminar flame speed, s_u^o, by

$$\frac{u_o}{s_u^o} = \sqrt{1 + \left(\frac{L_f}{W}\right)^2} \tag{6.7}$$

where the ratio of the flame length to its half width, $\chi = L_f/W$, plays an important role in the flame dynamics.

Following previous studies [7, 8], we assume that the flame remains anchored at the base, i.e.

$$\zeta(y = 1, t) = 0 \tag{6.8}$$

For wedge flames, the second boundary condition comes from the requirement that all information should flow out of the flame. This is a rigorous way of capturing the fact that the flame tail is free to move around (see Fig. 6.3), i.e.

$$\frac{\partial^2 \zeta(y = 0, t)}{\partial y^2} = 0 \tag{6.9}$$

The reason that we adopted the 2D wedge flame for analysis, instead of the axisymmetric conical flame used in the experiment, is because the axisymmetric wedge flame, as well as the 2D and axisymmetric conical flames, are not analytically solvable due to the extra curvature term associated with the bulk flame. Since our primary interests in the present study are to identify the critical scales of the imposed perturbation for stretch to be effective, and the mechanism for the self-damping of the flame wrinkles, the 2D wedge configuration offers a convenient platform to identify the controlling physics, as will be demonstrated subsequently. Furthermore, it is reasonable to expect, and we have numerically verified, that the flame responses for the 2D wedge and conical flames not only are qualitatively similar but are also quantitatively very close, with the only difference being the very small contribution from the tip region of the conical flame.

6.3.3. Velocity Field and Nondimensionalization

Experimental studies have clearly shown that the perturbation velocity field can exhibit a variety of characteristics, including both acoustic and vortical components, which in the latter case exhibits phase variation over a convective wavelength, u_o/f [15], where f is the perturbation frequency. By incorporating this convective phase variation into the perturbation velocity field, Schuller *et al.* [15] showed that the modeled flame area response agrees quite well with their data. As such, we assume the perturbation field to have an arbitrary phase speed so that the velocity field is specified as

$$u(\zeta,t) = u_o + u' e^{i(k\zeta - \omega_o t)} \tag{6.10}$$

where u' and ω_o respectively denote the amplitude and angular frequency of the velocity perturbation, and k is the convective wave number, defined as:

$$k = \frac{\omega_o}{u_c} = \left(\frac{u_o}{u_c}\right)\left(\frac{\omega_o}{u_o}\right) = \alpha\left(\frac{\omega_o}{u_o}\right) \tag{6.11}$$

where u_c is the phase speed of the perturbation, and $\alpha = u_o/u_c$ denotes the ratio of the mean flow velocity to the phase speed of the perturbation.

Hereafter, the variables t, y, ℓ_D, u and ζ are nondimensionalized by L_f/u_o, W, W, u_o and L_f, respectively. The nondimensional front tracking equation is then given by

$$\frac{\partial \zeta}{\partial t} = u - \left(\frac{s_u}{s_u^o}\right)\sqrt{\frac{1+\chi^2\left(\frac{\partial \zeta}{\partial y}\right)^2}{1+\chi^2}} \tag{6.12}$$

and the nondimensional velocity field can be written as

$$u(\zeta,t) = 1 + \varepsilon e^{iSt(\alpha\zeta - t)} \tag{6.13}$$

where

$$St = \frac{\omega_o L_f}{u_o} \tag{6.14}$$

is the Strouhal number and $\varepsilon = u'/u_o$.

The purely streamwise velocity field assumed in this study renders a divergence-free perturbation field for $\alpha = 0$, but in general not for $\alpha \neq 0$. While extending the current model to include a transverse velocity component in order to have a divergence-free perturbation field for the $\alpha \neq 0$ case is straightforward, it renders the resulting algebra quite tedious and does not contribute additional essential insight into the physics of the problem, at least at the level considered herein. It is emphasized that our goal here is not to simulate the exact perturbation field of a particular experimental setup, but rather to elucidate the key physical processes and the nondimensional parameters that influence the flame dynamics.

6.4. Results and Discussion

6.4.1. Solutions of Flame Perturbation and Transfer Function

In this section, we derive the expressions for the location of the disturbed flame and the transfer function when the flame speed is affected by stretch.

In response to the velocity perturbation, the flame position can be expanded as:

$$\begin{aligned} \zeta(y,t) &= \zeta_o(y) + \zeta'(y,t) \\ \zeta'(y,t) &= \varepsilon\zeta_1(y)e^{-iSt\cdot t} + O(\varepsilon^2) \end{aligned} \tag{6.15}$$

where

$$\zeta_o(y) = 1 - y \tag{6.16}$$

is the steady-state flame location. Substituting Eqs. (6.15) and (6.16) into Eq. (6.5), the flame speed relation can be expressed as:

$$\frac{s_u}{s_u^o} = 1 - \frac{\sigma_C \chi \zeta'_{yy}}{\left(1+\chi^2\right)^{3/2}} + \frac{\sigma_S \chi}{\left(1+\chi^2\right)^{1/2}} \frac{\partial u}{\partial x}\bigg|_{x=\zeta} \tag{6.17}$$

where the subscript "y" denotes the spatial derivative with respect to y, and

$$\sigma_C = \left[1 - \frac{\beta}{2}\left(\frac{1}{Le} - 1\right)\right]\left(\frac{\ell_D}{W}\right) \tag{6.18}$$

$$\sigma_S = \frac{\beta}{2}\left(\frac{1}{Le} - 1\right)\left(\frac{\ell_D}{W}\right) \tag{6.19}$$

are the Markstein numbers related to the curvature and strain sensitivities of the flame speed, respectively. Recognizing that the curvature of the flame front can be expressed as $\zeta'_{yy}/\left(1+\chi^2\right)^{3/2}$, Eq. (6.17) shows that, in the linear limit, the individual contributions from the flame curvature and strain have been separated out, as respectively represented by the second and third terms on its RHS. Furthermore, it is seen from Eq. (6.18) that, as noted earlier, the flame speed is modified by the curvature through a pure curvature effect, which is independent of *Le*, and the curvature component of the nonequidiffusion-related stretch. Consequently, the nonequidiffusional effect tends to strengthen the pure curvature effect when $Le > 1$, and weakens it when $Le < 1$. We further note that alternate expressions for the stretch-affected flame speed exist, such as that of Matalon & Matkowsky [16]. However, once expanded in terms of the flame position and flow speed, they can be expressed in the same form as Eq. (6.17). The differences are lumped into the detailed expressions for the Markstein numbers, σ_C and σ_S. In this paper we shall study the effects of flame stretch on the flame response by employing different values of σ_C and σ_S, which provide a direct interpretation of their respective influences on the flame

response. Thus, the present analysis is not restricted by the specific expression for the stretch-affected flame speed, and as such is general in nature. We shall, however, restrict our investigation to positive values of σ_C, since we are interested in curvature-induced damping. Thus the mixtures of interest here are either diffusionally stable or mildly unstable, which respectively conform with the experimental situations of Figs. 6.2 and 6.1.

Substituting Eqs. (6.15)-(6.17) into Eq. (6.12) and collecting $O(\varepsilon)$ terms, the evolution equation for the disturbed flame location ζ_1 can be derived as

$$\frac{\sigma_C \chi}{(1+\chi^2)^{3/2}}\frac{\partial^2 \zeta_1}{\partial y^2}+\frac{\chi^2}{1+\chi^2}\frac{\partial \zeta_1}{\partial y}+iSt\zeta_1+\left(1-\frac{i\sigma_S \alpha St\chi}{\sqrt{1+\chi^2}}\right)e^{iSt\alpha(1-y)}=0 \tag{6.20}$$

The solution of Eq. (6.20), subject to the boundary conditions in Eqs. (6.8) and (6.9), is

$$\zeta_1(y)=Ae^{L_1 y}+Be^{L_2 y}+Ce^{iSt_f\hat{\alpha}(1-y)} \tag{6.21}$$

where

$$L_{1,2}=\frac{1}{2\hat{\sigma}_C}\left(-1\pm\sqrt{1-4i\hat{\sigma}_C St_f}\right), \qquad A=-\frac{C\left(L_2^2+St_f^2\hat{\alpha}^2e^{L_2+iSt_f\hat{\alpha}}\right)}{L_2^2e^{L_1}-L_1^2e^{L_2}}$$

$$B=\frac{C\left(L_1^2+St_f^2\hat{\alpha}^2e^{L_1+iSt_f\hat{\alpha}}\right)}{L_2^2e^{L_1}-L_1^2e^{L_2}}, \qquad C=-\frac{1}{iSt}\left(\frac{1-i\hat{\sigma}_S St_f\hat{\alpha}}{i\hat{\sigma}_C St_f\hat{\alpha}^2-\hat{\alpha}+1}\right)$$

$$St_f=St\frac{1+\chi^2}{\chi^2}, \qquad \hat{\alpha}=\alpha\frac{\chi^2}{1+\chi^2} \tag{6.22, 6.23}$$

$$\hat{\sigma}_C=\frac{\sigma_C}{\chi\left(1+\chi^2\right)^{1/2}}, \qquad \hat{\sigma}_S=\frac{\sigma_S\chi}{\left(1+\chi^2\right)^{1/2}} \tag{6.24, 6.25}$$

In the above St_f, referred to as the reduced Strouhal number, combines effects of the flame aspect ratio and the Strouhal number, and can be rewritten as

$\omega_o (L_f/\cos\theta)/(u_o \cos\theta)$, where θ is the angle between the flame surface, without perturbation, and the flow direction. Thus it represents the angular frequency of the perturbation normalized by the time taken for the flame perturbation to propagate the flame length.

Recognizing that in the limit of weak stretch, i.e. $\hat{\sigma}_C \to 0$ and $\hat{\sigma}_S \to 0$, we have $L_2 \to -\infty$, $e^{L_1} >> e^{L_2}$ and $e^{L_1 y} >> e^{L_2 y}$ except for the region very near the flame tail ($y \to 0$), Eq. (6.7) can be simplified to

$$\zeta_1 = C\left[-e^{L_1(y-1)} + e^{i\hat{\omega}St_f(1-y)}\right] \tag{6.26}$$

Figure 6.4 shows the transverse distribution of the amplitude of the flame oscillation, $|\zeta_1(y)|$, from the exact and approximate solutions, (6.21) and (6.26), respectively, for different values of $\hat{\sigma}_C$. It is seen that the solutions agree well for $\hat{\sigma}_C$ up to 0.2, which is a rather large value, even near the flame tail region where $e^{L_1 y} >> e^{L_2 y}$ is not closely satisfied. Furthermore, they only show very small difference at the flame tail even for $\hat{\sigma}_C = 0.5$. Thus, hereafter we shall present the analysis based on the simpler solution, Eq. (6.26).

Next, we consider the total heat release of the flame. Since, by considering flame stretch, the heat release responds to the perturbation through both the flame surface area and flame speed, fluctuations of the heat release can be expressed as $Q' = Q'_A + Q'_S$ in the linear limit, where

$$Q'_S = \int s'_u d\overline{A}\,, \qquad Q'_A = \int \overline{s}_u dA' \tag{6.27}$$

are consequences of the fluctuations of the flame speed and flame surface area, respectively, and

$$d\overline{A} = \left(1+\chi^2\right)^{1/2} dy \tag{6.28}$$

$$dA' = -\frac{\chi^2}{\left(1+\chi^2\right)^{1/2}} \frac{\partial \zeta'}{\partial y} dy \tag{6.29}$$

$$s'_u = -\frac{\sigma_C \chi \zeta'_{yy}}{\left(1+\chi^2\right)^{3/2}} + \frac{\sigma_S \chi}{\left(1+\chi^2\right)^{1/2}} \left.\frac{\partial u}{\partial x}\right|_{x=\zeta} \tag{6.30}$$

Substituting equations (6.13), (6.16) and (6.28)-(6.30) into Eq. (6.27), and then into Eq. (6.3), yields

$$G_S = -\left\{\frac{\hat{\sigma}_C \chi^2}{1+\chi^2}\left[\frac{\partial \zeta_1(y=1)}{\partial y} - \frac{\partial \zeta_1(y=0)}{\partial y}\right] + \hat{\sigma}_S\left(1-e^{iSt_f\hat{\alpha}}\right)\right\} \tag{6.31}$$

$$G_A = \frac{\chi^2}{1+\chi^2}\zeta_1(y=0) \tag{6.32}$$

where $G_S = \left(Q'_S/\overline{Q}\right)/\left(u'/u_o\right)$ and $G_A = \left(Q'_A/\overline{Q}\right)/\left(u'/u_o\right)$ are the transfer functions contributed from fluctuations of the flame speed and flame surface area, respectively. The overall transfer function is then given by $G = G_S + G_A$, which depends on four key parameters: St_f, $\hat{\alpha}$, $\hat{\sigma}_C$ and $\hat{\sigma}_S$.

6.4.2. Baseline Flame Response

Since the influence of stretch on the flame response to perturbations should be assessed based on comparisons between results with and without stretch, we shall first present the baseline flame response characteristics for the unstretched flame. For this case, the transfer function is only contributed from fluctuations of the flame surface area. With $\hat{\sigma}_C = \hat{\sigma}_S = 0$, Eq. (6.26) becomes

$$\zeta_1 = i\frac{e^{iSt_f(1-y)} - e^{i\hat{\alpha}St_f(1-y)}}{(\hat{\alpha}-1)St} \tag{6.33}$$

As indicated in Boyer & Quinard [17], Eq. (6.33) shows that the shape of the flame front results from the conjugating action of the wrinkles convected along the flame induced by the flow oscillation at the flame base, $e^{iSt_f(1-y)}$, and those locally induced by the flow nonuniformity, $e^{i\hat{\alpha}St_f(1-y)}$. Figure 6.5 shows the transverse distribution of the amplitude of the flame oscillation, $|\zeta_1|$, for the unstretched flame with different $\hat{\alpha}$. It is seen that depending on the value of St_f and $\hat{\alpha}$, the convective and locally induced wrinkling may superimpose constructively ($0<\hat{\alpha}<2$) or destructively ($\hat{\alpha}>2$), leading to larger or smaller amplitude of flame oscillation, respectively, in comparison with the case of uniform velocity perturbation ($\hat{\alpha}=0$). In particular, $\hat{\alpha}=1$ corresponds to the exact coincidence of the convective wrinkling and the locally induced wrinkling. In this case, the local flow nonuniformity acts on the flame in a similar manner as resonance, as shown by Eq. (6.20) with $\sigma_C=\sigma_S=0$ and $\hat{\alpha}=1$, leading to a much larger oscillation amplitude that is only a function of y and is independent of St_f.

Substituting Eq. (6.33) into Eq. (6.32) yields the transfer function

$$G=i\frac{e^{iSt_f}-e^{i\hat{\alpha}St_f}}{(\hat{\alpha}-1)St_f} \tag{6.34}$$

with the gain given by

$$|G|=2\left|\frac{\sin\frac{1}{2}(\hat{\alpha}-1)St_f}{(\hat{\alpha}-1)St_f}\right| \tag{6.35}$$

Figure 6.6a shows the dependence of the gain of the transfer function, $|G|$, on St_f for different $\hat{\alpha}$. It is seen that the gains are always less than unity (except for the $\hat{\alpha}=1$ case) and exhibit a series of peaks and nodes. In particular, the nodes in the gain occur at

frequencies satisfying $\left|\hat{\alpha}St_f - St_f\right| = 2n\pi$, (n=0,1,2…). The gains for the $\hat{\alpha} = 0$ and $\hat{\alpha} = 2$ cases are identical, which is anticipated from the $\hat{\alpha}$ dependence of the gain in Eq. (6.35). In the limit of $\hat{\alpha} \to 1$, Eq. (6.34) can be reduced to $G_{\hat{\alpha}\to 1} = e^{iSt_f}$, leading to a constant, unity gain irrespective of the value of St_f. As we have just discussed and also shown in Eq. (6.34), the above characteristics for the gain of the transfer function is a consequence of the superposition of the convective wrinkling and the wrinkling locally induced by flow nonuniformity. Specifically, it is seen from Eq. (6.35) that the dependence of $|G|$ on $\hat{\alpha}$ is symmetric about $\hat{\alpha} = 1$, namely with the increase of $\hat{\alpha}$ from 0, $|G|$ first increases and then decreases monotonically as $\hat{\alpha}$ exceeds 1. Figure 6.6b shows the dependence of the phase of the transfer function on St_f for different $\hat{\alpha}$. It is seen that the phase increases with increasing St_f and has a jump of $-\pi$ at St_f satisfying $\left|\hat{\alpha}St_f - St_f\right| = 2n\pi$, as a result of the nodes in the gains at these values of St_f.

It is noted that the existence of nodes in the gain of the transfer function at $\left|\hat{\alpha}St_f - St_f\right| = 2n\pi$ does not mean that the flame does not respond to perturbations at these frequencies. To demonstrate this point, the transverse distribution of the amplitude of the flame oscillation, $|\zeta_1|$, is shown in Fig. 6.7 for St_f = 47.5 and χ = 2 ($\hat{\sigma}_C$ =0 case only). It is seen that for this frequency there exist nodal points ($|\zeta_1|$=0) on the flame surface in addition to the one at the flame base (y = 1). Thus the flame segments within these nodal points are constrained by them and as such oscillate in the manner of a vibrating string. Since there is no nodal point at the flame tail for this frequency, the flame segment between the flame tail and the nearest nodal point exhibits both bulk

oscillatory movement and local wrinkling. Thus the fluctuation of the flame surface area is a consequence of the superposition of these two forms of flame movement. Specifically, for frequencies corresponding to $\left|\hat{\alpha}St_f - St_f\right| = 2n\pi$ ($St_f = 2n\pi$ for $\hat{\alpha} = 0$), a nodal point is located at the flame tail so that the entire flame surface is constrained by the nodal points, and the fluctuation of the flame surface area is only due to flame wrinkling. In this case, it can be shown that the fluctuation amplitude of the flame surface area is $O(\varepsilon^2)$, which is neglected by the linearization process. This is the reason that the transfer function shown in figure 5 has nodes for $\left|\hat{\alpha}St_f - St_f\right| = 2n\pi$ even though the velocity perturbation wrinkles the flame.

6.4.3. Stretch Effects under Uniform Velocity Perturbation

The influence of stretch on the gain and phase of the transfer function is considered in this section. To obtain insight into the results, it is useful to first consider the case of the uniform perturbation velocity field ($\hat{\alpha} = 0$), which is simply an oscillating plug flow. For this case modification of the flame speed occurs only through the curvature of the flame front, as shown in Eq. (6.17). Then, the solution for the disturbed flame location, Eq. (6.26), becomes

$$\zeta_1 = -\frac{1}{iSt}\left[1 - e^{L_1(y-1)}\right] \tag{6.36}$$

Figure 6.7 shows the transverse distribution of the amplitude of flame oscillation for different values of $\hat{\sigma}_C$, with the parameters ($St_f = 47.5$ and $\chi = 2$) chosen to be consistent with the experiments of Bourehla & Baillot [2]. It is seen that in the presence of stretch, the amplitude of the flame front wrinkling decays continuously from the flame base (y =

1) to the tail (y = 0), in contrast to the constant amplitude for the unstretched flame ($\hat{\sigma}_C = 0$). Thus, the experimentally observed damping in the flame front oscillation away from the flame base is reproduced. Furthermore, since this damping increases with increasing $\hat{\sigma}_C$, and since $\hat{\sigma}_C$ itself increases with increasing *Le*, this result also supports the experimental observation of Fig. 6.1 that perturbations are damped to a greater extent in rich than in lean methane flames because the former has a larger *Le*.

To further explore the damping mechanism of flame wrinkling by stretch, we expand Eq. (6.36) for small $\hat{\sigma}_C$. In this limit,

$$L_1 \sim -iSt_f\left(1-2\hat{\sigma}_C^2 St_f^2\right)+\hat{\sigma}_C St_f^2$$

Then Eq. (6.36) becomes

$$\zeta_1 = -\frac{1}{iSt}\left[1-e^{\hat{\sigma}_C St_f^2(y-1)}e^{-iSt_f\left(1-2\hat{\sigma}_C^2 St_f^2\right)(y-1)}\right] \tag{6.37}$$

It is seen that for sufficiently small St_f, Eq. (6.37) degenerates to that of the unstretched flame

$$\zeta_{1,NS} = -\frac{1}{iSt}\left[1-e^{-iSt_f(y-1)}\right] \tag{6.38}$$

as is reasonable to expect. It is further seen from the comparison between Eqs. (6.37) and (6.38) that stretch damps the flame wrinkling through the term $e^{\hat{\sigma}_C St_f^2(y-1)}$, and this damping effect increases exponentially toward the flame tail, i.e. $y \to 0$. This demonstrates that the extent of damping in the flame wrinkling by stretch is controlled by the nondimensional parameter $\hat{\sigma}_C St_f^2$, and becomes $O(1)$ as $\hat{\sigma}_C St_f^2 \sim O(1)$, i.e. as the perturbation frequency satisfies $St_f \sim O\left(\hat{\sigma}_C^{-1/2}\right)$. This property is consistent with the plots in Fig. 6.7. For example, even for the very small stretch, $\hat{\sigma}_C = 0.0005$, the damping is

still quite evident especially near the flame tail (y = 0) because $\hat{\sigma}_C St_f^2 \approx 1.13 \sim O(1)$. For the case of $\hat{\sigma}_C = 0.005$ for which $\hat{\sigma}_C St_f^2 \approx 11.3$, the damping is so strong that flame wrinkling is only evident near the flame base, consistent with the experimental observations of Bourehla & Baillot [2]. Furthermore, the nondimensional parameter $\hat{\sigma}_C St_f^2$ indicates that the damping effect increases quadratically with the perturbation frequency and hence is very sensitive to it. This is the reason that doubling the perturbation frequency is able to completely damp the flame wrinkling except in the flame base region, as shown in Fig. 6.2. It is also seen from Eq. (6.37) and Fig. 6.7 that damping results in a more uniform flame oscillation amplitude, indicating an increase of the relative contribution of the bulk oscillatory movement of the flame to the fluctuation of the flame surface area.

Equation (6.37) further shows that flame stretch is also able to modulate the wavelength of the wrinkling through the term $1-2\hat{\sigma}_C^2 St_f^2$ in the exponential $e^{-iSt_f\left(1-2\hat{\sigma}_C^2 St_f^2\right)(y-1)}$, and this modulation effect is $O(1)$ for $St_f \sim O\left(\hat{\sigma}_C^{-1}\right)$. However, at such a large St_f, wrinkling is damped such that its wavelength does not have much significance. Thus, this effect can be neglected so that Eq. (6.37) can be further simplified to

$$\zeta_1 = -\frac{1}{iSt}\left[1 - e^{\hat{\sigma}_C St_f^2 (y-1)} e^{-iSt_f (y-1)}\right]$$

and the expansion of L_1 only needs to keep the first two terms

$$L_1 \sim -iSt_f + \hat{\sigma}_C St_f^2 \tag{6.39}$$

It is noted that by increasing St_f to $O\left(\hat{\sigma}_C^{-1}\right)$, the expansion for L_1, Eq. (6.39), becomes less accurate. However, the trend revealed for the flame response at this order of frequency is still preserved.

We next study effects of flame stretch on the transfer function. Since the heat release rate mainly depends on the flame surface area, which in turn depends on the flame wrinkling, it is expected that flame stretch starts to have an $O(1)$ effect on the heat release and thereby on the transfer function for frequency St_f from $O\left(\hat{\sigma}_C^{-1/2}\right)$. Substituting Eq. (6.36) into Eqs. (6.31) and (6.32), respectively, yields

$$G_S = -\frac{L_1\hat{\sigma}_C}{iSt_f}\left(1-e^{-L_1}\right) \tag{6.40}$$

$$G_A = -\frac{1}{iSt_f}\left(1-e^{-L_1}\right) \tag{6.41}$$

Figure 6.8 shows variations of the gains of G, G_A and G_S, with the reduced Strouhal number, St_f, for $\hat{\sigma}_C = 0.05$. The gain of the overall transfer function for the unstretched case ($\hat{\sigma}_C = 0$),

$$G_{\hat{\sigma}_C=0} = -\frac{1}{iSt_f}\left(1-e^{iSt_f}\right) \tag{6.42}$$

is also plotted for the purpose of comparison. It is seen that in the presence of flame stretch, the transfer function shows quite different behavior from the unstretched case. Specifically, the nodes at $St_f = 2n\pi$ in the gain of the transfer function for the unstretched case ($\hat{\sigma}_C = 0$) are eliminated in the presence of stretch, as already shown in Fig. 6.7, leading to higher values of $|G|$ for the stretched flame around these frequencies. Relaxation of the flame surface from the nodal points then enhances fluctuation of the

flame surface area, through the bulk oscillatory movement, to a larger extent than the damping effect through reduced wrinkling, which is $O(\varepsilon^2)$ for $St_f = 2n\pi$. Moreover, for the stretched case the overall transfer function G is very close to G_A at small St_f (< 5), implying that contribution from the fluctuation of the flame surface area dominates that of the flame speed. However, with increasing St_f the relative contribution of G_S increases and finally becomes comparable to G_A at $St_f \sim 30$. It is noted that the gain of the overall transfer function, $|G|$, is not simply the sum of $|G_A|$ and $|G_S|$ because G_A and G_S are not necessarily in phase, as will be shown in Fig. 6.9.

The dependence of the transfer functions, G_A, G_S and G, on the flame stretch $\hat{\sigma}_C$ and perturbation frequency St_f can be further illustrated by substituting the expansion for L_1, Eq. (6.39), into Eqs (6.40) and (6.41), resulting in

$$G_S \approx -\frac{1}{iSt_f}\left(-i\hat{\sigma}_C St_f + \hat{\sigma}_C^2 St_f^2\right)\left(1 - e^{-\hat{\sigma}_C St_f^2} e^{iSt_f}\right) \tag{6.43}$$

$$G_A \approx -\frac{1}{iSt_f}\left(1 - e^{-\hat{\sigma}_C St_f^2} e^{iSt_f}\right) \tag{6.44}$$

Comparing Eq. (6.44) with the transfer function for the unstretched flame, Eq. (6.42), shows that flame stretch starts to have an $O(1)$ effect on the transfer function as the perturbation frequency St_f satisfies $\hat{\sigma}_C St_f^2 \sim O(1)$, as noted earlier. At this frequency, $G_S/G_A \sim O\left(\hat{\sigma}_C^{1/2}\right)$ and hence the contribution from the flame speed fluctuation is secondary relative to that of the flame surface area. Thus, the overall transfer function G is mostly derived from fluctuations of the flame surface area, which however is still

affected by flame stretch through modulation of the shape of the wrinkles. Therefore, we have

$$G \approx G_A \approx -\frac{1}{iSt_f}\left(1 - e^{-\hat{\sigma}_C St_f^2} e^{iSt_f}\right) \sim O\left(\hat{\sigma}_C^{1/2}\right) \tag{6.45}$$

With St_f increasing from $O\left(\hat{\sigma}_C^{-1/2}\right)$ to $O\left(\hat{\sigma}_C^{-1}\right)$, the contribution from the flame speed fluctuation, G_S, becomes comparable to G_A. Furthermore, since flame wrinkling is totally suppressed at this order of St_f, fluctuations of the flame surface area are mainly due to the bulk movement of the flame. Then, the transfer functions become

$$G_S \approx -\frac{1}{iSt_f}\left(-i\hat{\sigma}_C St_f + \hat{\sigma}_C^2 St_f^2\right), \qquad G_A \approx -\frac{1}{iSt_f} \tag{6.46}$$

and the overall transfer function is given by

$$G \approx -\frac{1}{iSt_f}\left(1 + \hat{\sigma}_C^2 St_f^2 - i\hat{\sigma}_C St_f\right) \sim O\left(\hat{\sigma}_C\right) \tag{6.47}$$

The above characteristics are consistent with Fig. 6.8, which shows that G and G_A have almost identical values for $St_f < 5$ ($\hat{\sigma}_C St_f^2 \sim O(1)$), while G_A and G_S contribute comparably to the overall transfer function G for $St_f > 20$ ($\hat{\sigma}_C St_f \sim O(1)$).

Figure 6.9 shows variations of the phases of G, G_A and G_S with the reduced Strouhal number, St_f, for $\hat{\sigma}_C = 0.05$. It is seen that, compared to the unstretched case, the $-\pi$ jump in the phase resulting from the nodes in the gain of the transfer function is smoothed out, due to the elimination of these nodes in the presence of stretch. Furthermore, it is seen that at small St_f, the phase of G follows closely that of G_A, whereas with increasing St_f it approaches the phase of G_S due to the increased relative contribution

of G_S. This is the same trend as what was discussed for the gain of the transfer function in Fig. 6.8.

6.4.4. Stretch Effects under Nonuniform Velocity Perturbation

In the more general case of a nonuniform perturbation velocity field in the streamwise direction ($\hat{\alpha} \neq 0$), the flame speed is modified by both the curvature and aerodynamic strain, as shown in equation (6.17). In addition, the baseline flame response is also changed due to the wrinkling locally induced by the flow nonuniformity.

Substituting Eq. (6.26) into Eqs. (6.31) and (6.32) yields the transfer functions under nonuniform perturbation,

$$G_S = -\frac{\hat{\sigma}_C C_1}{iSt_f}\left[L_1\left(1-e^{-L_1}\right)+iSt_f\hat{\alpha}\left(1-e^{iSt_f\hat{\alpha}}\right)\right]-\hat{\sigma}_S\left(1-e^{iSt_f\hat{\alpha}}\right) \tag{6.48}$$

$$G_A = -\frac{C_1}{iSt_f}\left(-e^{-L_1}+e^{iSt_f\hat{\alpha}}\right) \tag{6.49}$$

where

$$C_1 = \frac{1-i\hat{\sigma}_S St_f\hat{\alpha}}{i\hat{\sigma}_C St_f\hat{\alpha}^2-\hat{\alpha}+1}$$

Figure 6.10 shows variations of the gains of G, G_A and G_S with St_f, for $\hat{\sigma}_C = 0.05$, $\hat{\sigma}_S = 0$ and $\hat{\alpha} = 2$. It is seen that at small frequencies ($St_f < 5$) the overall transfer function G can be approximately represented by G_A, whereas at large St_f, G follows closely the trend of G_S, indicating that contributions from fluctuations of the flame surface area and flame speed dominate at small and large frequencies, respectively. To further analyze the trend shown in Fig. 6.10, we substitute the expansion for L_1, Eq. (6.39), into Eqs. (6.26), (6.48) and (6.49), and obtain

$$\zeta_1 \approx -\frac{C_1}{iSt}\left(-e^{-\hat{\sigma}_C St_f^2(1-y)}e^{iSt_f(1-y)} + e^{iSt_f\hat{\alpha}(1-y)}\right) \tag{6.50}$$

$$G_S = -\frac{C_1}{iSt_f}\left[\left(-i\hat{\sigma}_C St_f + \hat{\sigma}_C^2 St_f^2\right)\left(1-e^{-\hat{\sigma}_C St_f^2}e^{iSt_f}\right) + i\hat{\sigma}_C St_f\hat{\alpha}\left(1-e^{iSt_f\hat{\alpha}}\right)\right] - \hat{\sigma}_S\left(1-e^{iSt_f\hat{\alpha}}\right) \tag{6.51}$$

$$G_A = -\frac{C_1}{iSt_f}\left(-e^{-\hat{\sigma}_C St_f^2}e^{iSt_f} + e^{iSt_f\hat{\alpha}}\right) \tag{6.52}$$

Comparing Eq. (6.52) with the transfer function for the unstretched flame, Eq. (6.34), shows that flame stretch begins to have $O(1)$ effects on the transfer function G_A as the perturbation frequency satisfies $\hat{\sigma}_C St_f^2 \sim O(1)$, as in the case of the uniform velocity perturbation. At this frequency, $G_S/G_A \sim O\left(\hat{\sigma}_C^{1/2}\right)$ and hence the contribution from G_S can be neglected in the overall transfer function. Thus, the overall transfer function G is mostly derived from fluctuations of the stretch-affected flame surface area:

$$G \approx G_A = -\frac{C_1}{iSt_f}\left(-e^{-\hat{\sigma}_C St_f^2}e^{iSt_f} + e^{iSt_f\hat{\alpha}}\right) \tag{6.53}$$

Furthermore, as we have discussed in Section 6.3.2, under nonuniform velocity perturbation the solution is determined by the superposition of the convective wrinkling and the wrinkling locally induced by flow nonuniformity. It is apparent from the comparison between results obtained with and without stretch effects, Eqs. (6.33) and (6.50) and Eqs. (6.34) and (6.53), that stretch only damps the convective wrinkling, with the locally induced wrinkling remaining unchanged.

As St_f increases from $O\left(\hat{\sigma}_C^{-1/2}\right)$ to $O\left(\hat{\sigma}_C^{-1}\right)$ such that $\hat{\sigma}_C St_f \sim O(1)$, the contribution from the flame speed fluctuation, G_S, becomes comparable to that from G_A. Furthermore, it is seen from Eq. (6.51) that aerodynamic strain only operates through the flame speed fluctuation. Further note that since both $\hat{\sigma}_C$ and $\hat{\sigma}_S$ are determined by the

nondimensional thermal thickness of the flame (see Eqs. (6.18) and (6.19)) and that we have assumed $\beta\left(Le^{-1}-1\right)\sim O(1)$, $\hat{\sigma}_C$ and $\hat{\sigma}_S$ can be assumed to have the same order of magnitude. Thus, at $St_f \sim O\left(\hat{\sigma}_C^{-1}\right)$, aerodynamic strain contributes to G_S comparably with the rest of the terms of G_S. At this order of St_f, contributions to G_A and G_S due to convective wrinkling have been totally damped such that the transfer functions become

$$G_S = -\frac{C_1}{iSt_f}\left[\left(-i\hat{\sigma}_C St_f + \hat{\sigma}_C^2 St_f^2\right) + i\hat{\sigma}_C St_f \hat{\alpha}\left(1-e^{iSt_f\hat{\alpha}}\right)\right] - \hat{\sigma}_S\left(1-e^{iSt_f\hat{\alpha}}\right) \tag{6.54}$$

$$G_A = -\frac{C_1 e^{iSt_f\hat{\alpha}}}{iSt_f} \tag{6.55}$$

With further increase of St_f, G_S dominates over G_A and G follows closely the trend of G_S at large St_f, which is consistent with Fig. 6.10.

Figure 6.11 shows variations of the phases of G, G_A and G_S with St_f, for $\hat{\sigma}_C = 0.05$, $\hat{\sigma}_S = 0$ and $\hat{\alpha} = 0$. It is seen that, as in the case of the uniform velocity perturbation shown in Fig. 6.9, the phase jump of $-\pi$ is moderated by stretch and the phase of G follows the trends of G_A and G_S at small and large St_f, respectively. The difference is that for this value of $\hat{\alpha}$ (= 2), all the phases have close values.

In contrast to the constant gain of unity for the unstretched $\hat{\alpha} = 1$ case shown in Fig. 6.5, results show that stretch effects cause the gain to reduce monotonically with increasing St_f. It is also noted that the gains for the $\hat{\alpha} = 0$ and $\hat{\alpha} = 2$ cases are identical in the unstretched case. However, in the presence of stretch, they possess different values. As we have discussed, the special characteristics for the gain of the transfer function of the unstretched case, such as unity gain for $\hat{\alpha} = 1$ and the same gains for $\hat{\alpha} = 0$ and $\hat{\alpha} = 2$, are consequences of the superposition of the convective and locally induced

wrinkling. Therefore, for these values of $\hat{\alpha}$, damping of the convective wrinkling leads to substantially different behavior in the presence of stretch.

6.5. Conclusions

In this study we have investigated the linear response of a 2D wedge-shaped premixed flame to harmonic velocity perturbations, allowing for the dependence of the flame speed on stretch. Different from previous studies, the transfer function now consists of contributions from fluctuations of both the flame surface area and flame speed. Two nondimensional parameters, $\hat{\sigma}_C St_f^2$ and $\hat{\sigma}_C St_f$, were identified to characterize their relative contributions and thereby the influence of flame stretch on the flame response. Specifically, as the perturbation frequency satisfies $\hat{\sigma}_C St_f^2 \sim O(1)$, i.e. $St_f \sim O\left(\hat{\sigma}_C^{-1/2}\right)$, flame stretch starts to have $O(1)$ effects on the transfer function through damping of the perturbation-induced flame wrinkling. At this order of the frequency, the contribution from the flame speed fluctuation is negligibly small. Thus flame stretch affects the transfer function only through its modulation of the flame shape and thereby its surface area, with this effect increasing with the square of the perturbation frequency. At larger frequencies such that $\hat{\sigma}_C St_f \sim O(1)$, i.e. $St_f \sim O\left(\hat{\sigma}_C^{-1}\right)$, contributions from fluctuations of the flame surface area and flame speed become comparable.

It is noted that previously flame stretch was thought to be not important in the response of flames to perturbations. The suggested reason [8] is that while the flame curvature and hence stretch effects could become large for large perturbation frequencies at which the wavelength of the perturbation-induced flame wrinkling is small, the sensitivity of the flame response diminishes significantly at large frequencies. The

present study has however demonstrated that flame stretch is still important for "moderate" perturbation frequencies even for small $\hat{\sigma}_C$. This is because even if $\hat{\sigma}_C$ is small, $St_f \sim O\left(\hat{\sigma}_C^{-1}\right)$ could assume values that are not very large but nevertheless would induce $O(1)$ effects on the flame response.

While the present study has yielded useful insights into the effects of stretch on the flame response upon being harmonically disturbed, especially on the role of self-induced curvature damping leading to the experimentally observed phenomenon of filtering, and the critical Strouhal numbers at which stretch effects become important, there are additional issues that need to be investigated. In particular, the study has focused on damping situations because of our interest in understanding the filtering phenomenon, and because they are sufficient to ensure stability in operations. It would however also be of interest to study situations in which the perturbation is either amplified or sustained, especially for small *Le* mixtures for which σ_C could become negative. Operationally, it has been suggested that resonant combustion could facilitate the heat transfer characteristics of burners.

We also note that, by studying 2D instead of axisymmetric flames, the effects of the azimuthal curvature of the bulk flame on the development of wrinkles are suppressed. Studies on flamefront cellular instability [3, 18] have shown that these wrinkles tend to be moderated by positive stretch and aggravated by negative stretch, which are respectively manifested by the wedge and conical geometries. The richness of the potential flame responses merits further investigation.

References

1. Rayleigh, L., *The Theory of Sound*, Dover Publications, New York (1945).
2. Bourehla, A. and Baillot, F., *Combust. Flame* **114**: 303-318 (1998).
3. Law, C. K., *Combustion Physics*, Cambridge University Press, New York (2006).
4. Rajaram, R. and Lieuwen, T., *Combust. Sci. Technol.* **175**: 2269-2298 (2003).
5. Cho, J. H. and Lieuwen, T., *Combust. Flame* **140**: 116-129 (2005).
6. McIntosh, A. C., *Phil. Trans. R. Soc. Lond. A.* **357**: 3523-3538 (1999).
7. Baillot, F., Durox, D. and Prud'homme, R., *Combust. Flame* **88**: 149-168 (1992).
8. Fleifel, M., Annaswamy, A. M., Ghoniem, Z. A. and Ghoniem, A. F., *Combust. Flame* **106**: 487-510 (1996).
9. Ducruix, S., Durox, D. and Candel, S., *Proc. Combust. Inst.* **28**: 765-773 (2000).
10. Schuller, T., Durox, D. and Candel, S., *Combust. Flame* **134**: 21-34 (2003).
11. Dowling, A. P., *J. Fluid Mech.* **346**: 271-290 (1997).
12. Lieuwen, T., *Proc. Combust. Inst.* **30**: 1725-1732 (2005).
13. Kerstein, A. R., Ashurst, W. T. & Williams, F. A., *Phys. Rev.* **A27**: 2728-2731 (1988).
14. Chung, S. H. and Law, C. K., *Combust. Flame* **72**: 325-336 (1988).
15. Schuller, T., Ducruix, S., Durox, D. and Candel, S., *Proc. Combust. Inst.* **29**: 107-113 (2002).
16. Matalon, M. and Matkowsky, B. J., *J. Fluid Mech.* **124**: 239-259 (1982).
17. Boyer, L. & Quinard, J., *Combust. Flame* **82**: 51-65 (1990).
18. Sivashinsky, G. I., Law, C. K. and Joulin, G., *Combust. Sci. Technol.* **28**, 155-159 (1982).

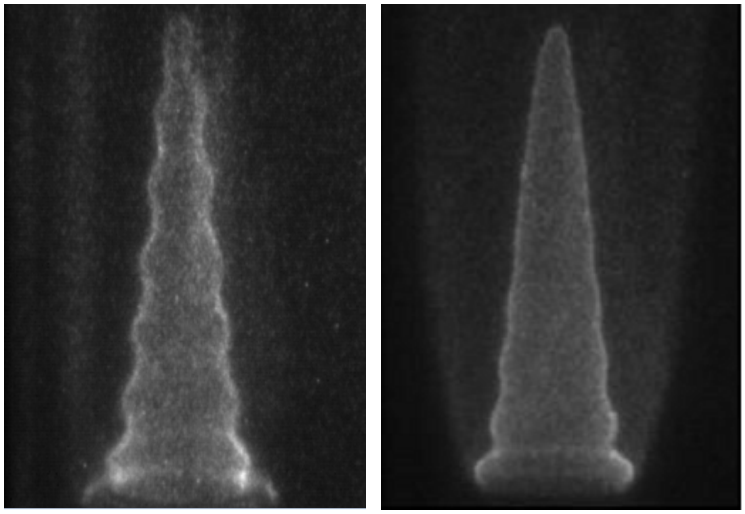

(a) (b)

Figure 6.1. Visualization of (a) a 130 Hz acoustically excited lean methane flame (ϕ = 0.8, u_o = 0.65 m/s), and (b) a 140 Hz acoustically excited rich methane flame (ϕ = 1.4, u_o = 0.7 m/s). Images show flame wrinkling with constant and damped amplitudes, respectively.

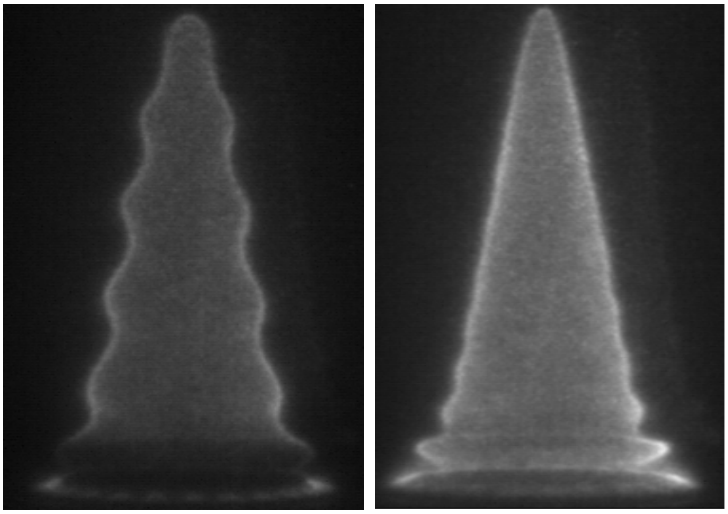

(a) (b)

Figure 6.2. Visualization of a (a) 100 Hz and (b) 190 Hz acoustically excited propane flame (ϕ = 0.7 and u_o= 0.8 m/s). Images show flame wrinkling with constant and damped amplitude, respectively.

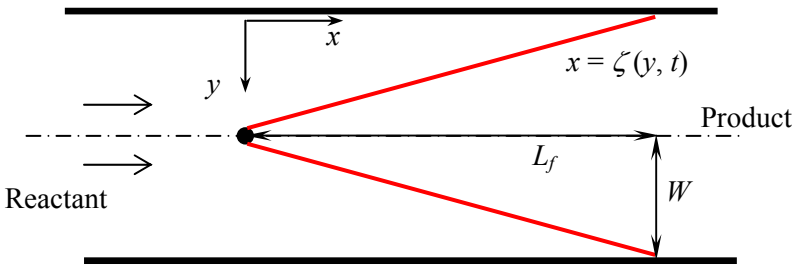

Figure 6.3. Schematic of two dimensional wedge shaped flame geometry.

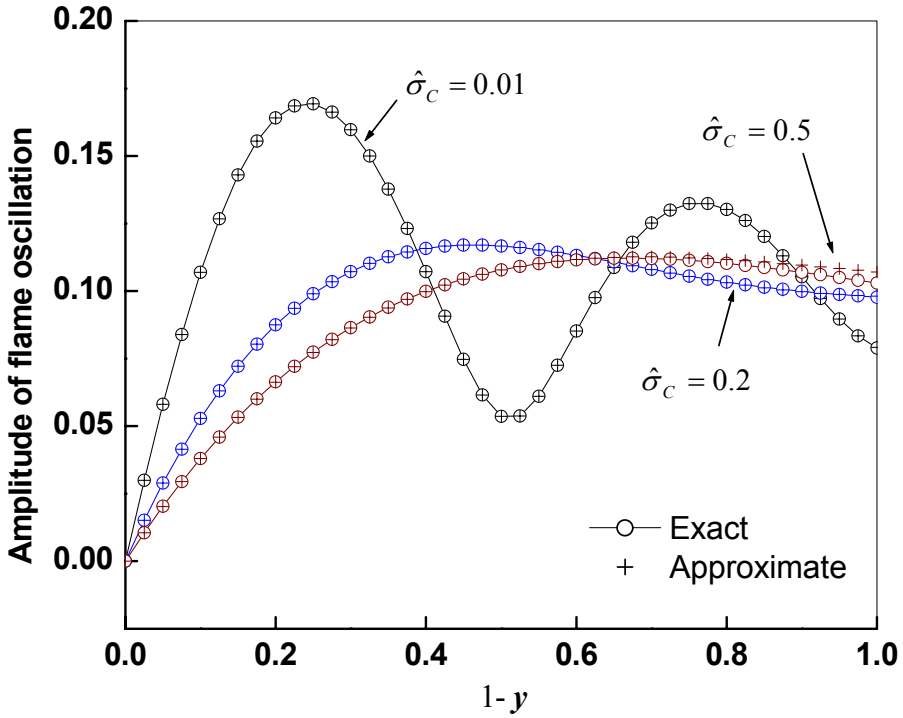

Figure 6.4. Transverse distribution of the flame oscillation amplitude, $|\zeta_1(y)|$, from Eqs. (6.21) and (6.26), respectively, for different values of $\hat{\sigma}_C$ with $St = 10$, $\chi = 2$ and $\hat{\alpha} = 0$. Note that $y = 1$ and $y = 0$ correspond to the flame base and tale, respectively.

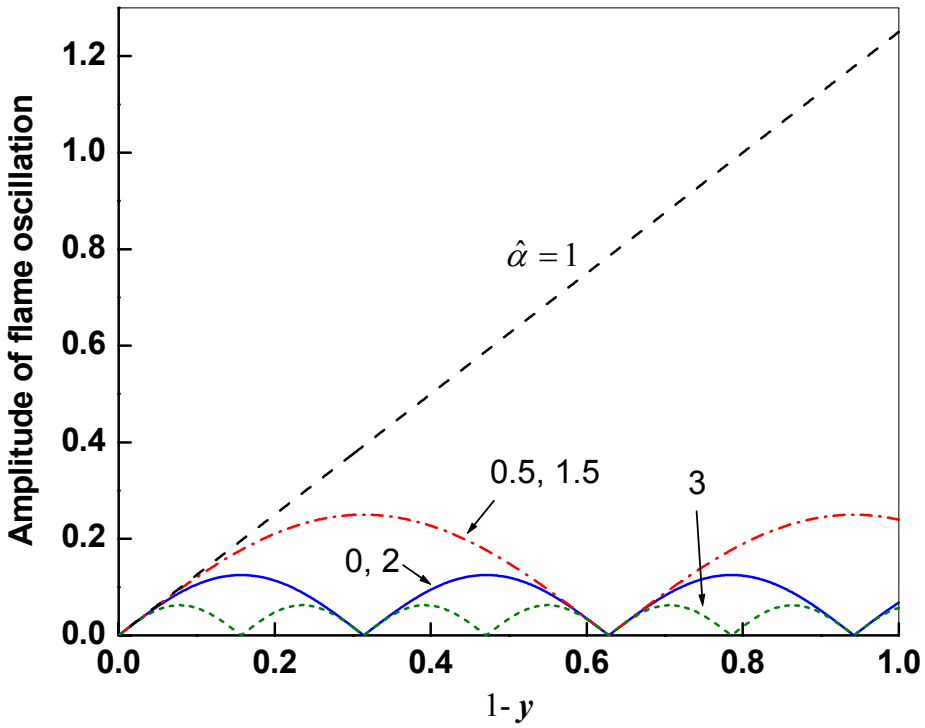

Figure 6.5. Transverse distribution of the flame oscillation amplitude, $|\zeta_1(y)|$, for the unstretched flame with St_f = 20, χ = 2 and different $\hat{\alpha}$. Note that y = 1 and y = 0 correspond to the flame base and tale, respectively.

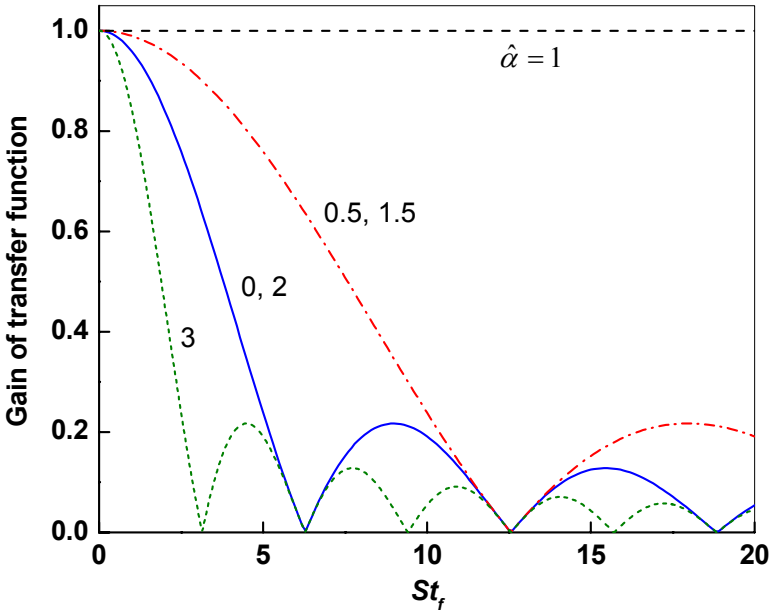

(a)

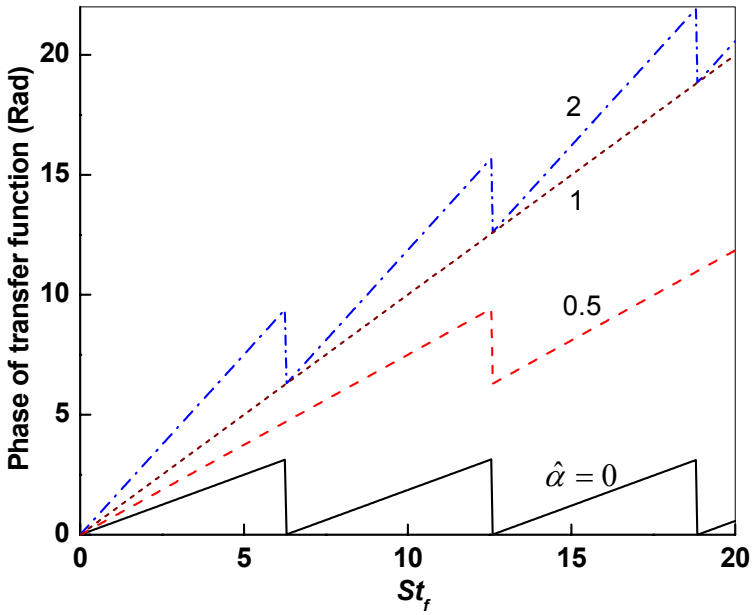

(b)

Figure 6.6. Dependence of (a) the gain and (b) the phase of the transfer function on St_f for unstretched flame with different $\hat{\alpha}$.

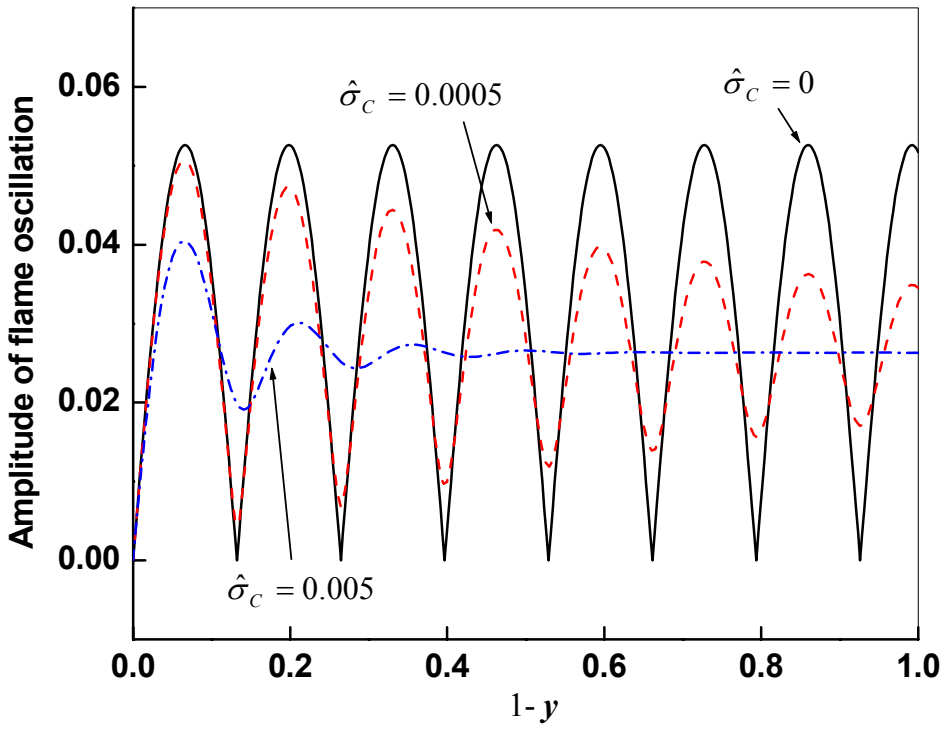

Figure 6.7. Transverse distribution of the flame oscillation amplitude, $|\zeta_1(y)|$, for different values of $\hat{\sigma}_C$ with St_f = 47.5, χ = 2 and $\hat{\alpha} = 0$. Note that y = 1 and y = 0 correspond to the flame base and tale, respectively.

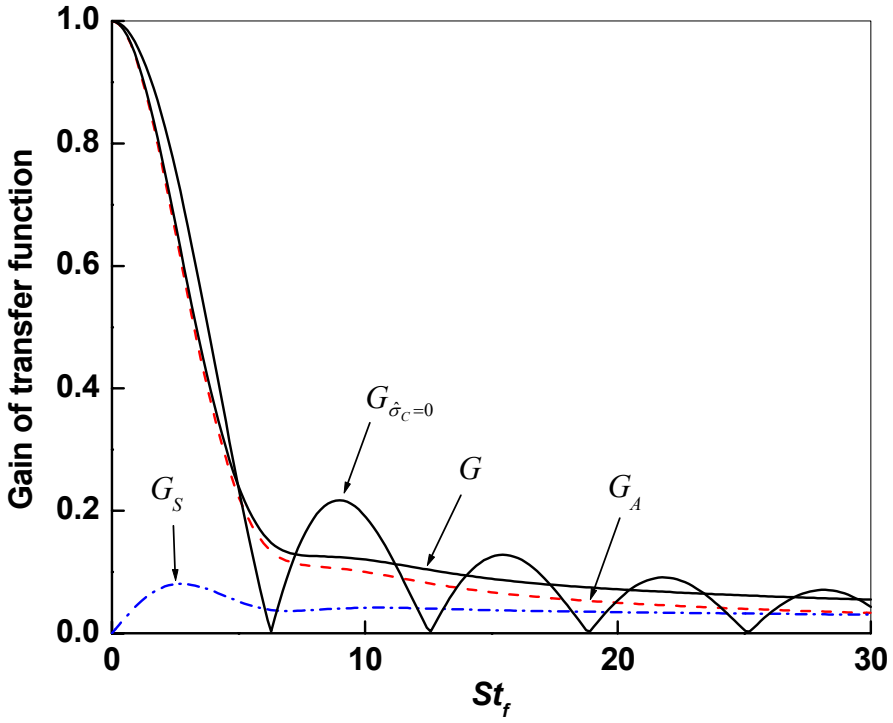

Figure 6.8. Variations of the gains of the overall transfer function G and the transfer functions resulted from the fluctuations of flame surface area and flame speed, G_A and G_S, with St_f for $\hat{\sigma}_C = 0.05$ and $\hat{\alpha} = 0$. The gain of the overall transfer function for $\hat{\sigma}_C = 0$ and $\hat{\alpha} = 0$ is also plotted for comparison.

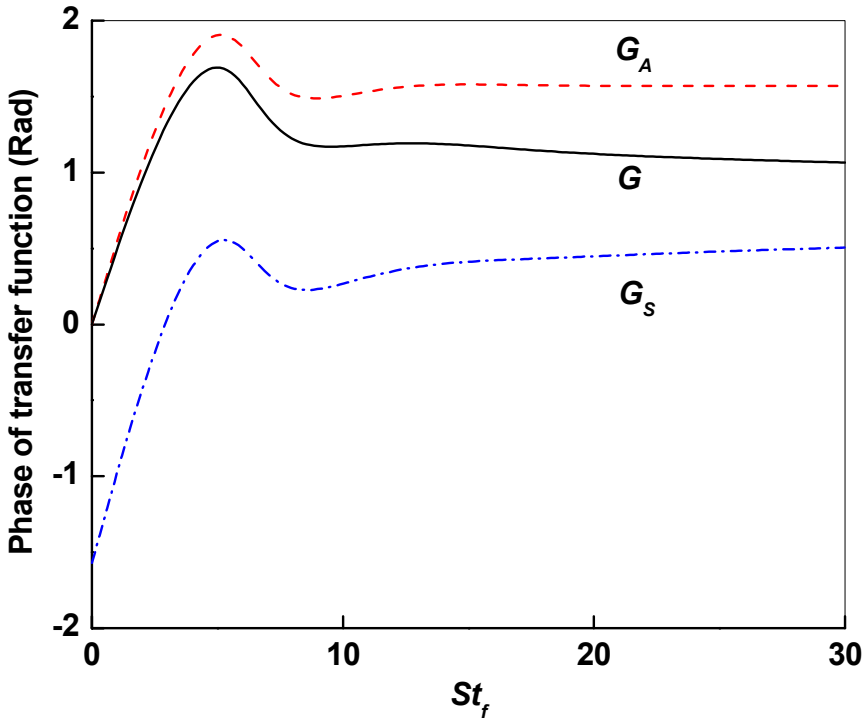

Figure 6.9. Variations of the phase of the overall transfer function G and the transfer functions resulted from the fluctuations of flame surface area and flame speed, G_A and G_S, with St_f for $\hat{\sigma}_C = 0.05$ and $\hat{\alpha} = 0$.

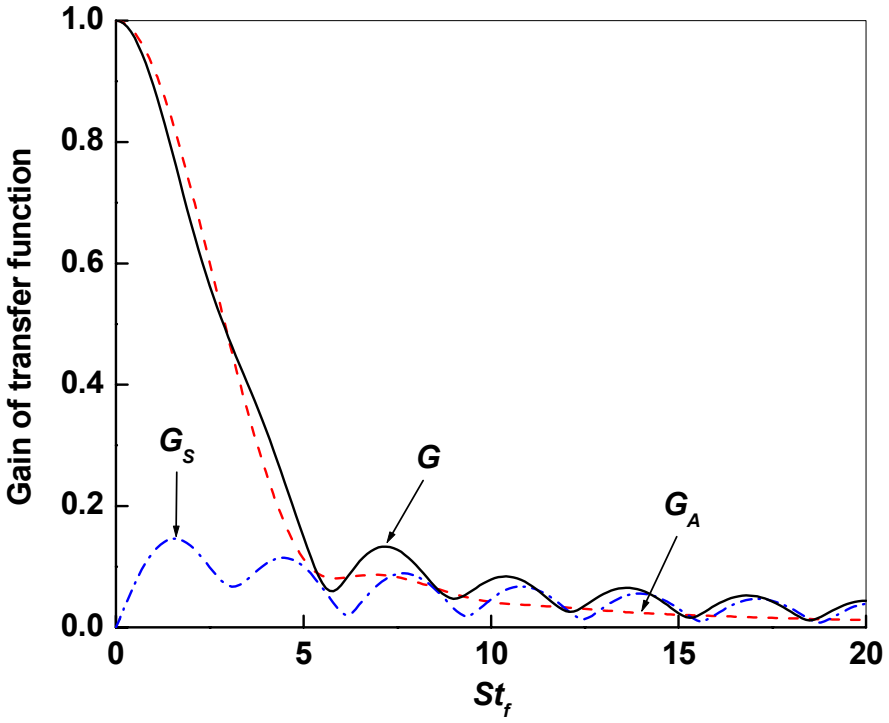

Figure 6.10. Variations of the gains of the overall transfer function G and the transfer functions resulted from the fluctuations of flame surface area and flame speed, G_A and G_S, with St_f for $\hat{\sigma}_C = 0.05$, $\hat{\sigma}_S = 0$ and $\hat{\alpha} = 2$.

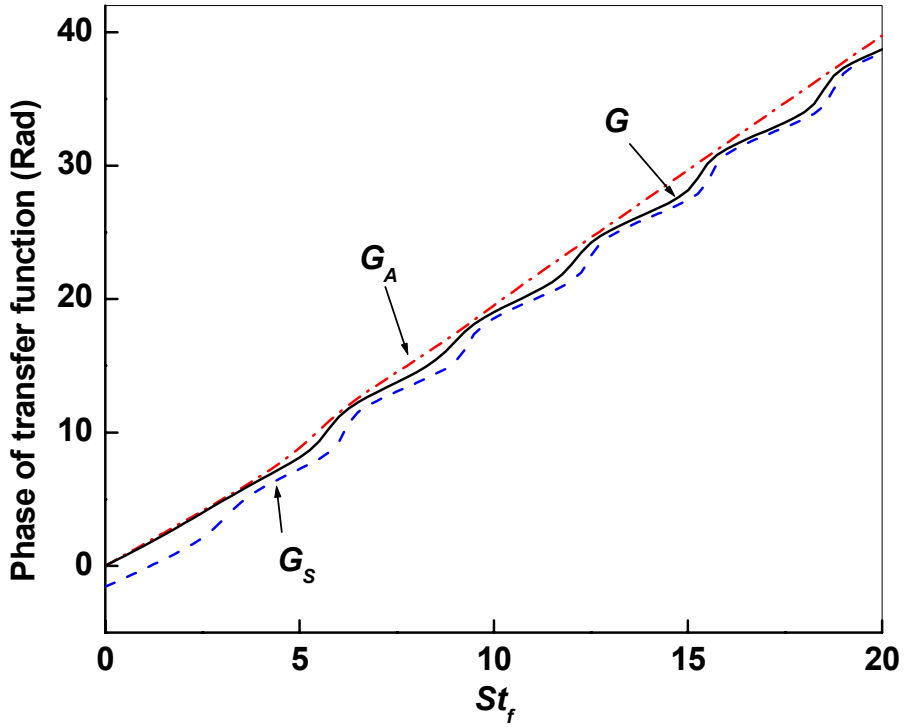

Figure 6.11. Variations of the phases of the overall transfer function G and the transfer functions resulted from the fluctuations of flame surface area and flame speed, G_A and G_S, with St_f for $\hat{\sigma}_C = 0.05$, $\hat{\sigma}_S = 0$ and $\hat{\alpha} = 2$.

Chapter 7: Summary and Recommendations for Future Work

7.1. Summary

In this dissertation flame oscillations in both diffusion and premixed flames have been analytically studied. For diffusion flames (Chapters 2 ~ 5), the study was focused on the intrinsic oscillations induced by the thermal-diffusive instability and their coupling with the imposed flow oscillations. Radiative heat loss was also considered. To facilitate the study on radiation-affected flames, a model allowing for radiative loss and non-unity Lewis numbers was developed and then utilized to study radiation-induced flame extinctions and oscillations. For premixed flames (Chapter 6), the study was focused on the effects of flame stretch on the response of a 2D wedge-shaped flame to harmonic flow oscillations.

Specifically, in Chapter 2, a systematic analysis of flame oscillations was carried out for adiabatic planar diffusion flames. We employed the asymptotic theory of Cheatham & Matalon [1], and performed a bifurcation analysis in which the Damköhler number Da is chosen to be very close to the critical Damköhler number Da_{Cr}, corresponding to the marginally stable state. A nonlinear evolution equation of the Landau type was derived for the amplitude of perturbation. Solutions to the resulting equation indicate three distinct burning regimes, which are mapped out in parameter space. Results show that the perturbations may either decay to zero such that the planar flame is stable, or the amplitude can become unbounded in finite time, indicating flame quenching. Furthermore, our equation admits time-periodic (limit-cycle) solutions,

although these solutions were not found to exist over a wide range of parameters typical of combustion systems.

In Chapter 3, we carried out a systematic analysis of the forced flame oscillations subjected to imposed flow oscillations of small amplitude. The linear response of flames was first examined and the results show that even very small imposed flow oscillations can induce flame oscillations of infinitely large amplitude, as the frequency of flow oscillations approaches the intrinsic oscillation frequency when the flame is near the marginal state of thermal-diffusive instability. This is a resonance phenomenon between the intrinsic and forced flame oscillations. The nonlinear near-resonant response is then conducted by deriving an evolution equation for the amplitude of forced oscillation. The Damköhler number Da and forced frequency are chosen to be close to Da_{Cr} and the intrinsic oscillation frequency so that even very weak forcing is able to induce $O(1)$ oscillation amplitude. It is shown that by considering inherent nonlinearity, flame oscillation exhibits finite amplitude at the resonant condition. Examination of the evolution equation revealed that, in most situations, flames with larger Le_F, smaller ϕ, smaller ΔT, and $1 < Le_O < 2$ are most responsive to the flow oscillations.

In Chapter 4, we studied the structure and extinction characteristics of radiative counterflow diffusion flames. A model that includes radiative loss and nonunity Lewis numbers of the fuel and oxidant was first developed using multiscale asymptotic analysis. This model considers properly the excess enthalpy, which is a crucial element in stability analyses but was overlooked in previous analyses for radiative diffusion flames [2-4]. The existence of dual extinction limits in the presence of radiative heat loss, namely the kinetic limit at small Damköhler numbers (high stretch rate) and the radiative limit at

large Damköhler numbers (low stretch rate), were identified. The former was found to be minimally affected by radiative loss, while substantial amount of heat loss is associated with the radiative limit. Reactant leakage, however, is the cause for both limits. The influence of radiative loss on the extinction Damköhler numbers was found to be through its effects on the flame temperature, excess enthalpy and the reduced extinction Damköhler number. At both extinction limits, contributions from the flame temperature are always important and dominant. Contributions from the other two, however, could be important in some special cases. Specifically, the contribution from the excess enthalpy is important for small Le_O and it may be comparable to the contribution from the flame temperature when radiative loss is small. Thus, overlooking the excess enthalpy in previous analyses may result in rather large error in the predicted extinction Damköhler numbers, especially the kinetic one.

In Chapter 5, a linear stability analysis was conducted using the model developed in Chapter 4 to study the occurrence of flame oscillations in radiation-affected diffusion flames. The intrinsic oscillations near the radiative extinction limit at large Damköhler numbers were identified, in addition to the one near the kinetic limit at small Damköhler numbers. It was shown that radiative loss assumes a similar role as varying the thermal diffusivity of the reactants. Thus, flame oscillation near the radiative limit is still thermal-diffusive in nature although it may develop under unity Lewis numbers. The unstable range of Damköhler numbers near the radiative limit shows quite similar parametric dependence on Le_F, Le_O, ϕ, and the radiative loss as that near the kinetic limit. However, they show different dependence on the temperature difference between the supplying reactants.

In Chapter 6, we studied the linear response of 2D wedge-shaped premixed flames to harmonic velocity oscillations, allowing for the influence of flame stretch manifested as variations in the local flame speed along the wrinkled flame front. Results obtained from analyzing the G-equation show that the flame response is mainly characterized by the Markstein number $\hat{\sigma}_C$ and the Strouhal number St_f, which respectively characterize the curvature effect of the wrinkles and the oscillation frequency. Flame stretch is found to become important when the oscillation frequency satisfies $\hat{\sigma}_C St_f^2 \sim O(1)$, i.e. $St_f \sim O\left(\hat{\sigma}_C^{-1/2}\right)$. Specifically, for frequencies below this order, stretch effects are small and the flame responds as an unstretched one. When the frequencies are of this order, the transfer function, defined as the ratio of the normalized oscillation of the heat release rate to that of the velocity, is contributed mostly from oscillations of the flame surface area, which is now affected by stretch. Finally, as the frequency increases to $St_f \sim O\left(\hat{\sigma}_C^{-1}\right)$, i.e. $\hat{\sigma}_C St_f \sim O(1)$, the direct contribution from the stretch-affected flame speed oscillation to the transfer function becomes comparable to that of the flame surface area. The present study phenomenologically explains the experimentally observed damping of the perturbation-induced flame wrinkling for large frequency flow oscillations as well as for thermal-diffusively stable and weakly unstable mixtures.

7.2. Recommendations for Future Work

7.2.1. Comprehensive Studies on the Response of Stretched-Affected Premixed Flames to Flow Modulations

In Chapter 6, the response of premixed flames to flow oscillations was studied and the effects of flame stretch on the transfer functions have been identified. However, this study was still a quite preliminary one. First, the experiments were conducted only for methane/air and propane/air flames under very limited stoichiometric conditions and a narrow range of oscillation frequencies. As such, while the experimental results were able to demonstrate qualitatively the existence of flame stretch effects, they cannot be used for the quantitative comparison with the theoretical results. In addition, both the experimental and theoretical results in Chapter 6 were limited to the thermal-diffusively stable or weakly unstable flames such that the Markstein number $\hat{\sigma}_C$ is always positive. Since the mathematical simplifications and theoretical analysis in Chapter 6 were based on the assumption of small and positive $\hat{\sigma}_C$, it is expected that the stretch effects would be significantly different under a negative $\hat{\sigma}_C$. Therefore, a systematically designed experiment covering a variety of fuels with different stoichiometric conditions and diluents is needed to extend the current study to a wider parameter range. A careful measurement of the flame surface area would allow a quantitative comparison with the theory.

Second, the study of Chapter 6 was based on the 2D wedge-shaped flame. By studying 2D instead of axisymmetric flames, the effects of the azimuthal curvature of the bulk flame on the development of wrinkles are suppressed. However, studies on flamefront cellular instability [5, 6] have shown that these wrinkles tend to be moderated by positive stretch and aggravated by negative stretch, which are respectively manifested by the wedge and conical geometries. In addition, it is important to note that for axisymmetric flames, since the stretch-induced damping of flame wrinkling is most

significant at the flame tip, a region that contributes substantially and minimally to the flame area for wedge and conical flames, respectively, the impact of stretch on the transfer function of wedge flames is expected to be significantly higher than that of conical flames. The richness of these potential flame responses in different flame geometries certainly merits further investigation.

Third, the studies in Chapter 6 and the above discussions are so far limited to the linear response of flames, and hence to small amplitudes of flow and flame oscillations. In order to study the effects of flame stretch on the limit cycle amplitude of flame oscillations, the current study needs to be extended to the nonlinear regime allowing for finite amplitude of flow and flame oscillations. Specifically, Lieuwen [7] showed that flames with less flame surface area near the attached point exhibit stronger nonlinearity. Since the damping effect of flame stretch is more significant for such flames because a larger portion of the flame wrinkling is damped by stretch, flame stretch is expected to have a strong effect on the nonlinear response of flames.

Finally, the understanding gained from the above studies on the response of flames to flow modulations should be applied to the acoustic equation in reactive flows to investigate the generation of acoustic waves by unsteady combustion heat release. Only then we can have a complete analysis on the driving mechanism responsible for the development of thermo-acoustic instability.

7.2.2. Numerical Simulation of Unsteady Combustion Heat Release in More Realistic Flows

Guided by the understandings gained from the theoretical analysis in highly idealized flame configurations, the studies on the response of premixed flames to flow modulations should be extended to more realistic flows, such as mixing layer flows, with emphasis on the effects of flow unsteadiness on the combustion heat release. Specifically, the evolution processes of large coherent vortex structures in mixing layers, including vortex rollup, formation and paring control the transport of fresh reactants into the flame and distort the flame surface area, and thereby determine the nonsteady conversion rate of reactants and the combustion heat release. Since these processes are generally multi-dimensional, transient and even turbulent, advanced numerical methods must be adopted, such as Large Eddy Simulation (LES) and Direct Numerical Simulation (DNS). For plane mixing layer flows, the study can first be conducted in a simpler time-evolving mixing layer in which two adjacent vortices rollup, rotate with each other and finally amalgamate into a single one. Thus, the response of flame to the two adjacent interacting vortices can be isolated. Then the simulation can be conducted in realistic mixing layer flows. The final stage of this study is to incorporate the feedback effects of unsteady heat release on the coherent vortices to study the potential resonant coupling between the unsteady heat release and vortices.

7.2.3. Coupling between the Intrinsic Instabilities of Premixed Flames and Flow Modulations

The above studies can also be extended to incorporate the intrinsic instabilities of flames, which are expected to lead to significantly different flame responses when coupled to the flame oscillations and wrinkling induced by flow modulations. For example, it has been

found that a parametric acoustic instability of planar flames may be produced through the coupling between the acoustic standing waves in tubes and downward propagating flames [8]. The physical mechanism driving this instability is the periodic acceleration of the flame surface separating two regions of different density. For the present study, the flame is oblique and anchored at a fixed point, and hence has some specific characteristics, such as convective wrinkling, in addition to the density jump across the flame. The flame wrinkling is expected to be coupled to the hydrodynamic instability under small frequencies (large wavelength), and to the thermal-diffusive instability under large frequencies (small wavelength). Once the coupling mechanisms between the intrinsic flame instabilities and external flow modulations are understood, they can be utilized to suppress or enhance the intrinsic flame instabilities. For example, it has been found that an acoustic field of moderate intensity can first stabilize the hydrodynamic instability of premixed flames and then, at higher intensity, produce parametric cellular instability with a well-defined threshold and associated with a well-defined critical wavenumber [8].

7.2.4. Thermal-Diffusive Instability of Diffusion Flames in More Realistic Configurations

The studies on the thermal-diffusive instability of diffusion flames in this dissertation were focused on the 1D non-strained planar configuration with a uniform underlying flow field. However, experimentally the unstable phenomena in diffusion flames were mostly observed in configurations with complex underlying flow field, such as jet flames [9] and candle flames [10]. Although thermal-diffusive effects have been identified to play a crucial role, it is not clear to what extent the influence of flow field may have on the development of thermal-diffusive instability. Thus, a comprehensive study of the

thermal-diffusive instability of diffusion flames in more realistic configurations should be conducted. This work should start from the theoretical work of this dissertation with the assumptions that may affect the results relaxed. The final stage of this work is expected to be the numerical simulation of real flames, such as jet flames, using advanced numerical method and detailed chemistry and transport models.

7.2.5. Nonlinear Analysis of Flame Oscillations in Radiative Diffusion Flames

Although we have identified the critical conditions for the onset of flame oscillations near the radiative extinction limit in Chapter 5, the subsequent behavior is still not clear. In particular, persistent flame oscillations (limit-cycle) have only been observed near the radiative limit, and the analysis in Chapter 2 has also shown that limit-cycle near the kinetic limit cannot be realized for parameter values in adiabatic combustion systems. Thus a nonlinear analysis must be carried out for flame oscillations near both extinction limits in radiation-affected diffusion flames. This can be realized using the model derived in Chapter 4 and following the same procedures as those in Chapter 2.

References

1. Cheatham, S. and Matalon, M., *J. Fluid Mech.* **414**: 105-144 (2000).
2. Chao, B. H., Law, C. K., T'ien, J. S., *Proc. Combust. Inst.* **23**: 523–531 (1990).
3. Oh, T. K., Lee, J. S. and Chung, S. H., *Int. J. Heat Mass Transfer* **37**: 2893-2900 (1994).
4. Liu, F., Smallwood, G. J., Gulder, O. L. and Ju, Y., *Combust. Flame* **121**: 275-287 (2000).
5. Sivashinsky, G. I., Law, C. K. and Joulin, G., *Combust. Sci. Technol.* **28**, 155-159 (1982).
6. Law, C. K., *Combustion Physics*, Cambridge University Press, New York (2006).
7. Lieuwen, T., *Proc. Combust. Inst.* **30**: 1725-1732 (2005).
8. Searby, G. and Rochwerger, D., *J. Fluid Mech.* **231**: 529-543 (1991).
9. Furi, M., Papas, P. and Monkewitz, P. A., *Proc. Combust. Inst.* **28**: 831-838 (2000).
10. Ross, H. D., Sotos, R. G. and T'ien, J. S., *Combust. Sci. Technol.* **75**: 155-160 (1991).